

A Particle Finite Element Method for Cutting of Solids

vom Fachbereich Maschinenbau und Verfahrenstechnik
der Technischen Universität Kaiserslautern
zur Verleihung des akademischen Grades
Doktor-Ingenieur (Dr.-Ing.)
genehmigte Dissertation

von
Matthias Sabel, M.Sc.
aus Zell (Mosel)

Hauptreferent: Prof. Dr.-Ing. Ralf Müller
Korreferenten: JP Dr.-Ing. Charlotte Kuhn
Prof. Tarek Zohdi
Vorsitzender: Prof. Dr.-Ing. Jan C. Aurich
Dekan: Prof. Dr.-Ing. Jörg Seewig

Tag der Einreichung: 14.06.2017
Tag der mündlichen Prüfung: 22.09.2017

Kaiserslautern, 2018

D 386

Herausgeber

Lehrstuhl für Technische Mechanik
Technische Universität Kaiserslautern
Gottlieb-Daimler-Straße
Postfach 3049
67653 Kaiserslautern

© Matthias Sabel

Ich danke der „Prof. Dr. Hans Georg und Liselotte Hahn Stiftung“ für die finanzielle Unterstützung bei der Drucklegung.

Druck

Technische Universität Kaiserslautern
Hauptabteilung 5 / Bau-Technik-Energie
Abteilung 5.6 Foto-Repro-Druck

Alle Rechte vorbehalten, auch das des auszugsweisen Nachdrucks, der auszugsweisen oder vollständigen Wiedergabe (Photographie, Mikroskopie), der Speicherung in Datenverarbeitungsanlagen und das der Übersetzung.

ISBN 978-3-942695-16-9

Vorwort

Die vorliegende Arbeit entstand während meiner Tätigkeit als wissenschaftlicher Mitarbeiter am Lehrstuhl für Technische Mechanik der Technischen Universität Kaiserslautern.

An erster Stelle möchte ich mich bei meinem Doktorvater Prof. Dr.-Ing. Ralf Müller für die hervorragende Betreuung und Unterstützung meiner Arbeit bedanken. Außerdem danke ich Prof. Tarek Zohdi und JP Dr.-Ing. Charlotte Kuhn für das Interesse an meiner Arbeit und für die Übernahme der Korreferate sowie Prof. Dr.-Ing. Jan C. Aurich für die Übernahme des Vorsitzes.

Bedanken möchte ich mich auch bei meinen ehemaligen Kollegen für die gemeinsame Zeit am Lehrstuhl, die mir immer in schöner Erinnerung bleiben wird.

Ein besonderer Dank gilt allen, die mir auf dem Weg von der Berufsausbildung zur Promotion immer wieder Mut gemacht haben. Insbesondere Prof. Dr.-Ing. Herbert Baaser, der mich auf einem großen Teil dieses Weges begleitet hat.

Mannheim, August 2018

Matthias Sabel

Kurzfassung

In der spanenden Bearbeitung treten im Werkstück große Deformationen, sowie große Änderungen der Topologie auf. Beispiele dafür sind die Span- und Gratbildung. Besonders die Auftrennung des Materials und die großen Längenskalen stellen etablierte Simulationsmethoden vor große Herausforderungen. Diskrete Simulationsmethoden, wie z.B. die Molekular Dynamik (MD) eignen sich für Simulationen mit stark veränderlicher Topologie. Allerdings weisen diese Methoden schnell sehr hohe Rechenzeiten auf, wenn es darum geht Simulationen auf großen Längenskalen durchzuführen. Die Finite Elemente Methode (FEM) hingegen, basiert auf der Kontinuumsmechanik und ist daher in der Lage auch großskalige Probleme mit einer überschaubaren Anzahl von Freiheitsgraden abzubilden. Andererseits stößt die FEM schnell an ihre Grenzen wenn große Topologieänderungen in Simulationen auftreten. Die Entwicklung der Partikel Finite Elemente Methode ist ein Versuch, die Vorzüge der Finite Elemente Methode mit denen von diskreten Simulationsmethoden zu verbinden. Die Methode wurde zunächst angewandt um schwappende Flüssigkeiten zu simulieren und wurde dann erweitert um die Interaktion von Flüssigkeiten mit Festkörpern zu modellieren. Aber auch die Zahl der Anwendungen in der Mechanik fester Körper wächst stetig. Aufgrund der Fähigkeit komplexes Materialverhalten auf großen Längenskalen zu modellieren und dabei signifikante Topologieänderungen zu berücksichtigen, bildet die PFEM ein geeignetes Werkzeug zur Simulation von Spanprozessen.

Da im Spanprozess große Deformationen auftreten, werden zu Beginn dieser Arbeit die wesentlichen Grundlagen der nichtlinearen Kontinuumsmechanik erläutert. Um Simulationen an verschiedenen Klassen von Materialien durchzuführen, werden zwei konstitutive Gesetze vorgestellt. Ein hyperelastisches Materialmodell kann eingesetzt werden um Spanprozesse an Kunststoffen zu simulieren, während ein elasto-plastisches Materialmodell verwendet wird um das Spanen von Metallen zu modellieren. Auf die Einführung in die Grundgleichungen der Kontinuumsmechanik folgt ein Kapitel zur Formulierung von Finiten Elementen. Die Herleitung der schwachen Form des mechanischen Gleichgewichts wird erläutert sowie deren Diskretisierung mit Dreieckselementen. Da das resultierende Problem nichtlinear von der Verschiebung abhängt, wird das Newton Verfahren vorgestellt, welches zur Lösung des Problems verwendet wird. Die im Newton Verfahren benötigte Linearisierung der schwachen Form wird ebenfalls erläutert.

Ein zentraler Bestandteil der PFEM ist die Detektierung von Randsegmenten einer Partikelwolke. Dazu wird die sogenannte α -shape Methode verwendet, welche ursprünglich im Gebiet der Computergrafik entwickelt wurde. Auf eine kurze Erläuterung der Funktionsweise, folgt eine Parameterstudie um den zentralen Parameter α . Ziel dieser Studie ist es, die Schwierigkeiten der Ermittlung von Randsegmenten und der damit verbundenen Wahl des Parameters aufzuzeigen. Da die Anwendung der α -shape Methode in der PFEM einen Einfluss auf die Materialantwort und die Auftrennung des Materials aufweist, wird in dieser Arbeit eine Interpretation des Parameters im Kontext der Strukturfestigkeit präsentiert. Es wird gezeigt, dass der Parameter α mit einer kritischen Dehnung von Randsegmenten in Verbindung gebracht werden kann, und eine Beziehung zu Eigenvektoren von Verzerrungstensoren wird erläutert. Außerdem wird erklärt, dass α nicht nur die Dehnung von Randsegmenten einschränkt, sondern auch die Orientierung der Segmente limitiert. Dieses Ergebnis wird an PFEM Simulationen von einfachen Deformationszuständen demonstriert. Des Weiteren schaffen Simulationen von Zugversuchen eine Verbindung von α zur Bruchdehnung, wie sie aus der Werkstoffwissenschaft bekannt ist.

In der PFEM folgt auf die Detektion von Randsegmenten die Vernetzung mit Finiten Elementen. Zusammen mit Randbedingungen wird dann ein Finite Elemente Problem formuliert. Zu Beginn der Finite Elemente Simulation muss der Deformationsgradient aus dem vorherigen PFEM-Schritt von den Partikeln auf die Gauß-Punkte übertragen werden. Nach der Lösung des FE Problems wird der aktuelle Deformationsgradient dann zurück auf die Partikel projiziert und dort für den nächsten PFEM-Schritt gespeichert. Bei Simulationen mit elasto-plastischem Material muss zusätzlich zum Deformationsgradienten noch der plastische Deformationsgradient, sowie die Verfestigungsvariable projiziert und auf den Partikeln gespeichert werden. Um den Einfluss der wiederholten Projektion der Variablen auf die Qualität der Ergebnisse zu untersuchen, wird ein Vergleich der PFEM mit der FEM durchgeführt. Verglichen werden Reaktionskräfte aus Simulationen mit hyperelastischem und elasto-plastischem Material an einfachen Geometrien und Deformationszuständen.

In dieser Arbeit werden Spansimulationen mit hyperelastischem und elasto-plastischem Materialverhalten präsentiert. Zu Beginn wird ein vertikales Abtrennen des Werkstücks simuliert, wobei das Werkstück mit Hilfe des hyperelastischen Materials und entsprechenden Parametern als Kunststoff modelliert wird. Die Entwicklung von Schub und Druckspannungen während des Abtrennprozesses wird gezeigt. In diesen Simulationen wird das Werkzeug als Starrkörper betrachtet und Normalkontakt zwischen Werkzeug und Werkstück ist berücksichtigt. Das Werkstück ist in einem gewissen Bereich fixiert, während das Werkzeug mittels einer Verschiebungsrandbedingung in das Werkstück eindringt. Spankräfte können berechnet werden über eine Summation

der Reaktionskräfte an den FE Knoten des Werkzeugs, und in einer Parameterstudie von α werden diese Spankräfte verglichen.

Weitere PFEM Simulationen beschäftigen sich mit dem Extrusionsprozess. Ähnlich zur Simulation des Abtrennprozesses wird hier die Matrize des Extruders als starrer Körper betrachtet und Normalkontakt zwischen Matrize und Werkstück ist berücksichtigt. Das Werkstück wird durch eine Verschiebungsrandbedingung dem Extruder zugeführt, während die Matrize räumlich fixiert ist. Druck- und Zugspannungen, sowie die plastische Deformation des Werkstücks werden betrachtet. Die resultierenden Extrusionskräfte können über eine Summation der Reaktionskräfte am Verschiebungsrand des Werkstücks berechnet werden und ein Vergleich dieser Extrusionskräfte für unterschiedliche Anfangsfließspannungen wird gezeigt.

Ein weiterer Abschnitt dieser Arbeit befasst sich mit der Spansimulation von metallischen Werkstoffen. Dabei wird das elasto-plastische Materialmodell mit entsprechenden Materialparametern für Stähle verwendet. Analog zur Extrusionssimulation, wird in diesen Simulationen das Werkstück mit Hilfe einer Verschiebungsrandbedingung dem Werkzeug zugeführt, während das Werkzeug räumlich fixiert ist. Die Entstehung von Spannungen während des Spanprozesses wird demonstriert und verglichen zu einschlägiger Fachliteratur. Effekte wie die Ausbildung eines Scherbandes im Werkstück, sowie die plastische Deformation im Span und in der Freifläche werden aufgezeigt. Des Weiteren demonstrieren Parameterstudien den Einfluss von wichtigen Prozessparametern auf die Schnittkräfte, die Spannungen und die plastische Deformation. Eine Parameterstudie von α zeigt auf, dass mit der Wahl von α das Spannen von spröden oder zähen Werkstoffen realisiert werden kann. Abschließend wird ein Vergleich von Spankräften aus PFEM Simulationen zu einer empirischen Methode durchgeführt.

Abstract

In cutting processes the material experiences large deformations and large configurational changes. This challenges established modelling techniques such as the finite element method (FEM) or molecular dynamics (MD). Discrete methods are well suited to model large configurational changes, yet are computationally expensive for large length and time scales. Continuum based methods on the other hand, are well fit to model problems on the length scale of engineering components as well as intricate geometries. Another benefit of the FEM is the ability to model complex material behaviour. However, large topological changes push the method to its limits. The particle finite element method (PFEM) represents a combination of the benefits of discrete modelling techniques and continuum based methods. First applied to problems with sloshing liquids, the range of applications has widened to solid mechanics and simulations with fluid-solid interaction.

Since large deformations occur in cutting simulations, some relations of nonlinear continuum mechanics are provided in the beginning of this work. In order to model the cutting of metals and plastics, an elasto-plastic material model is introduced as well as the concept of hyperelasticity. The following chapter is concerned with the finite element formulation. The derivation of the weak form is elaborated as well as the spatial discretisation. Since the weak form is nonlinear in the displacements, a Newton scheme is employed and the linearisation of the weak form is demonstrated in this work. Moreover the integration of the inelastic constitutive equations is explained.

A central operation within the PFEM is the detection of the boundary of a set of particles. This is accomplished with the so called α -shape method which was developed in the field of computer graphics. After a brief description of the working principle, a parameter study is conducted on the method's central parameter α in order to demonstrate the difficulties in the detection of boundary segments. Furthermore, a physical interpretation of the α -shape method in the context of strength of materials is provided. It is shown that the parameter α can be associated to a critical stretch of boundary segments and a relation to eigenvalues of strain tensors is presented. In addition it is elaborated that α not only limits the stretch of boundary segments but

also the orientation. PFEM simulations of circular discs under basic deformations - such as uniaxial stretch, biaxial stretch, and simple shear - are studied to demonstrate these effects. Tensile tests on specimens with geometries similar to experiments in material science are presented and a relation of α to the fracture strain is elaborated. Further simulations demonstrate that by varying α the separation of material can be triggered, which enables the modelling of brittle or ductile material.

In a PFEM simulation the boundary detection is followed by a meshing algorithm and in combination with boundary conditions, a finite element problem is formulated. In the beginning of the finite element simulation the deformation gradient of the previous PFEM step is transferred from the particles to the Gauß points. After solving the FEM problem, the actual deformation gradient is projected to the particles and stored for the next step. For simulations with elasto-plastic material, the plastic deformation gradient and the hardening variable are projected and stored on the particles as well. In order to investigate the influence of the frequent projection on the quality of the results, a comparison of PFEM to FEM simulations is studied. The benchmarks include problems with uniform deformations as well as non-uniform deformations. These simulations are executed with hyperelastic and elasto-plastic material.

In this work cutting simulations of hyperelastic and elasto-plastic are presented. In combination with suitable material parameters, the material models enable a cutting of plastics and metals. The first cutting simulation in this work focuses on vertical cutting of a workpiece with hyperelastic material. The evolution of shear and compressive stresses during the cutting process is demonstrated. In the simulations the cutting tool is considered as rigid body and normal contact is considered between tool and workpiece. The workpiece is partially fixed, whereas a displacement boundary condition is applied to the tool. Cutting forces are computed by a summation of reaction forces at the finite element nodes of the tool. For the vertical cutting simulations of hyperelastic material, the cutting forces are compared for a variation of α . Furthermore, an extrusion process is studied using an elasto-plastic material. Analog to the cutting simulations, the die of the extruder is considered as a rigid body and normal contact to the workpiece is considered. The workpiece is fed to the die by a displacement boundary condition and the die is fixed in space. The compressive stresses in the workpiece during the extrusion process are studied as well as the plastic deformation.

Extrusion forces are computed analog to the cutting simulations and a parameter study on the initial yield stress is presented.

For the cutting of metals, the elasto-plastic material model is considered for the workpiece. Similar to the extrusion simulations, the workpiece is fed to the cutting tool by applying a displacement boundary condition at the base of the workpiece and the tool is fixed in space. The evolution of stresses in the workpiece is studied throughout the cutting process and compared to literature. Effects such as the development of shear bands are observed and the plastic deformation in the workpiece is demonstrated. Parameter studies are conducted in order to show the influence of certain process parameters on the cutting force, the stresses, and the plastic deformation. A parameter study on α demonstrates that cutting of brittle or ductile material can be realised by choosing an appropriate value for α . Furthermore, a comparison of the cutting forces to an empirical model is considered. In a first approach the cutting force from a PFEM simulation is compared to the empirical method for one specific cutting depth. In order to do so, a certain segment of the PFEM result is selected, in which the cutting force is relatively constant. In a second step the PFEM cutting forces are compared to the empirical method for several cutting depths. In this example the material parameters for the PFEM simulation are fixed and only the cutting depth is varied.

Contents

1	Introduction	1
1.1	Motivation and State of the Art	1
1.2	Objectives and Overview	4
2	Continuum Mechanics	7
2.1	Kinematics	7
2.1.1	Deformation Gradient	7
2.1.2	Decomposition of the Deformation Gradient	10
2.1.3	Polar Decomposition	12
2.1.4	Strain Tensors	12
2.1.5	Spectral Decomposition of Strain Tensors	13
2.1.6	Small Strains	14
2.1.7	The Hencky Strain	15
2.2	Stress Tensors	15
2.3	Equilibrium Equation	17
2.4	Constitutive Laws	19
2.4.1	Linear Elasticity	19
2.4.2	Hyperelasticity	20
2.4.3	Von Mises Plasticity	21
3	Numerical Implementation	25
3.1	Weak Form of Equilibrium Equation	25
3.2	Linearisation of the Weak Form	26
3.3	Spatial Discretisation	28
3.4	Numerical Integration	32
3.5	Local Integration of Inelastic Constitutive Relations	33
3.5.1	Return Mapping Algorithm for Small Strain Plasticity	33
3.5.2	Extension to Finite Strains	35
3.6	Solution of Nonlinear Problems	37

4	The Particle Finite Element Method	39
4.1	Structure of the PFEM Algorithm	39
4.1.1	Detecting the Shape of a Particle Set	41
4.1.2	Processing of History Variables	45
4.2	Validation of the PFEM on Benchmarks	46
4.2.1	Examples with Uniform Deformations	46
4.2.2	Examples with Non-Uniform Deformations	49
4.3	Physical Interpretation of α	51
4.3.1	The Role of α in Tensile Tests	65
4.3.2	Modelling of Material Separation	68
5	Cutting Simulations	71
5.1	Vertical Cutting of Hyperelastic Material	71
5.2	Extrusion of Elasto-Plastic Material	74
5.3	Cutting Simulations for Elasto-Plastic Material	77
5.4	Study of Important Process Parameters	79
5.4.1	Variation of the Hardening Modulus	79
5.4.2	Variation of the Rake Angle	80
5.4.3	Variation of α	81
5.5	Comparison to Empirical Results	84
6	Conclusion and Outlook	87

Chapter 1

Introduction

1.1 Motivation and State of the Art

In manufacturing the processed material is often referred to as workpiece and experiences large deformations in many operations, such as forging, deep drawing or turning. Especially cutting processes e.g. turning, milling, and drilling are characterised by large deformations and large changes in the topology. In these procedures the cutting edge of a tool penetrates the workpiece and produces chips and burrs. Figure 1.1 sketches the cutting process.

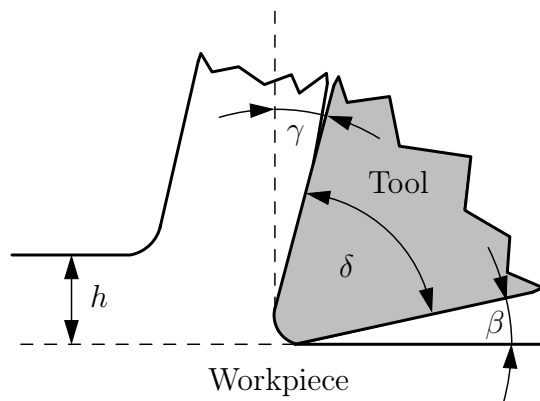


Fig. 1.1: Tool and workpiece in cutting process

In manufacturing technology a certain terminology are used to specify cutting processes. One of which distinguishes the angles of the cutting edge as demonstrated in Fig. 1.1. The rake angle γ is defined as the angle between the rake face and the vertical, whereas the clearance angle β is defined as the angle between flank face and the horizontal. Together with the wedge angle δ , the relation $\beta + \delta + \gamma = 90^\circ$ is prescribed. The cutting depth is depicted by h in Fig. 1.1.

The physical modelling of cutting processes is challenging due to several reasons. For one, the material undergoes large deformations and large configurational changes. Especially the formation of chips and burrs pushes established modelling techniques to their limits. Due to the large deformations, elaborate material models are required for certain groups of materials. For instance, plastic deformations in the workpiece have to be considered in cutting simulations of metals. In cutting simulations of plastics a different class of material models is used, which are referred to as hyperelastic (Holzapfel, 2000; Bonet and Wood, 2008). Further obstacles in the simulation of cutting processes are the length and time scale of the problem. Simulations on the scale of engineering components generate unreasonably high computational effort for some modelling techniques and only short simulation times can be considered. For this reason, methods based on continuum mechanics, such as the finite element method (FEM), are well suited. Large length and time scales can be covered, while the number of unknowns remains moderate. Another benefit of the FEM is the ability to cope with intricate geometries and complex material behaviour such as plasticity at finite strains, which is important for simulations of metal cutting. Nonetheless, large changes in the topology push the FEM to its limits and numerous work has been done to expand the FEM in order to cope with material separations. Approaches to separate the mesh can be found in Komvopoulos and Erpenbeck (1991); Shet and Deng (2000); Li et al. (2002); Mamalis et al. (2001), where the nodes are separated depending on various criteria. Another technique is the use of link elements, which are placed in the path of the cutting tool and fail once the tool is in contact (Zhang and Bagchi, 1994). In some cases however, the decision process whether the nodes are separated or the link elements are removed, may be considered as rather unphysical. An empirical method to predict cutting forces can be found in Kienzle (1952), which is used as a benchmark in this work.

Discrete modelling techniques such as molecular dynamics (MD) are well suited to model topological changes and cutting simulations on atomistic scales can be found in Gao and Urbassek (2014); Alhafez et al. (2017). However, increasing length and time scales lead to an unreasonable increase in computation time. Aside from MD, the cutting process has been modelled with other mesh less methods such as smooth particles hydrodynamics (SPH) Heinstein and Segalman (1997); Limido et al. (2007). Cutting simulations using the finite pointset method (FPM) can be found in Uhlmann et al. (2013, 2011) and in Eberhard and Gaugele (2013); Fleissner et al. (2007) the discrete element method (DEM) is applied to model cutting processes.

The development of the particle finite element method (PFEM) is an attempt to combine the benefits of discrete methods and modelling techniques based on continuum mechanics. The first applications of the PFEM were concerned with sloshing liquids (Oñate et al., 2004; Idelsohn et al., 2006, 2004; Aubry et al., 2005, 2006), where collapsing water columns and free surface waves are simulated. Recent work in this field can be found in Zhu and Scott (2014, 2017). Applications to problems with fluid-solid interaction can be found in Oñate et al. (2006, 2011); Oñate et al. (2008). Since sloshing liquids represent large topological changes, the finite element nodes are treated as a set of particles and a so called α -shape algorithm is employed to detect the shape of the set throughout the simulation. The α -shape method was developed in the field of computer graphics (Edelsbrunner and Mücke (1994); Fischer (2000) and literature cited in there) and provides a list of boundary segments, which is required for the subsequent meshing procedure. After the mesh generation, a finite element problem is solved and the particle coordinates are updated. In this way, changes in the topology can be encountered, while simulations on large length and time scales can be considered. An outline of the PFEM algorithm is illustrated in Fig. 1.2 and a detailed explanation is provided in chapter 4.

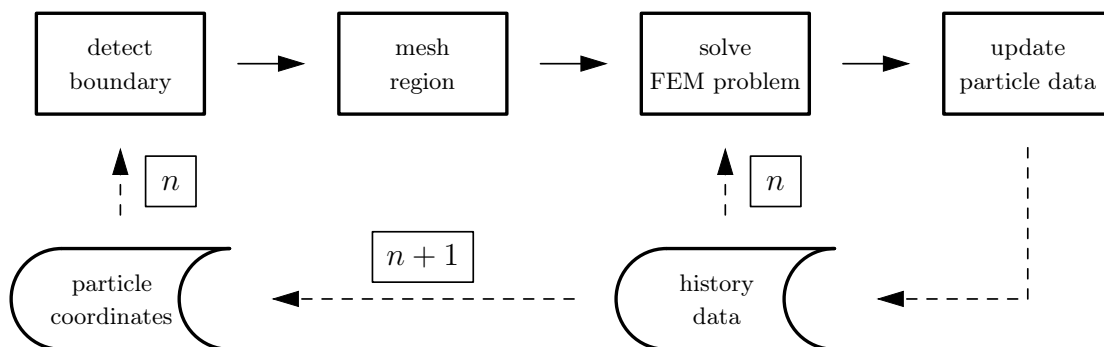


Fig. 1.2: Outline of the PFEM algorithm

In the α -shape method circles for every pair of particles in the set are defined, where the radius of the circles is scaled by a parameter α , hence the name α -shape method. As demonstrated in Edelsbrunner and Mücke (1994); Fischer (2000), the parameter α controls the level of detail of the detected shape and in Oñate et al. (2004) experience based recommendations are provided for the choice of α . As the number of PFEM applications in solid mechanics increased (Oliver et al., 2007; Carbonell et al., 2013, 2010) it was observed in Sabel et al. (2014) that the parameter α affects the material response. In Sabel et al. (2016b) a first attempt was made to find a physical interpretation for α . Applications in the modelling of cutting processes can be found in Sabel et al. (2016a); Rodríguez et al. (2017a,b); Oñate et al. (2014).

1.2 Objectives and Overview

The basic relations of continuum mechanics necessary for the implementation of the PFEM are introduced in chapter 2. The chapter starts with the definition of the deformation gradient and a multiplicative decomposition which is followed by the derivation of strain tensors. The Hencky strain is introduced, which is crucial for the plasticity model used in this work. After the definition of strain tensors, the concept of stress is introduced. The chapter closes with constitutive laws such as hyperelasticity, and von Mises plasticity.

Chapter 3 begins with the derivation of the weak form of the equilibrium equation, which is followed by the linearisation of the weak form. The spatial discretisation is elaborated, as well as the numerical integration. The time integration of inelastic constitutive relations on the element level is explained and the extension from small strain plasticity to finite strains is introduced. The chapter closes with comments on the Newton scheme, which is used to solve nonlinear systems of equations.

The implementation of the particle finite element method (PFEM) is elaborated in chapter 4. At first, the structure of the PFEM algorithm is explained followed by a description of the detection of boundary segments. The boundary is detected with the α -shape method, which is studied in a benchmark with intricate topology. For the PFEM implementation it is crucial to store deformation data on particles and therefore it is necessary to transfer the data from the element level to the particles and vice versa. This procedure is also explained in chapter 4. The PFEM is then validated by a comparison to the finite element method (FEM) on several benchmarks, which include problems with uniform deformations such as uniaxial stretch and simple shear as well as non-uniform deformations. Two constitutive laws are considered and the validation is accomplished by a comparison of reaction forces of FEM and PFEM. Furthermore, the influence of the discretisation and the number of projections is investigated.

Section 4.3 is concerned with a physical interpretation of the α -shape method. A relation of the parameter α to the stretch ratio is presented as well as a connection to eigenvalues of a strain tensor and the respective eigenvectors. The outcome of this interpretation is demonstrated on PFEM simulations of basic deformations such as uniaxial tension, simple shear, and biaxial shear. Furthermore, a graphical explanation the interpretation is provided. Finally, the role of α in material science is discussed on tensile tests and simulations with separating material are shown.

In chapter 5 cutting simulations with hyperelastic and elasto-plastic material are presented. The chapter begins with simulations of a vertical cutting process with hyperelastic material, where a parameter study demonstrates the influence of the parameter α on the cutting force. Contour plots of simulations with varying α illustrate the influence on material separation. A further example is the extrusion of elasto-plastic material through a die. In these simulations the stresses are studied as well as the plastic deformation as they occur during the extrusion process. A parameter study on the initial yield stress is conducted and the extrusion forces are compared. In the following section typical effects known from manufacturing technology are studied. The chip formation in cutting of elasto-plastic material is investigated and stresses, as well as the plastic deformation in the workpiece are observed. Parameter studies are conducted in order to investigate the influence of parameters such as the hardening modulus, the rake angle, as well as α on the cutting force. Given the physical interpretation, especially the parameter study on α is of interest. Therefore, the norm of the plastic deformation gradient is demonstrated in contour plots for a varying α . At the end of the chapter empirical results are compared to cutting forces calculated by the PFEM. The cutting forces are first compared for a fixed set of parameters and one decisive cutting depth h . In a follow up study an attempt is made to reproduce the empirical results for various cutting depths h .

Chapter 6 provides some conclusions and a brief outlook on further research.

Chapter 2

Continuum Mechanics

The particle finite element implementation developed in this work, is based on nonlinear continuum mechanics. Some core concepts of continuum mechanics are introduced in this chapter, such as kinematics, stress measures, the mechanical equilibrium, and some constitutive laws. For more details on continuum mechanics, the reader is referred to classical textbooks such as Holzapfel (2000); Spencer (2004); Greve (2003); Bonet and Wood (2008); Becker and Gross (2002); Sadd (2014); Simo and Hughes (2000); de Souza Neto et al. (2011).

2.1 Kinematics

2.1.1 Deformation Gradient

The deformation φ of a continuous body \mathcal{B} in space can be considered as a sequence of configurations, where the term *configuration* refers to a region Ω_t which is occupied by the body at time t . In the following, Ω_t is called actual or current configuration since it is associated to the current time t . The material points of the body in the current configuration are described using spatial (Eulerian) coordinates \boldsymbol{x} . For convenience, an initial configuration Ω_0 can be introduced to provide a reference at time $t = 0$. Hence, this configuration is called reference configuration and the position of the material points is described by the reference (Lagrangian) coordinates \boldsymbol{X} . Figure 2.1 illustrates the body \mathcal{B} in the reference and current configuration.

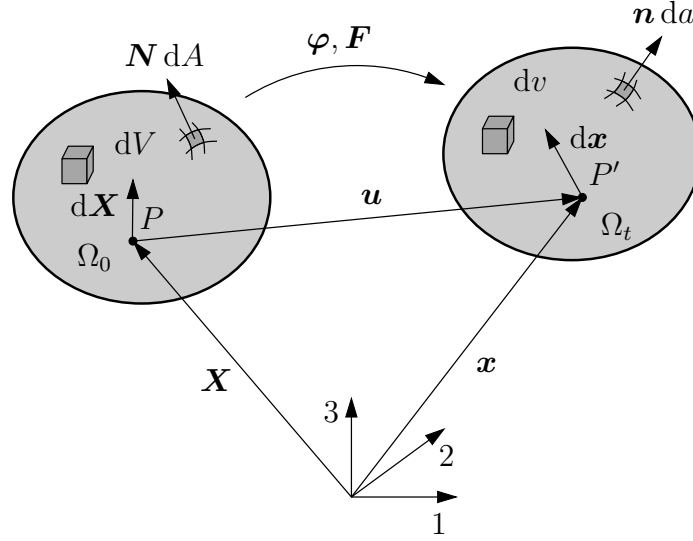


Fig. 2.1: Body in reference- and current configuration

Since the current position of a material point at time t depends on the deformation φ and the reference coordinates \mathbf{X} , the spatial coordinates can also be expressed as

$$\mathbf{x} = \mathbf{x}(\mathbf{X}) = \varphi(\mathbf{X}) . \quad (2.1)$$

The derivative of the deformation with respect to the Lagrangian coordinates is called deformation gradient

$$\mathbf{F} = \frac{\partial \mathbf{x}}{\partial \mathbf{X}} = \frac{\partial \varphi(\mathbf{X})}{\partial \mathbf{X}} , \quad (2.2)$$

which is a commonly used measure in the finite deformation theory and for the definition of strain tensors. Since the current position of a material point can also be defined by the reference coordinates and the displacement vector \mathbf{u}

$$\mathbf{x} = \mathbf{X} + \mathbf{u} , \quad (2.3)$$

the deformation gradient in Eq. (2.2) may be expressed alternatively in terms of displacements \mathbf{u} . Combining Eq. (2.2) and Eq. (2.3) leads to the definition of the displacement gradient

$$\mathbf{H} = \frac{\partial \mathbf{u}}{\partial \mathbf{X}} = \frac{\partial (\mathbf{x} - \mathbf{X})}{\partial \mathbf{X}} = \mathbf{F} - \mathbf{1} , \quad (2.4)$$

where $\mathbf{1}$ is the second order identity tensor. By employing the deformation gradient, the deformation of infinitesimal line segments, surface elements, and volume elements can be described, which is crucial to define balance laws and stress measures for the reference and spatial configurations.

For neighbouring points that define a line segment of infinitesimal length, the map

$$d\mathbf{x} = \mathbf{F} d\mathbf{X} \quad (2.5)$$

can be defined to describe the deformation of that line segment. For volume elements $dV = dX_1 dX_2 dX_3$ and $dv = dx_1 dx_2 dx_3$ the relation

$$dv = J dV \quad (2.6)$$

holds, where $J = \det \mathbf{F}$. The deformation gradient \mathbf{F} is invertible and therefore $J \neq 0$, and since a volume must not be negative $J > 0$ follows. In the case that the body is not subjected to a deformation i.e. $\mathbf{x} = \mathbf{X}$ and therefore $\mathbf{F} = \mathbf{1}$ respectively, we obtain $J = 1$.

The deformation of small surface elements is crucial for the transformation of stress tensors. To obtain a relation between the surface elements

$$d\mathbf{a} = \mathbf{n} da \quad \text{and} \quad d\mathbf{A} = \mathbf{N} dA \quad (2.7)$$

from Fig. 2.1 we express the deformation of volume elements in Eq. (2.6) as

$$dv = d\mathbf{a} \cdot d\mathbf{x} = J d\mathbf{A} \cdot d\mathbf{X}. \quad (2.8)$$

The surface elements in Eq. (2.7) are defined using normal vectors \mathbf{N} and \mathbf{n} as well as infinitesimal surface areas dA and da . Employing Eq. (2.5), the deformed line segment in Eq. (2.8) can be replaced, which yields

$$d\mathbf{a} \cdot \mathbf{F} d\mathbf{X} = J d\mathbf{A} \cdot d\mathbf{X}. \quad (2.9)$$

Rearranging Eq. (2.9) leads to

$$(\mathbf{F}^T d\mathbf{a} - J d\mathbf{A}) \cdot d\mathbf{X} = 0, \quad (2.10)$$

and for arbitrary line segments $d\mathbf{X}$ we finally obtain

$$d\mathbf{a} = J \mathbf{F}^{-T} d\mathbf{A} \quad \text{or} \quad da \mathbf{n} = J \mathbf{F}^{-T} dA \mathbf{N}. \quad (2.11)$$

The relation between deformed- and undeformed surface elements in Eq. (2.11) is known in literature as Nanson's formula.

2.1.2 Decomposition of the Deformation Gradient

As mentioned in the introduction of the deformation gradient, the deformation can be considered as a sequence of configurations. Nonetheless, we fixated on just distinguishing between two, the reference- and the actual configuration. In the following, we consider a sequence of configurations in order to define a multiplicative decomposition of the deformation gradient, which e.g. is important for the modelling of elasto-plastic material at finite strains. In this case the deformation gradient is split in an elastic part \mathbf{F}^e and a plastic part \mathbf{F}^p , which was first applied in Lee (1969). In the context of the particle finite element method, the decomposition is also needed, which is explained in more detail in Sec. 4. In order to elaborate the multiplicative decomposition of the deformation gradient, we will first study the body \mathcal{B} in Fig. 2.2, which is subjected to the deformation φ_1 .

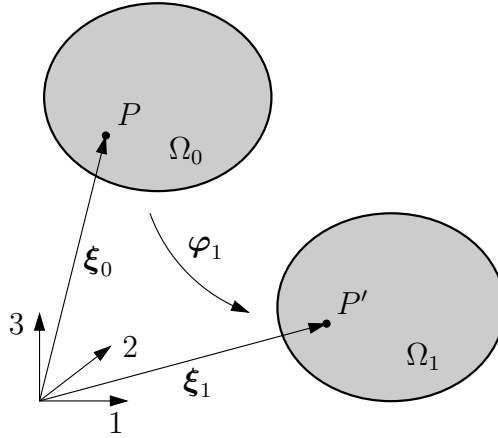
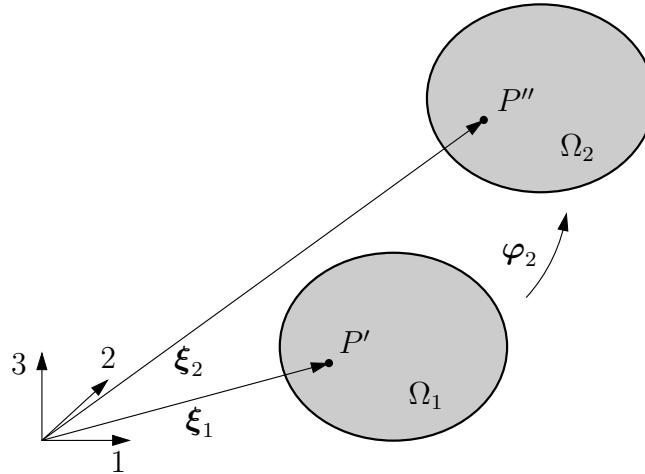


Fig. 2.2: Two configurations of body \mathcal{B}

The coordinates ξ_1 in configuration Ω_1 can also be expressed as function of the coordinates of configuration Ω_0 i.e. $\xi_1 = \varphi_1(\xi_0)$. Then, the deformation gradient yields

$$\mathbf{F}_1 = \frac{\partial \xi_1}{\partial \xi_0} = \frac{\partial \varphi_1(\xi_0)}{\partial \xi_0}. \quad (2.12)$$

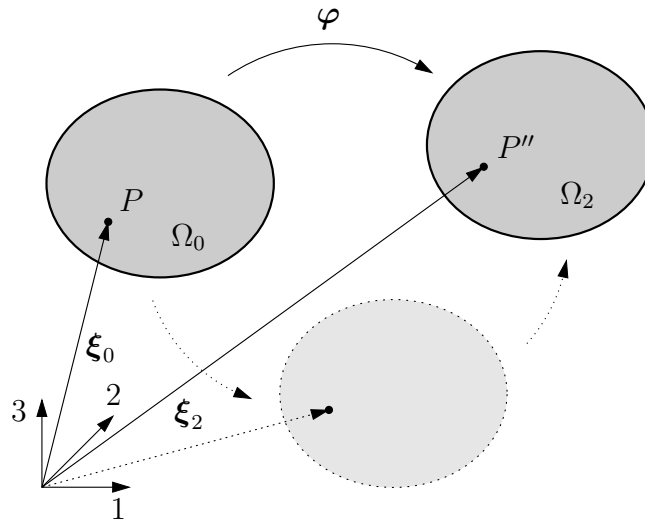
Next, we consider the body \mathcal{B} subjected to a second deformation φ_2 , which evokes a new configuration Ω_2 as shown in Fig. 2.3.


 Fig. 2.3: Body \mathcal{B} in configuration Ω_1 and Ω_2

The coordinates in this configuration are labeled $\xi_2 = \varphi_2(\xi_1)$ and the deformation gradient is defined as

$$\mathbf{F}_2 = \frac{\partial \xi_2}{\partial \xi_1} = \frac{\partial \varphi_2(\xi_1)}{\partial \xi_1}. \quad (2.13)$$

Alternatively, we consider a deformation φ that maps the coordinates ξ_0 of configuration Ω_0 to the coordinates ξ_2 of configuration Ω_2 as illustrated in Fig. 2.4.


 Fig. 2.4: Body \mathcal{B} subjected to deformation φ

The deformation φ can be alternatively expressed as $\varphi = \varphi_2(\varphi_1(\xi_0))$. The deformation gradient then follows as

$$\mathbf{F} = \frac{\partial \varphi_2(\varphi_1(\xi_0))}{\partial \xi_0} = \frac{\partial \varphi_2(\varphi_1(\xi_0))}{\partial \varphi_1} \frac{\partial \varphi_1(\xi_0)}{\partial \xi_0} = \frac{\partial \xi_2}{\partial \xi_1} \frac{\partial \xi_1}{\partial \xi_0} = \mathbf{F}_2 \mathbf{F}_1. \quad (2.14)$$

The deformation gradient for a respective sequence of $n + 1$ configurations can then be expressed as a product of n deformation gradients

$$\mathbf{F} = \prod_{i=1}^n \frac{\partial \boldsymbol{\xi}_{n+1-i}}{\partial \boldsymbol{\xi}_{n-i}} = \prod_{i=1}^n \mathbf{F}_{n+1-i}. \quad (2.15)$$

2.1.3 Polar Decomposition

In Eq. (2.15) a multiplicative decomposition of the deformation gradient is presented. As mentioned, the multiplicative split can be applied for several purposes. An important application is the unique decomposition in a rotation part \mathbf{R} and a stretch part \mathbf{U} or \mathbf{V} , which is useful for the definition of strain tensors. The split of the deformation gradient can then be defined as

$$\mathbf{F} = \mathbf{R}\mathbf{U} = \mathbf{V}\mathbf{R}, \quad (2.16)$$

where \mathbf{U} is called the right stretch tensor and \mathbf{V} represents the left stretch tensor. The rotation tensor \mathbf{R} is a proper orthogonal tensor and therefore $\mathbf{R}^T \mathbf{R} = \mathbf{1}$, where the stretch tensors are symmetric thus, $\mathbf{U} = \mathbf{U}^T$ and $\mathbf{V} = \mathbf{V}^T$.

2.1.4 Strain Tensors

Strain tensors are defined with respect to the reference configuration or the spatial configuration. The right Cauchy-Green tensor yields

$$\mathbf{C} = \mathbf{F}^T \mathbf{F} \quad \text{or} \quad C_{IJ} = F_{kI} F_{kJ}. \quad (2.17)$$

In the following, we assign capital indices to the reference configuration and lower case indices to the current configuration. The summation convention is adopted, which implies a summation over an index from one to three if that index appears twice in the same term. In Eq. (2.17) it can be observed that both indices of the right Cauchy-Green tensor refer to the reference configuration. By expressing the deformation gradient in Eq. (2.16) with the right stretch tensor and the rotation tensor from Eq. (2.16), the right Cauchy-Green tensor can be expressed as

$$\mathbf{C} = \mathbf{F}^T \mathbf{F} = (\mathbf{R}\mathbf{U})^T \mathbf{R}\mathbf{U} = \mathbf{U}^T \mathbf{R}^T \mathbf{R}\mathbf{U} = \mathbf{U}^T \mathbf{U} = \mathbf{U}^2. \quad (2.18)$$

In analogy, the left Cauchy-Green tensor is defined as

$$\mathbf{b} = \mathbf{F}\mathbf{F}^T = \quad \text{or} \quad b_{ij} = F_{iK} F_{jK}, \quad (2.19)$$

and it can be observed that both indices of the left Cauchy-Green tensor refer to the spatial configuration. By replacing the deformation gradient in Eq. (2.19) with the

left stretch tensor \mathbf{V} and the rotation tensor \mathbf{R} , the left Cauchy-Green tensor can be rearranged to

$$\mathbf{b} = \mathbf{F} \mathbf{F}^T = \mathbf{V} \mathbf{R} (\mathbf{V} \mathbf{R})^T = \mathbf{V} \mathbf{R} \mathbf{R}^T \mathbf{V}^T = \mathbf{V}^T \mathbf{V} = \mathbf{V}^2. \quad (2.20)$$

In Eq. (2.18) and (2.20) the rigid body rotations of the deformation gradient cancel out due to the properties of the orthogonal tensor $\mathbf{R}^T \mathbf{R} = \mathbf{1}$. Therefore, the tensors \mathbf{C} and \mathbf{b} represent a pure straining and - in contrast to the tensors \mathbf{U} and \mathbf{V} - are positive definite. A further strain measure is the Green-Lagrange strain tensor, which is defined as

$$\mathbf{E} = \frac{1}{2} (\text{Grad}^T \mathbf{u} + \text{Grad} \mathbf{u}) + \frac{1}{2} \text{Grad}^T \mathbf{u} \text{Grad} \mathbf{u}, \quad (2.21)$$

with the displacement gradient

$$\text{Grad} \mathbf{u} = \frac{\partial \mathbf{u}}{\partial \mathbf{X}} = \mathbf{H}. \quad (2.22)$$

The Green-Lagrange strain tensor is defined with respect to the reference configuration. With the right Cauchy-Green tensor from Eq. (2.17) and the definition of the displacement gradient from Eq. (2.4), the Green-Lagrange strain tensor can also be expressed as

$$\mathbf{E} = \frac{1}{2} (\mathbf{C} - \mathbf{1}). \quad (2.23)$$

The equivalent of the Green-Lagrange tensor in the spatial configuration is the Euler-Almansi tensor

$$\boldsymbol{\epsilon} = \frac{1}{2} (\text{grad}^T \mathbf{u} + \text{grad} \mathbf{u}) + \frac{1}{2} \text{grad}^T \mathbf{u} \text{grad} \mathbf{u}, \quad (2.24)$$

where the displacement gradient in Eq. (2.24) is defined with respect to the spatial configuration

$$\text{grad} \mathbf{u} = \frac{\partial \mathbf{u}}{\partial \mathbf{x}}. \quad (2.25)$$

In analogy to the Green-Lagrange tensor, the Euler-Almansi tensor can be expressed using the left Cauchy-Green tensor from Eq. (2.19)

$$\boldsymbol{\epsilon} = \frac{1}{2} (\mathbf{1} - \mathbf{b}^{-1}). \quad (2.26)$$

2.1.5 Spectral Decomposition of Strain Tensors

Since strain tensors are symmetric, a representation in terms of the eigenvalues of these tensors can be introduced. The spectral decomposition is useful in some applications, one of which is shown in Sec. 2.1.7 within the definition of the Hencky strain. The right

and left Cauchy-Green tensors from Eq. (2.17) and Eq. (2.19) can then be expressed as

$$\mathbf{C} = \mathbf{U}^2 = \sum_{i=1}^3 \lambda_i^2 \mathbf{N}_i \otimes \mathbf{N}_i \quad \text{and} \quad \mathbf{b} = \mathbf{V}^2 = \sum_{i=1}^3 \lambda_i^2 \mathbf{n}_i \otimes \mathbf{n}_i, \quad (2.27)$$

where λ_i^2 are the eigenvalues of the right and left Cauchy-Green tensors. In Eq. (2.27) can also be observed that the eigenvalues of both tensors are identical. However, the eigenvectors \mathbf{N}_i and \mathbf{n}_i refer to different configurations.

2.1.6 Small Strains

In many applications small strains are sufficient to describe the deformation of a material. In these cases the displacement \mathbf{u} is assumed to be small and the spatial coordinates approximate the reference coordinates $\mathbf{x} \approx \mathbf{X}$. Then, the displacement gradient from Eq. (2.4) yields

$$|H_{ij}| \ll 1. \quad (2.28)$$

Considering the definition of the Green-Lagrange tensor and the Euler-Almansi tensor in Eq. (2.21) and (2.24), one can observe with Eq. (2.28) that the nonlinear terms are small of higher order and can be neglected. With these assumption, we can define the linearised strain tensor

$$\boldsymbol{\varepsilon} = \frac{1}{2} (\text{grad}^T \mathbf{u} + \text{grad} \mathbf{u}) . \quad (2.29)$$

Split in Spherical and Deviatoric Part

For elasto-plastic material models, a decomposition of the linearised strain tensor into a spherical and deviatoric part is practical, since plastic deformations are considered to be incompressible. With the definition of a spherical strain

$$\varepsilon_s = \frac{1}{3} \text{tr} \boldsymbol{\varepsilon}, \quad (2.30)$$

and the deviatoric strain \mathbf{e} , the linearised strain tensor can be decomposed as

$$\boldsymbol{\varepsilon} = \varepsilon_s \mathbf{1} + \mathbf{e}. \quad (2.31)$$

In Eq. (2.30) the spherical strain is introduced using the trace operator tr , which is defined as $\text{tr} \boldsymbol{\varepsilon} = \varepsilon_{ii} = \varepsilon_{11} + \varepsilon_{22} + \varepsilon_{33}$.

2.1.7 The Hencky Strain

In Eq. (2.31) an additive decomposition of the linearised strain tensor is presented. The additive decomposition can only be realised due to the assumptions made in linear theory, namely $|H_{ij}| \ll 1$. In the finite deformation regime, only multiplicative decompositions can be realised as in Eq. (2.15). In order to provide an additive decomposition of nonlinear strain tensors, the logarithmic strain (or Hencky strain) can be used. The Hencky strain is defined as

$$\boldsymbol{\varepsilon} = \frac{1}{2} \ln \mathbf{C} = \ln \mathbf{U}. \quad (2.32)$$

The properties of the Hencky strain can be easily shown by using the relations in Eq. (2.18). In conjunction with $\mathbf{U} = \mathbf{U}^T$, Eq. (2.32) can be expressed as

$$\boldsymbol{\varepsilon} = \frac{1}{2} \ln \mathbf{C} = \frac{1}{2} \ln \mathbf{U}^2 = \frac{1}{2} (\ln \mathbf{U} + \ln \mathbf{U}) = \ln \mathbf{U}. \quad (2.33)$$

As shown in Eq. (2.33), the properties of the logarithm enable an additive decomposition of nonlinear strain tensors. This feature is used in this work to model elasto-plastic material, which is described in more detail in Sec. 3.5.2. For the actual computation of the Hencky strain, the spectral decomposition from Eq. (2.27) is required. Then the Hencky strain can be expressed as

$$\boldsymbol{\varepsilon} = \frac{1}{2} \sum_{i=1}^3 \ln (\lambda_i^2) \mathbf{N}_i \otimes \mathbf{N}_i, \quad (2.34)$$

where λ_i^2 are the eigenvalues and \mathbf{N}_i the eigenvectors of the right Cauchy-Green tensor \mathbf{C} .

2.2 Stress Tensors

To elaborate the concept of stress, we consider a control volume Ω_t in the current configuration as in Fig. 2.5 which is exposed to traction loads \mathbf{t} and volume loads \mathbf{b} . These loads induce inner forces $\Delta \mathbf{F}$ which are assumed to act on small surface elements Δa , as demonstrated in Fig. 2.6.

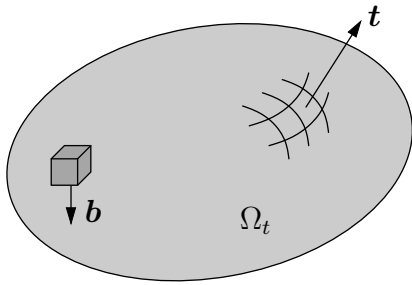


Fig. 2.5: Arbitrary control volume

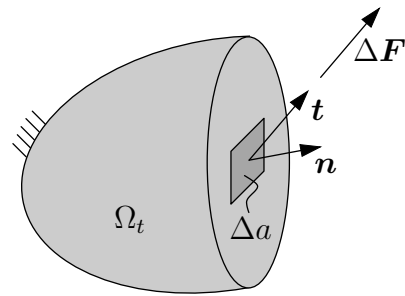


Fig. 2.6: Traction vector

The orientation of the cut, and therefore the surface element is characterised by the unit normal vector \mathbf{n} and the so called traction vector can then be defined as

$$\mathbf{t} = \lim_{\Delta a \rightarrow 0} \frac{\Delta \mathbf{F}}{\Delta a}. \quad (2.35)$$

The traction vector can also be described by a component collinear to the surface normal, which is called normal stress σ , and an orthogonal component called shear stress τ . In order to fully describe the state of stress in the body, three orthogonal cuts are processed. The resulting traction vectors and stresses are shown in Fig. 2.7.

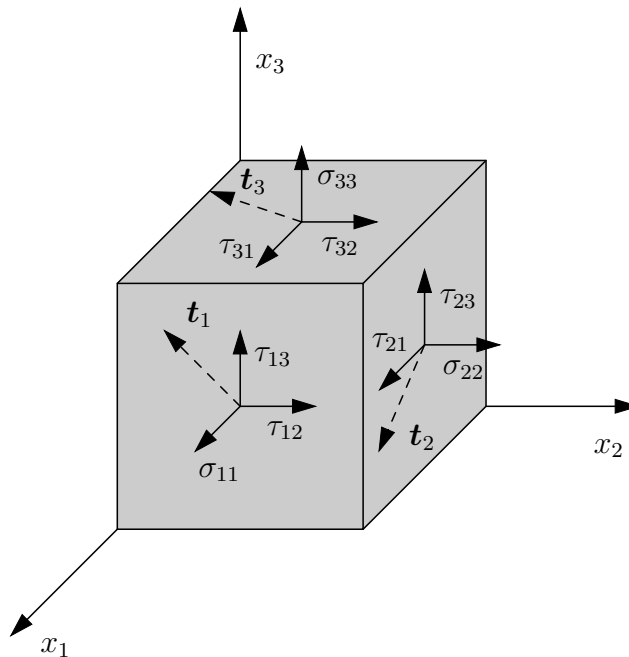


Fig. 2.7: Cube displaying components of stress

The stress tensor can then be defined with Cauchy's theorem

$$\mathbf{t} = \boldsymbol{\sigma}^T \mathbf{n}, \quad (2.36)$$

and the Cauchy stress tensor yields

$$\boldsymbol{\sigma} = [\mathbf{t}_1 \quad \mathbf{t}_2 \quad \mathbf{t}_3]^T = \begin{bmatrix} \sigma_{11} & \tau_{12} & \tau_{13} \\ \tau_{21} & \sigma_{22} & \tau_{23} \\ \tau_{31} & \tau_{32} & \sigma_{33} \end{bmatrix}. \quad (2.37)$$

The Cauchy stress tensor possesses the following symmetry

$$\boldsymbol{\sigma} = \boldsymbol{\sigma}^T, \quad (2.38)$$

which can be shown by the balance of angular momentum for the infinitesimal cube in Fig. 2.7.

2.3 Equilibrium Equation

We consider an arbitrary control volume in mechanical equilibrium in the spatial configuration Ω_t as in Fig. 2.5. The body is subjected to body forces \mathbf{b} , and traction loads \mathbf{t} on the boundary $\partial\Omega_t$. The mechanical equilibrium can then be expressed as

$$\mathbf{p} = \int_{\Omega_t} \rho \mathbf{b} \, dv + \int_{\partial\Omega_t} \mathbf{t} \, da = \mathbf{0}. \quad (2.39)$$

Using Cauchy's theorem from Eq.(2.36) to replace the traction vector \mathbf{t} , Eq. (2.39) can be rearranged to

$$\int_{\Omega_t} \rho \mathbf{b} \, dv + \int_{\partial\Omega_t} \boldsymbol{\sigma} \mathbf{n} \, da = \mathbf{0}. \quad (2.40)$$

The surface term in Eq. (2.40) can be replaced by a volume term with the aid of the divergence theorem

$$\int_{\partial\Omega_t} \boldsymbol{\sigma} \mathbf{n} \, da = \int_{\Omega_t} \operatorname{div} \boldsymbol{\sigma} \, dv. \quad (2.41)$$

Then, the equilibrium equation from Eq. (2.39) yields

$$\int_{\Omega_t} (\rho \mathbf{b} + \operatorname{div} \boldsymbol{\sigma}) \, dv = \mathbf{0}. \quad (2.42)$$

If Eq. (2.42) holds for any arbitrary control volume, the local mechanical equilibrium follows to

$$\operatorname{div} \boldsymbol{\sigma} + \rho \mathbf{b} = \mathbf{0} \quad \text{or} \quad \sigma_{ij,j} + \rho b_i = 0, \quad (2.43)$$

whereas Eq. (2.42) is commonly referred to as the global mechanical equilibrium. In order to derive the equilibrium condition in the reference configuration, Nanson's formula from Eq. (2.11) can be applied

$$\int_{\partial\Omega_t} \boldsymbol{\sigma} \mathbf{n} \, da = \int_{\partial\Omega_0} \boldsymbol{\sigma} J \mathbf{F}^{-T} \mathbf{N} \, dA. \quad (2.44)$$

The right hand side in Eq. (2.44) leads to the definition of the first Piola-Kirchhoff stress tensor

$$\mathbf{P} = J \boldsymbol{\sigma} \mathbf{F}^{-T}, \quad (2.45)$$

which is defined in the reference configuration. The operation in Eq. (2.45) is called *pull back*, since the Cauchy stress tensor is transferred from the current to the reference configuration. Using this expression, Eq. (2.44) can be rearranged to

$$\int_{\partial\Omega_t} \boldsymbol{\sigma} \mathbf{n} \, da = \int_{\partial\Omega_0} \mathbf{P} \mathbf{N} \, dA. \quad (2.46)$$

Then, we can replace the surface term in Eq. (2.39) with the surface term in Eq. (2.46). The volume forces now act on the reference volume with the density ρ_0 , and the equilibrium can be expressed as

$$\int_{\Omega_0} \rho_0 \mathbf{b} \, dV + \int_{\partial\Omega_0} \mathbf{P} \mathbf{N} \, dA = \mathbf{0}. \quad (2.47)$$

Note that due to the mass balance $\rho_0 \, dV = \rho \, dv$, the density can be expressed in the reference configuration as $\rho_0 = J \rho$. In analogy to Eq. (2.41), the utilisation of the divergence theorem yields

$$\int_{\Omega_0} (\rho_0 \mathbf{b} + \text{Div} \mathbf{P}) \, dV = \mathbf{0}, \quad (2.48)$$

where the divergence operator in Eq. (2.48) is defined with respect to the reference configuration. The local form of the equilibrium in the reference configuration follows as

$$\text{Div} \mathbf{P} + \rho_0 \mathbf{b} = \mathbf{0} \quad \text{or} \quad P_{IJ,J} + \rho_0 b_I = 0. \quad (2.49)$$

The first Piola-Kirchhoff stress tensor in Eq. (2.49) was introduced in Eq. (2.45) and is not symmetric. A symmetric stress measure can be obtained by

$$\mathbf{S} = \mathbf{F}^{-1} \mathbf{P} = J \mathbf{F}^{-1} \boldsymbol{\sigma} \mathbf{F}^{-T}, \quad (2.50)$$

which is known as second Piola-Kirchhoff stress tensor.

2.4 Constitutive Laws

2.4.1 Linear Elasticity

A fundamental constitutive relation between stresses and strains can be provided by the concept of linear elasticity, which is premised on the existence of a strain energy potential

$$\psi = \frac{1}{2} \boldsymbol{\varepsilon} : [\mathbb{C} \boldsymbol{\varepsilon}] \quad \text{or} \quad \psi = \frac{1}{2} \varepsilon_{ij} \mathbb{C}_{ijkl} \varepsilon_{kl}. \quad (2.51)$$

The stress is then defined as the derivative of the strain energy function ψ with respect to the strain

$$\boldsymbol{\sigma} = \frac{\partial \psi}{\partial \boldsymbol{\varepsilon}} = \mathbb{C} \boldsymbol{\varepsilon} \quad \text{or} \quad \sigma_{ij} = \mathbb{C}_{ijkl} \varepsilon_{kl}, \quad (2.52)$$

where \mathbb{C} represents the elasticity tensor. The fourth order tensor has the following symmetries due to the symmetry of the stress and strain tensors, and the existence of the potential from Eq. (2.51)

$$\mathbb{C}_{ijkl} = \mathbb{C}_{jikl} = \mathbb{C}_{ijlk} = \mathbb{C}_{klij}, \quad (2.53)$$

which reduce the number of independent constants from 81 to 21. In the case of an isotropic material, the number of constants can be reduced down to only 2. This concept is based on an identical material response in all directions. The required parameters can either be Young's modulus E and Poisson's ratio ν , or Lamé's constants

$$\mu = \frac{E}{2(1+\nu)}, \quad \lambda = \frac{E\nu}{(1+\nu)(1-2\nu)}. \quad (2.54)$$

For isotropic material, Hooke's law can then be defined as

$$\sigma_{ij} = \lambda \varepsilon_{kk} \delta_{ij} + 2\mu \varepsilon_{ij}, \quad (2.55)$$

and the elasticity tensor yields

$$\mathbb{C}_{ijkl} = \lambda \delta_{ij} \delta_{kl} + \mu (\delta_{ik} \delta_{jl} + \delta_{il} \delta_{jk}). \quad (2.56)$$

In various applications it is convenient to express Hooke's law as an additive split in a deviatoric

$$s_{ij} = 2\mu e_{ij} \quad \text{with} \quad e_{ij} = \varepsilon_{ij} - \frac{1}{3} \varepsilon_{kk} \delta_{ij} \quad (2.57)$$

and a volumetric part

$$\sigma_{kk} = 3\kappa \varepsilon_{kk}, \quad (2.58)$$

with the bulk modulus $\kappa = \lambda + \frac{2}{3}\mu$.

2.4.2 Hyperelasticity

The concept of hyperelasticity is applied to materials, which act elastic under finite strains and the method is characterised by the assumption that stresses can be derived from a potential

$$\mathbf{S} = 2 \frac{\partial \Psi(\mathbf{C})}{\partial \mathbf{C}}. \quad (2.59)$$

The potential Ψ in Eq. (2.59) represents a strain energy density function, which in this case is defined with respect to the right Cauchy-Green tensor. The strain energy function can be expressed in terms of the invariants of the right Cauchy-Green tensor if the material is isotropic $\Psi(\mathbf{C}) = \Psi(I_C, II_C, III_C)$. Isotropic materials possess the properties $\Psi(\mathbf{C}) = \Psi(\mathbf{Q}\mathbf{C}\mathbf{Q}^T)$ for all orthogonal tensors \mathbf{Q} . The invariants of the right Cauchy-Green tensor are defined as

$$\begin{aligned} I_C &= \text{tr } \mathbf{C} = C_{II} \\ II_C &= \frac{1}{2} [(\text{tr } \mathbf{C})^2 - \text{tr } (\mathbf{C}^2)] = \frac{1}{2} (C_{II} C_{JJ} - C_{IJ} C_{IJ}) \\ III_C &= \det \mathbf{C} = \epsilon_{IJK} C_{1I} C_{2J} C_{3K}, \end{aligned} \quad (2.60)$$

where ϵ_{IJK} is the permutation symbol, which is defined as

$$\epsilon_{IJK} = \begin{cases} 1 & \text{for even permutations (i.e. } \epsilon_{123} = \epsilon_{231} = \epsilon_{312} = 1) \\ -1 & \text{for odd permutations (i.e. } \epsilon_{321} = \epsilon_{132} = \epsilon_{213} = -1) \\ 0 & \text{if any two indices are equal (e.g. } \epsilon_{112} = \epsilon_{333} = 0). \end{cases} \quad (2.61)$$

With the invariants, the second Piola-Kirchhoff stress in Eq. (2.59) can be expressed as

$$\mathbf{S} = 2 \left[\left(\frac{\partial \Psi}{\partial I_C} + I_C \frac{\partial \Psi}{\partial II_C} \right) \mathbf{1} - \frac{\partial \Psi}{\partial II_C} \mathbf{C} + III_C \frac{\partial \Psi}{\partial III_C} \mathbf{C}^{-1} \right], \quad (2.62)$$

and the derivatives in Eq. (2.62) are defined as

$$\frac{\partial I_C}{\partial \mathbf{C}} = \mathbf{1}, \quad \frac{\partial II_C}{\partial \mathbf{C}} = I_C \mathbf{1} - \mathbf{C}, \quad \frac{\partial III_C}{\partial \mathbf{C}} = III_C \mathbf{C}^{-1}. \quad (2.63)$$

In this work a compressible neo-Hookian material is used, which is defined as a function of the first invariant of the right Cauchy-Green tensor and the determinant J of the deformation gradient

$$\Psi(I_C, J) = \frac{\mu}{2}(I_C - 3) + \frac{\lambda}{4}(J^2 - 1) - \ln J \left(\frac{\lambda}{2} + \mu \right). \quad (2.64)$$

Elastic materials often show a nearly incompressible behaviour under finite deformations. Therefore, the strain energy function has to fulfil the conditions

$$\lim_{J \rightarrow +\infty} \Psi \rightarrow \infty \quad \text{and} \quad \lim_{J \rightarrow 0} \Psi \rightarrow \infty. \quad (2.65)$$

By inserting the strain energy function of Eq. (2.64) into Eq. (2.62) and considering the derivatives of the invariants in Eq. (2.63), the second Piola-Kirchhoff stress tensor yields

$$\mathbf{S} = \frac{\lambda}{2}(J^2 - 1) \mathbf{C}^{-1} + \mu(\mathbf{1} - \mathbf{C}^{-1}). \quad (2.66)$$

In Eq. (2.66) another important property of the strain energy function can be observed. The stresses vanish $\mathbf{S} = \mathbf{0}$ in the case of an unstretched material $\mathbf{C} = \mathbf{1}$. In the spatial configuration, the stresses are expressed by the Cauchy stress tensor and the constitutive law can be obtained by a push forward of Eq. (2.66). The Cauchy stress is then defined as

$$\boldsymbol{\sigma} = \frac{\lambda}{2J}(J^2 - 1) \mathbf{1} + \frac{\mu}{J}(\mathbf{b} - \mathbf{1}). \quad (2.67)$$

2.4.3 Von Mises Plasticity

An additive split of the linearised strain tensor in an elastic and plastic part

$$\boldsymbol{\varepsilon} = \boldsymbol{\varepsilon}^e + \boldsymbol{\varepsilon}^p \quad (2.68)$$

is established. Since stress only depends on elastic strain $\boldsymbol{\varepsilon}^e$, the constitutive relation is defined as

$$\boldsymbol{\sigma} = \mathbb{C} \boldsymbol{\varepsilon}^e = \mathbb{C}(\boldsymbol{\varepsilon} - \boldsymbol{\varepsilon}^p), \quad (2.69)$$

where \mathbb{C} is the isotropic elasticity tensor from Eq. (2.56). It is often assumed that plastic deformation is driven through deviatoric stresses. Therefore, we neglect the volumetric stresses in the following and make use of the elastic law for the deviatoric stresses

$$\mathbf{s} = 2\mu(\mathbf{e} - \mathbf{e}^p). \quad (2.70)$$

In order to decide whether a material deforms plastically, a yield criterion is defined

$$f(\mathbf{s}, q) = 0, \quad (2.71)$$

where $q = q(\psi)$ is used to model strain hardening and ψ is the hardening variable. In this work a power law of the form

$$q(\psi) = \sigma_y + k \psi^m \quad (2.72)$$

is used to model hardening. In this context σ_y describes an initial or virgin yield stress, and k is often referred to as the hardening modulus. For the case of isotropic hardening, the von Mises plasticity is often used. Thus, the yield function is defined as

$$f(\mathbf{s}, q) = \sigma_v - q(\psi), \quad (2.73)$$

where σ_v is the von Mises stress, which provides the name to the method (see Gross and Seelig (2016)). The von Mises stress is defined as

$$\sigma_v = \sqrt{3 \mathbb{I}_s} \quad (2.74)$$

with the second invariant of the deviatoric stresses

$$\mathbb{I}_s = \frac{1}{2} \|\mathbf{s}\|^2. \quad (2.75)$$

Consequently, the yield function can be expressed in the way, which is commonly found in literature

$$f(\mathbf{s}, q) = \|\mathbf{s}\| - \sqrt{\frac{2}{3}} q(\psi). \quad (2.76)$$

Since Eq. (2.76) only depends on the second invariant of the deviatoric stresses, this approach is often referred to as J_2 -plasticity. In order to determine the plastic strain rate $\dot{\mathbf{e}}^p$, a flow rule is required as well as an evolution law for the hardening variable ψ . The plastic flow is proportional to the derivative of the yield function with respect to the deviatoric stress

$$\dot{\mathbf{e}}^p = \gamma \frac{\partial f}{\partial \mathbf{s}} = \gamma \frac{\mathbf{s}}{\|\mathbf{s}\|} = \gamma \mathbf{N}(\mathbf{s}). \quad (2.77)$$

Eq. (2.77) is called the flow rule and $\gamma \geq 0$ represents a plastic multiplier. The direction of the plastic flow in Eq. (2.77) is governed by $\mathbf{N}(\mathbf{s})$. The evolution law for the hardening variable can be derived in a similar fashion by

$$\dot{\psi} = \gamma \frac{\partial f}{\partial q} = \sqrt{\frac{2}{3}} \gamma. \quad (2.78)$$

In order to decide whether or not a deformation is plastic and then compute the plastic multiplier $\gamma = \|\dot{\mathbf{e}}^P\|$, Eq. (2.71) has to be evaluated. The yield criterion classifies the material response into the two cases

$$\begin{aligned} f(\mathbf{s}, q) < 0 &\rightsquigarrow \text{elastic} \rightsquigarrow \gamma = 0 \\ f(\mathbf{s}, q) = 0 &\rightsquigarrow \text{plastic} \rightsquigarrow \gamma \geq 0. \end{aligned} \quad (2.79)$$

From these equations one can conclude that $\gamma f(\mathbf{s}, q) = 0$, and the Kuhn-Tucker conditions can be defined as

$$\gamma \geq 0, \quad f(\mathbf{s}, q) \leq 0, \quad \gamma f(\mathbf{s}, q) = 0. \quad (2.80)$$

To fully describe elasto-plasticity, the loading conditions have to be studied on a plasticly deformed material. Therefore, a material point at time t^* is considered, at which the material is plasticly deformed, i.e. $f = 0$. Then the loading/unloading conditions follow to

$$\begin{aligned} \dot{f} > 0 &\rightsquigarrow \text{inadmissible} \\ \dot{f} = 0 &\rightsquigarrow \text{plastic loading} \rightsquigarrow \gamma > 0 \\ \dot{f} < 0 &\rightsquigarrow \text{elastic unloading} \rightsquigarrow \gamma = 0, \end{aligned} \quad (2.81)$$

which can be summarised to the so called consistency condition

$$\gamma \dot{f}(\mathbf{s}, q) = 0 \quad \text{for} \quad f(\mathbf{s}, q) = 0. \quad (2.82)$$

Chapter 3

Numerical Implementation

In this chapter the derivation of triangular finite elements is demonstrated in the context of finite strains. At first, the weak form of the equilibrium equation is introduced and the linearisation is demonstrated in the following section. Furthermore, the spatial discretisation, and the numerical integration are briefly explained. The following section is concerned with the integration of inelastic constitutive equations, and the chapter closes with some remarks on the solution of nonlinear problems. For more details on the theory, the reader is referred to textbooks on nonlinear finite elements such as Wriggers (2001); Bathe (2006); Zienkiewicz and Taylor (2000a,b); Bonet and Wood (2008); Simo and Hughes (2000); de Souza Neto et al. (2011).

3.1 Weak Form of Equilibrium Equation

In order to derive finite element formulations, the equilibrium in Eq. (2.49) is transferred to the so called weak form. The weak form can be obtained by scalar multiplication of Eq. (2.49) with a vector-valued test function $\delta \mathbf{x}$, and integration over the domain Ω_0

$$\int_{\Omega_0} (\text{Div} \mathbf{P} + \rho_0 \mathbf{b}) \cdot \delta \mathbf{x} \, dV = 0. \quad (3.1)$$

The test function $\delta \mathbf{x}$ can also be interpreted as a virtual displacement. Analog to the strong form in Eq. (2.49), the stresses in Eq. (3.1) are represented by the first Piola-Kirchhoff tensor \mathbf{P} , and $\rho_0 \mathbf{b}$ is a body force. Using the product rule $\text{Div} \mathbf{P} \cdot \delta \mathbf{x} = P_{iJ,J} \delta x_i = (P_{iJ} \delta x_i)_{,J} - P_{iJ} \delta x_{i,J}$, Eq. (3.1) can be rearranged to

$$\int_{\Omega_0} \text{Div} (\mathbf{P} \delta \mathbf{x}) \, dV - \int_{\Omega_0} \mathbf{P} : \text{Grad} \delta \mathbf{x} \, dV + \int_{\Omega_0} \rho_0 \mathbf{b} \cdot \delta \mathbf{x} \, dV = 0. \quad (3.2)$$

The divergence theorem (or Gauß theorem) describes the transformation of a volume integral into a surface integral. Applied to the first term in Eq. (3.2), the Gauß theorem yields

$$\int_{\Omega_0} \text{Div}(\mathbf{P} \delta \mathbf{x}) \, dV = \int_{\partial \Omega_0^\sigma} (\mathbf{P} \mathbf{N}) \cdot \delta \mathbf{x} \, dA. \quad (3.3)$$

By applying the Cauchy theorem $\mathbf{P} \mathbf{N} = \mathbf{t}_0$ on the boundary $\partial \Omega_0^\sigma$ and making use of $\mathbf{P} : \text{Grad} \delta \mathbf{x} = \mathbf{P} : \delta \mathbf{F}$, the weak form in the reference configuration yields

$$G = \int_{\Omega_0} \mathbf{P} : \delta \mathbf{F} \, dV - \int_{\partial \Omega_0^\sigma} \mathbf{t}_0 \cdot \delta \mathbf{x} \, dA - \int_{\Omega_0} \rho_0 \mathbf{b} \cdot \delta \mathbf{x} \, dV = 0 \quad \forall \delta \mathbf{x}. \quad (3.4)$$

The boundary of the domain is partitioned as $\partial \Omega_0 = \partial \Omega_0^u \cup \partial \Omega_0^\sigma$ and Dirichlet boundary conditions $\mathbf{x} = \mathbf{x}^*$ are defined on $\partial \Omega_0^u$ as well as Neumann boundary conditions $\mathbf{P} \mathbf{N} = \mathbf{t}_0$ on $\partial \Omega_0^\sigma$. The test function vanishes i.e. $\delta \mathbf{x} = \mathbf{0}$ on the boundary $\partial \Omega_0^u$. In order to obtain the weak form in the spatial configuration, a push forward is applied to Eq. (3.4). The push forward $\mathbf{P} : \delta \mathbf{F} = J \boldsymbol{\sigma} : \text{grad}_s \delta \mathbf{x}$ in conjunction with $dv = J \, dV$ leads to

$$\int_{\Omega_0} \mathbf{P} : \delta \mathbf{F} \, dV = \int_{\Omega_t} \boldsymbol{\sigma} : \text{grad}_s \delta \mathbf{x} \, dv. \quad (3.5)$$

In Eq. (3.5) the term grad_s can be used because of the symmetry of the Cauchy stress tensor. The boundary term in Eq. (3.4) can be expressed in the spatial configuration as

$$\int_{\partial \Omega_0^\sigma} \mathbf{t}_0 \cdot \delta \mathbf{x} \, dA = \int_{\partial \Omega_0^\sigma} (\mathbf{P} \mathbf{N}) \cdot \delta \mathbf{x} \, dA = \int_{\partial \Omega_t^\sigma} (\boldsymbol{\sigma} \mathbf{n}) \cdot \delta \mathbf{x} \, da = \int_{\partial \Omega_t^\sigma} \mathbf{t} \cdot \delta \mathbf{x} \, da, \quad (3.6)$$

and the body force term can be transferred to the spatial configuration as

$$\int_{\Omega_0} \rho_0 \mathbf{b} \cdot \delta \mathbf{x} \, dV = \int_{\Omega_t} \rho_0 \frac{1}{J} \mathbf{b} \cdot \delta \mathbf{x} \, dv = \int_{\Omega_t} \rho \mathbf{b} \cdot \delta \mathbf{x} \, dv. \quad (3.7)$$

As a result of Eq. (3.5) - (3.7), the weak form in the spatial configuration yields

$$g = \int_{\Omega_t} \boldsymbol{\sigma} : \text{grad}_s \delta \mathbf{x} \, dv - \int_{\partial \Omega_t^\sigma} \mathbf{t} \cdot \delta \mathbf{x} \, da - \int_{\Omega_t} \rho \mathbf{b} \cdot \delta \mathbf{x} \, dv = 0 \quad \forall \delta \mathbf{x}. \quad (3.8)$$

3.2 Linearisation of the Weak Form

The weak forms in Eq. (3.8) and Eq. (3.4) represent nonlinear functions of the displacements. In nonlinear finite element theory it is common to approximate weak forms by a Taylor series expansion. A linear approximation of G from the weak form $G = 0$ can be obtained by a Taylor series expansion

$$\mathcal{L}[G]_{\mathbf{x}=\bar{\mathbf{x}}} = G(\bar{\mathbf{x}}, \delta \mathbf{x}) + \text{D}G(\bar{\mathbf{x}}, \delta \mathbf{x}) \cdot \Delta \mathbf{u}, \quad (3.9)$$

that is terminated after the linear term. The linearisation in Eq. (3.9) is evaluated at the position $\mathbf{x} = \bar{\mathbf{x}}$ and $\Delta \mathbf{u}$ represents a displacement increment. Therefore, $G(\bar{\mathbf{x}}, \delta \mathbf{x})$ is the weak form evaluated at position $\bar{\mathbf{x}}$ and the term $D G(\bar{\mathbf{x}}, \delta \mathbf{x})$ acts as a tangent. The tangent for the weak form in the reference configuration from Eq. (3.4) then follows with $\mathbf{P} = \mathbf{F}\mathbf{S}$ to

$$\begin{aligned} D G(\bar{\mathbf{x}}, \delta \mathbf{x}) \cdot \Delta \mathbf{u} &= \int_{\Omega_0} [D \mathbf{P}(\bar{\mathbf{x}}) \cdot \Delta \mathbf{u}] : \text{Grad } \delta \mathbf{x} \, dV \\ &= \int_{\Omega_0} (\text{Grad } \Delta \mathbf{u} \bar{\mathbf{S}} + \bar{\mathbf{F}} [D \mathbf{S}(\bar{\mathbf{x}}) \cdot \Delta \mathbf{u}]) : \text{Grad } \delta \mathbf{x} \, dV. \end{aligned} \quad (3.10)$$

In Eq. (3.10) the surface and body loads are neglected and $D \mathbf{S}(\bar{\mathbf{x}})$ is the tangent of the second Piola Kirchhoff stress tensor. By expressing the tangent as

$$D \mathbf{S}(\bar{\mathbf{x}}) \cdot \Delta \mathbf{u} = \bar{\mathbb{C}} [\Delta \bar{\mathbf{E}}], \quad (3.11)$$

we can rearrange the linearisation of the weak form to

$$\begin{aligned} D G(\bar{\mathbf{x}}, \delta \mathbf{x}) \cdot \Delta \mathbf{u} &= \int_{\Omega_0} (\text{Grad } \Delta \mathbf{u} \bar{\mathbf{S}} + \bar{\mathbf{F}} \bar{\mathbb{C}} [\Delta \bar{\mathbf{E}}]) : \text{Grad } \delta \mathbf{x} \, dV \\ &= \int_{\Omega_0} (\text{Grad } \Delta \mathbf{u} \bar{\mathbf{S}} : \text{Grad } \delta \mathbf{x} + \delta \bar{\mathbf{E}} : \bar{\mathbb{C}} [\Delta \bar{\mathbf{E}}]) \, dV. \end{aligned} \quad (3.12)$$

In Eq. (3.12) the fourth order tensor $\bar{\mathbb{C}}$ results from the linearisation of the second Piola-Kirchhoff tensor and is often referred to as material tangent. The material tangent depends on the constitutive law and can be found in literature as Holzapfel (2000); Wriggers (2001), for hyperelastic materials as described in Sec. 2.4.2. A material law to model elasto-plasticity at finite deformations is considered in this work as well and is explained in more detail in Sec. 3.5.2. The respective material tangent can be found in Cuitiño and Ortiz (1992); Montáns and Bathe (2003); de Souza Neto et al. (2011). In order to express the linearisation of the weak form in the spatial configuration, a push forward is applied to Eq. (3.12). Then the first term in Eq. (3.12) can be expressed as

$$\text{Grad } \Delta \mathbf{u} \bar{\mathbf{S}} : \text{Grad } \delta \mathbf{x} = \overline{\text{grad}} \Delta \mathbf{u} J \bar{\boldsymbol{\sigma}} : \overline{\text{grad}} \delta \mathbf{x}, \quad (3.13)$$

and the second term in Eq. (3.12) yields

$$\delta \bar{\mathbf{E}} : \bar{\mathbb{C}} [\Delta \bar{\mathbf{E}}] = \overline{\text{grad}}_s \delta \mathbf{x} : \bar{\mathbb{c}} \overline{\text{grad}}_s \Delta \mathbf{u}. \quad (3.14)$$

In Eq. (3.14) the fourth order tensor $\bar{\mathbb{c}}$ symbolises the material tangent in the spatial configuration, which is computed with

$$\bar{\mathfrak{c}}_{ijkl} = \bar{F}_{iA} \bar{F}_{jB} \bar{F}_{kC} \bar{F}_{lD} \bar{\mathfrak{C}}_{ABCD}. \quad (3.15)$$

Finally, with $\hat{\mathfrak{c}} = \bar{\mathfrak{c}}/\bar{J}$, the linearisation of the weak form in the spatial configuration can be expressed as

$$Dg(\bar{\mathbf{x}}, \delta\mathbf{x}) \cdot \Delta\mathbf{u} = \int_{\Omega_t} (\overline{\text{grad}} \Delta\mathbf{u} \bar{\boldsymbol{\sigma}} : \overline{\text{grad}} \delta\mathbf{x} + \overline{\text{grad}}_s \delta\mathbf{x} : \hat{\mathfrak{c}} \overline{\text{grad}}_s \Delta\mathbf{u}) dv \quad (3.16)$$

3.3 Spatial Discretisation

The combination of kinematics, constitutive law, equilibrium equation, and boundary conditions defines the boundary value problem *BVP*. In the following, the two dimensional body \mathcal{B} is discretised with finite elements Ω^e as shown in Fig. 3.1. The discretised body \mathcal{B}^h then consists of the assembly of finite elements as in Eq. (3.17), and the boundary $\partial\mathcal{B}$ transforms to $\partial\mathcal{B}^h$.

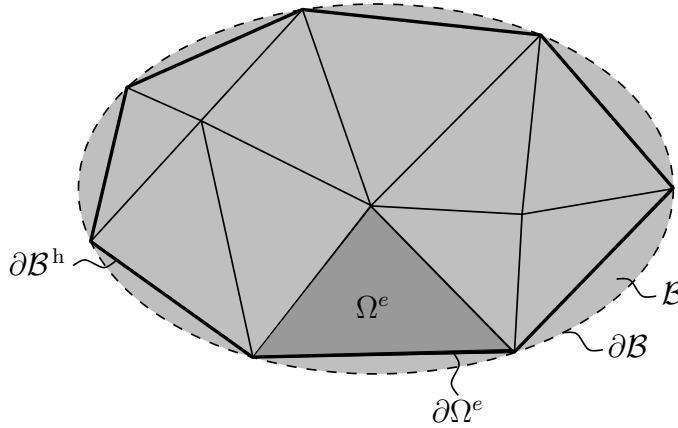


Fig. 3.1: Discretised body \mathcal{B}

$$\mathcal{B} \approx \mathcal{B}^h = \bigcup_{e=1}^{n^e} \Omega^e \quad (3.17)$$

In order to simplify the meshing procedure in every PFEM loading step, triangular isoparametric finite elements are used. In the isoparametric concept, the coordinates of a finite element are transformed from a global system to a reference system, in which the integration is carried out. The name of the concept stems from the idea that the same shape functions can be used to approximate the geometry of the body, as well as the unknown displacements. Figure 3.2 shows a finite element in the reference configuration Ω_0^e , the spatial configuration Ω_t^e , as well as the isoparametric element Ω_Δ^e .

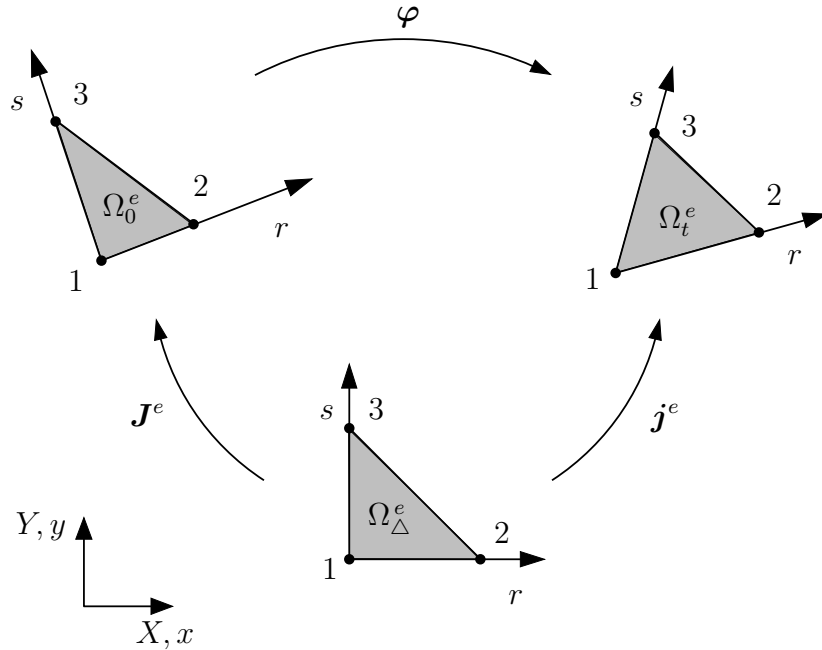


Fig. 3.2: Isoparametric triangular finite element for finite deformations

In this context, the matrix \mathbf{j}^e transforms the coordinates of the isoparametric element to the spatial coordinates, and \mathbf{J}^e transforms the element coordinates to the reference coordinates. The isoparametric element is defined in the coordinates r and s . In Fig. 3.2, φ represents the deformation of the element from the reference, to the spatial configuration. The geometry in both configurations, and the displacements are approximated using so called shape functions

$$\mathbf{X}^e = \sum_{I=1}^N N_I \mathbf{X}_I, \quad \mathbf{x}^e = \sum_{I=1}^N N_I \mathbf{x}_I, \quad \mathbf{u}^e = \sum_{I=1}^N N_I \mathbf{u}_I, \quad (3.18)$$

where N represents the number of nodes per element i.e. $N = 3$. In this work linear shape functions are used, which are defined in isoparametric coordinates

$$N_1 = 1 - r - s, \quad N_2 = r, \quad N_3 = s. \quad (3.19)$$

Within a finite element the displacement gradient can then be computed using the

shape functions. The displacement gradient with respect to the reference coordinates yields

$$\text{Grad } \mathbf{u}^e = \sum_{I=1}^N \mathbf{u}_I \otimes \text{Grad } N_I = \sum_{I=1}^N \mathbf{u}_I \otimes N_{I,\mathbf{X}}, \quad (3.20)$$

and the gradient with respect to the spatial coordinates follows as

$$\text{grad } \mathbf{u}^e = \sum_{I=1}^N \mathbf{u}_I \otimes \text{grad } N_I = \sum_{I=1}^N \mathbf{u}_I \otimes N_{I,\mathbf{x}}. \quad (3.21)$$

The derivatives of the shape functions in Eq. (3.20) and (3.21) are calculated using the transformation matrices \mathbf{J}^e and \mathbf{j}^e respectively. The gradient of the shape functions with respect to the spatial configuration in Eq. (3.21) can therefore be expressed as

$$\text{grad } N_I = \begin{bmatrix} N_{I,x} \\ N_{I,y} \end{bmatrix} = (\mathbf{j}^e)^{-T} \begin{bmatrix} N_{I,r} \\ N_{I,s} \end{bmatrix} \quad \text{with} \quad \mathbf{j}^e = \begin{bmatrix} \frac{\partial x}{\partial r} & \frac{\partial x}{\partial s} \\ \frac{\partial y}{\partial r} & \frac{\partial y}{\partial s} \end{bmatrix}. \quad (3.22)$$

In the following, the discretisation of the weak form in the spatial configuration from Eq. (3.8) is demonstrated for neglected body forces and surface loads. Then, the term $\text{grad}_s \delta \mathbf{x}$ from Eq. (3.8) can be discretised with

$$\text{grad}_s \delta \mathbf{x} \approx \frac{1}{2} \sum_{I=1}^N (\delta \mathbf{x}_I \otimes N_{I,\mathbf{x}} + N_{I,\mathbf{x}} \otimes \delta \mathbf{x}_I) = \sum_{I=1}^N \underline{\mathbf{B}}_I \delta \mathbf{x}_I \quad (3.23)$$

where the under bar symbolises the Voigt or matrix notation. The matrix $\underline{\mathbf{B}}_I$ contains the derivatives of the shape functions and - as the Cauchy stresses - is structured using the Voigt notation

$$\underline{\mathbf{B}}_I = \begin{bmatrix} N_{I,x} & 0 \\ 0 & N_{I,y} \\ N_{I,y} & N_{I,x} \end{bmatrix}, \quad \text{and} \quad \underline{\boldsymbol{\sigma}} = \begin{bmatrix} \sigma_{xx} \\ \sigma_{yy} \\ \sigma_{xy} \end{bmatrix}. \quad (3.24)$$

The discretisation of the internal virtual work can then be expressed as

$$\begin{aligned} \int_{\Omega_t} \text{grad}_s \delta \mathbf{x} : \boldsymbol{\sigma} \, da &\approx \bigcup_{e=1}^{n^e} \int_{\Omega_t^e} (\text{grad}_s \delta \mathbf{x})^T \underline{\boldsymbol{\sigma}} \, da \\ &= \bigcup_{e=1}^{n^e} \sum_{I=1}^N \delta \mathbf{x}_I^T \int_{\Omega_t^e} \underline{\mathbf{B}}_I^T \underline{\boldsymbol{\sigma}} \, da \\ &= \bigcup_{e=1}^{n^e} \sum_{I=1}^N \delta \mathbf{x}_I^T \mathbf{r}_I^e(\mathbf{u}^e) = \delta \underline{\mathbf{x}}^T \underline{\mathbf{r}}(\underline{\mathbf{u}}) \end{aligned} \quad (3.25)$$

In Eq. (3.25) the discretised internal virtual work is expressed as an assembly of the virtual internal work of all finite elements n^e . The global discretised nonlinear system then yields

$$g(\underline{\mathbf{u}}, \delta \underline{\mathbf{x}}) = \delta \underline{\mathbf{x}}^T (\underline{\mathbf{r}}(\underline{\mathbf{u}}) - \underline{\mathbf{p}}) = 0, \quad (3.26)$$

where $\underline{\mathbf{r}}$ is often referred to as residual. The load term $\underline{\mathbf{p}}$ is neglected in the linearisation in Eq. (3.16) due to the assumption that the load is independent of the deformation of the body and will therefore not be considered in the discretisation. Since a linearised system is solved to approximate the solution of the nonlinear problem, the discretisation of the increment of the weak form in Eq. (3.16) is required. Applying the discretisations

$$\overline{\text{grad}} \Delta \underline{\mathbf{u}} = \sum_{J=1}^N \Delta \underline{\mathbf{u}}_J \otimes N_{J,\mathbf{x}}, \quad \text{and} \quad \overline{\text{grad}} \delta \underline{\mathbf{x}} = \sum_{I=1}^N \delta \underline{\mathbf{x}}_I \otimes N_{I,\mathbf{x}} \quad (3.27)$$

to Eq. (3.16), the discretisation of the first term in Eq. (3.16) can be expressed as

$$\int_{\Omega_t} (\overline{\text{grad}} \Delta \underline{\mathbf{u}} \boldsymbol{\sigma} : \overline{\text{grad}} \delta \underline{\mathbf{x}}) da \approx \bigcup_{e=1}^{n^e} \sum_{I=1}^N \sum_{J=1}^N \delta \underline{\mathbf{x}}_I^T \left(\int_{\Omega_t^e} \overline{g}_{IJ} \mathbf{1} da \right) \Delta \underline{\mathbf{u}}_J. \quad (3.28)$$

The upper bound of summation N in Eq. (3.27) and (3.28) corresponds to the number of nodes per element and the scalars \overline{g}_{IJ} in Eq. (3.28) are called geometrical stiffness. The geometrical stiffness is calculated as

$$\overline{g}_{IJ} = \begin{bmatrix} N_{I,x} & N_{I,y} \end{bmatrix} \begin{bmatrix} \sigma_{xx} & \sigma_{xy} \\ \text{sym} & \sigma_{yy} \end{bmatrix} \begin{bmatrix} N_{J,x} \\ N_{J,y} \end{bmatrix}. \quad (3.29)$$

The second term in Eq. (3.16) is called material stiffness and is discretised using the matrix $\underline{\mathbf{B}}_I$ from Eq. (3.24)

$$\int_{\Omega_t} (\overline{\text{grad}}_s \delta \underline{\mathbf{x}} : \hat{\mathbf{c}} \overline{\text{grad}}_s \delta \Delta \underline{\mathbf{u}}) da \approx \bigcup_{e=1}^{n^e} \sum_{I=1}^N \sum_{J=1}^N \delta \underline{\mathbf{x}}_I^T \left(\int_{\Omega_t^e} \underline{\mathbf{B}}_I^T \hat{\mathbf{c}} \underline{\mathbf{B}}_J da \right) \Delta \underline{\mathbf{u}}_J. \quad (3.30)$$

Therefore, the discretisation of the linearised system yields

$$Dg(\overline{\mathbf{x}}, \delta \underline{\mathbf{x}}) \cdot \Delta \underline{\mathbf{u}} \approx \bigcup_{e=1}^{n^e} \sum_{I=1}^N \sum_{J=1}^N \delta \underline{\mathbf{x}}_I^T \underline{\mathbf{k}}_{IJ}^e \Delta \underline{\mathbf{u}}_J, \quad (3.31)$$

where the tangential stiffness matrix is defined as

$$\underline{\mathbf{k}}_{IJ}^e = \int_{\Omega_t^e} (\overline{g}_{IJ} \mathbf{1} + \underline{\mathbf{B}}_I^T \hat{\mathbf{c}} \underline{\mathbf{B}}_J) da. \quad (3.32)$$

In Eq. (3.31) the tangential stiffness matrices of all elements n^e are assembled to form the global tangential stiffness matrix. An explanation on how the solution of the nonlinear system is approximated using the linearisation is provided in Sec. 3.6.

3.4 Numerical Integration

Prior to the assembly of the global residual and tangent, the integrals of the element residual and tangent in Eqs. (3.25) and (3.32) are numerically evaluated. The numerical integration is executed in the isoparametric parameter space using Gauß quadrature. In order to facilitate the procedure, the integrals are transformed using the determinant of the transformation matrix \mathbf{j}^e

$$\int_{\Omega_t^e} g(\mathbf{x}) \, da = \int_{\Omega_\Delta} g(\mathbf{r}) \det \mathbf{j}^e \, d\Delta = \int_0^1 \int_0^{1-r} g(r, s) \det \mathbf{j}^e \, ds \, dr. \quad (3.33)$$

In this work, a two dimensional approach is used in conjunction with triangular finite elements and linear shape functions. The right hand side in Eq. (3.33) is then approximated by

$$\int_0^1 \int_0^{1-r} g(r, s) \det \mathbf{j}^e \, ds \, dr \approx \sum_{p=1}^{n_p} g(r_p, s_p) \det \mathbf{j}^e w_p, \quad (3.34)$$

where the number of integration points is characterised by n_p , w_p is the integration weight, and the coordinates of the integration points are $\mathbf{r}_p = [r_p, s_p]^T$. Then, the integral of the internal virtual work from Eq. (3.25) yields

$$\underline{\mathbf{r}}_I^e = \int_{\Omega_t^e} \underline{\mathbf{B}}_I^T \underline{\boldsymbol{\sigma}} \, da \approx \sum_{p=1}^{n_p} \Delta \underline{\mathbf{B}}_I^T \Delta \underline{\boldsymbol{\sigma}} \det \mathbf{j}^e w_p. \quad (3.35)$$

In Eq. (3.35) and (3.36) a more compact notation is used to express quantities with respect to the isoparametric coordinates $\Delta \underline{\boldsymbol{\sigma}} = \underline{\boldsymbol{\sigma}}(r_p, s_p)$. The element tangent from Eq. (3.32) is computed with

$$\underline{\mathbf{k}}_{IJ}^e = \int_{\Omega_t^e} (\bar{g}_{IJ} \mathbf{1} + \underline{\mathbf{B}}_I^T \hat{\underline{\mathbf{c}}} \underline{\mathbf{B}}_J) \, dv \approx \sum_{p=1}^{n_p} \left(\Delta \bar{g}_{IJ} \mathbf{1} + \Delta \underline{\mathbf{B}}_I^T \Delta \hat{\underline{\mathbf{c}}} \Delta \underline{\mathbf{B}}_J \right) \det \mathbf{j}^e w_p. \quad (3.36)$$

For triangular finite elements with linear shape functions used in this work, the parameters for the Gauß quadrature are shown in Tab. 3.1.

n_p	r_p	s_p	w_p
1	1/3	1/3	1/2

Table 3.1: Parameters for Gauß integration in triangular elements with linear shape functions

3.5 Local Integration of Inelastic Constitutive Relations

3.5.1 Return Mapping Algorithm for Small Strain Plasticity

In this work an implicit Euler scheme is used for the integration of the constitutive equations, which is often referred to as return mapping algorithm in literature. Since the constitutive equations have to be fulfilled at every point of the material, time integration is performed at every Gauß point in a discretised finite element domain. In the following we restrict ourselves to the von Mises model with isotropic hardening as described in Sec. 2.4.3. At the beginning of the algorithm a trial deviatoric stress is computed

$$\mathbf{s}_{n+1}^{\text{tr}} = 2\mu(\mathbf{e}_{n+1} - \mathbf{e}_n^{\text{p}}), \quad (3.37)$$

as well as a trial state for the yield function

$$f_{n+1} = \|\mathbf{s}_{n+1}^{\text{tr}}\| - \sqrt{\frac{2}{3}}q(\psi_n). \quad (3.38)$$

In Eq. (3.37) and (3.38) \mathbf{e}_{n+1} is the total deviatoric strain from time step $n + 1$, \mathbf{e}_n^{p} represents the plastic strain of the previous time step n , and ψ_n is the hardening variable. Then, the yield function from Eq. (3.38) is evaluated.

- ★ If $f_{n+1} < 0$ The plastic multiplier $\Delta\gamma = 0$, the plastic strain remains unchanged $\mathbf{e}_{n+1}^{\text{p}} = \mathbf{e}_n^{\text{p}}$, as well as the hardening variable $\psi_{n+1} = \psi_n$. In this case, the deviatoric stress coincides with the deviatoric trial stress $\mathbf{s}_{n+1} = \mathbf{s}_{n+1}^{\text{tr}}$.
- ★ If $f_{n+1} \geq 0$ holds, then the deformation is plastic, which means that the plastic multiplier $\Delta\gamma > 0$ and has to be determined. Since in this work, a nonlinear function is used to model isotropic hardening, the strain increment is computed using a Newton scheme. In this procedure the stress is computed using a predictor-corrector method, where the trial stress acts as a stress prediction,

and a corrector term can be formed with the plastic multiplier yielding the stress update formula

$$\mathbf{s}_{n+1} = 2\mu (\mathbf{e}_{n+1} - \mathbf{e}_{n+1}^p) = \underbrace{\mathbf{s}_{n+1}^{\text{tr}}}_{\text{predictor}} - \underbrace{2\mu\Delta\gamma\mathbf{N}_{n+1}}_{\text{corrector}}. \quad (3.39)$$

With Eq. (3.39) we can rearrange the yield condition in order to form a residual for the iterative computation of $\Delta\gamma$ to

$$r^i = f_{n+1} = \|\mathbf{s}_{n+1}^{\text{tr}}\| - 2\mu\Delta\gamma - \sqrt{\frac{2}{3}}q(\psi_n) < \text{TOL}, \quad (3.40)$$

where ψ is updated by the evolution law

$$\psi_{n+1}^{i+1} = \psi_n + \sqrt{\frac{2}{3}}\Delta\gamma_{n+1}^{i+1}. \quad (3.41)$$

Another crucial part for Newton's method is the tangent to the residual, which is computed as the derivative of the residual with respect to the plastic multiplier

$$t^i = \frac{\partial r^i}{\partial \Delta\gamma} = -2\mu - \sqrt{\frac{2}{3}} \frac{\partial q(\psi)}{\partial \psi} \frac{\partial \psi}{\partial \Delta\gamma} = -2\mu - \frac{2}{3}q'(\psi). \quad (3.42)$$

The value for $\Delta\gamma$ can then be updated in every iteration by

$$\Delta\gamma^{i+1} = \Delta\gamma^i - \frac{r^i}{t^i}. \quad (3.43)$$

Since the local Newton scheme is applied in every time step $n+1$, the indices in Eq. (3.42) and (3.43) are neglected in order to not overload the notation. The employed Newton scheme for the computation of $\Delta\gamma$ is outlined in Alg. 1.

```

input :  $\Delta\gamma^i = 0, \psi^i$ 
output:  $\Delta\gamma_{n+1}^{i+1}$ 
while  $|r^i| = \|\mathbf{s}_{n+1}^{\text{tr}}\| - 2\mu\Delta\gamma^i - \sqrt{2/3}q(\psi^i) < TOL$  do
     $t^i = -2/3q'(\psi^i) - 2\mu$ 
     $\Delta\gamma^{i+1} = \Delta\gamma^i - r^i/t^i$ 
     $\psi^{i+1} = \psi^i + \sqrt{2/3}\Delta\gamma^{i+1}$ 
end
    
```

Algorithm 1: Solve nonlinear yield condition (`gamma_solve`)

With the solution $\Delta\gamma_{n+1}^{i+1}$ for $|r^{i+1}| < \text{TOL}$, the plastic strain, the stress, and the hardening variable can be updated by

$$\begin{aligned} \mathbf{e}_{n+1}^p &= \mathbf{e}_n^p + \Delta\gamma_{n+1} \mathbf{N}_{n+1} \\ \mathbf{s}_{n+1} &= \mathbf{s}_{n+1}^{\text{tr}} - 2\mu \Delta\gamma_{n+1} \mathbf{N}_{n+1} \\ \psi_{n+1} &= \psi_n + \sqrt{\frac{2}{3}} \Delta\gamma_{n+1}. \end{aligned} \quad (3.44)$$

The algorithm for the complete stress update is summarised in Alg. 2.

```

input :  $\mathbf{e}_{n+1}, \mathbf{e}_n^p, \psi_n$ 
output:  $\mathbf{e}_{n+1}^p, \psi_{n+1}, \mathbf{s}_{n+1}$ 
 $\mathbf{s}_{n+1}^{\text{tr}} = 2\mu(\mathbf{e}_{n+1} - \mathbf{e}_n^p)$ 
%check yield condition
 $f = \|\mathbf{s}_{n+1}^{\text{tr}}\| - \sqrt{2/3}q(\psi_n)$ 
if  $f \leq 0$  then
    |(elastic)
     $\mathbf{e}_{n+1}^p = \mathbf{e}_n^p$ 
     $\mathbf{s}_{n+1} = \mathbf{s}_{n+1}^{\text{tr}}$ 
     $\psi_{n+1} = \psi_n$ 
else
    |(plastic)
     $\mathbf{N}_{n+1} = \mathbf{s}_{n+1}^{\text{tr}} / \|\mathbf{s}_{n+1}^{\text{tr}}\|$ 
    %solve yield condition for plastic multiplier
    call gamma_solve (see Alg. 1)
     $\mathbf{e}_{n+1}^p = [\mathbf{e}_n^p]^1 + \Delta\gamma_{n+1} \mathbf{N}_{n+1}$ 
     $\mathbf{s}_{n+1} = \mathbf{s}_{n+1}^{\text{tr}} - 2\mu \Delta\gamma_{n+1} \mathbf{N}_{n+1}$ 
     $\psi_{n+1} = \psi_n + \sqrt{2/3} \Delta\gamma_{n+1}$ 
end

```

Algorithm 2: Return mapping algorithm for small strains (`return_map`)

3.5.2 Extension to Finite Strains

In order to describe elasto-plasticity in the finite deformation regime, it is convenient to apply a multiplicative split of the deformation gradient as in Eq. (2.15). The deformation gradient is split into an elastic part \mathbf{F}^e and a plastic part \mathbf{F}^p

¹ If the stress update algorithm is extended to finite deformations, the term within brackets $[\mathbf{e}_n^p]$ is neglected.

$$\mathbf{F} = \mathbf{F}^e \mathbf{F}^p . \quad (3.45)$$

With the adoption of Eq. (3.45) - and therefore two additional unknowns - one additional equation is required. The plastic deformation gradient can be determined by using an extension of small strain stress update algorithms to finite deformations as presented in Cuitiño and Ortiz (1992); Montáns and Bathe (2003). In order to extend the stress update algorithm from small strains to finite deformations, the Hencky strain from Eq. (2.32) is used and the elastic trial strain is computed by

$$\boldsymbol{\varepsilon}_{\text{tr}}^e = \frac{1}{2} \ln(\mathbf{C}_{\text{tr}}^e) . \quad (3.46)$$

In Eq. (3.46) \mathbf{C}_{tr}^e represents the trial elastic strain in the finite deformation regime

$$\mathbf{C}_{\text{tr}}^e = (\mathbf{F}_{\text{tr}}^e)^T \mathbf{F}_{\text{tr}}^e , \quad (3.47)$$

and is computed using a trial elastic deformation gradient

$$\mathbf{F}_{\text{tr}}^e = \mathbf{F} (\mathbf{F}_n^p)^{-1} . \quad (3.48)$$

In Eqs. (3.48) and (3.49) the index n denotes the previous time step of the stress update algorithm i.e. the previous Newton iteration. The indices for the current time step $n + 1$ are omitted in Eqs. (3.46) - (3.48) for the sake of clarity. The small strain stress update algorithm provides the plastic small strain increment $\Delta\boldsymbol{\varepsilon}^p$ and the updated hardening variables. The discretisation in time leads to the update rule for the plastic deformation gradient

$$\mathbf{F}_{n+1}^p = \exp(\Delta\boldsymbol{\varepsilon}^p) \mathbf{F}_n^p . \quad (3.49)$$

With this exponential map integrator, the plastic deformation gradient can be recovered from the small plastic strain increment. Equation (3.49) is often referred to as exponential map integrator. The stress that is computed by the stress update algorithm is defined in the plastic configuration and therefore has to be transferred with

$$\boldsymbol{\sigma} = (J^e)^{-1} \mathbf{F}^e \bar{\boldsymbol{\sigma}} (\mathbf{F}^e)^T . \quad (3.50)$$

More details on the extension of small strain stress update algorithms to finite deformation as well as exponential map integrators can be found in Cuitiño and Ortiz (1992); Montáns and Bathe (2003); de Souza Neto et al. (2011). The method is summarised in Alg. 3.

```

input :  $\mathbf{F}_{n+1}, \mathbf{F}_n^p, \psi_n$ 
output:  $\mathbf{F}_{n+1}^p, \psi_{n+1}$ 
%compute trial strain
 $\mathbf{C}_{n+1} = \mathbf{F}_{n+1}^T \mathbf{F}_{n+1}$ 
 $\mathbf{C}_{n+1}^{e, \text{tr}} = (\mathbf{F}_n^p)^{-T} \mathbf{C}_{n+1} (\mathbf{F}_n^p)^{-1}$ 
 $\boldsymbol{\varepsilon}_{n+1}^{\text{tr}} = \frac{1}{2} \ln (\mathbf{C}_{n+1}^{e, \text{tr}})$ 
call return_map (see Alg. 2)
%update plastic deformation gradient
 $\mathbf{F}_{n+1}^p = \exp (\Delta \boldsymbol{\varepsilon}^p) \mathbf{F}_n^p$ 
%push forward of stresses
 $\boldsymbol{\sigma} = (J^e)^{-1} \mathbf{F}^e \bar{\boldsymbol{\sigma}} (\mathbf{F}^e)^T$ 
    
```

Algorithm 3: Extension from small to large strains (`mat_driver`)

3.6 Solution of Nonlinear Problems

Since the resulting system of equations in Eq. (3.26) is nonlinear in the displacements, the problem is linearised as presented in Eq. (3.9). With the linearisation, the nonlinear problem can then be solved iteratively with a Newton method. In order to ensure good convergence of the method, a load parameter λ is introduced to prescribe a load level. The nonlinear system is then given by

$$\underline{\mathbf{g}}(\underline{\mathbf{u}}, \lambda) = \underline{\mathbf{r}}(\underline{\mathbf{u}}) - \lambda \underline{\mathbf{p}} = \underline{\mathbf{0}}. \quad (3.51)$$

The linearised form of Eq. (3.51) is obtained by a Taylor expansion where only the first order term is considered. This results in

$$\underline{\mathbf{g}}(\underline{\mathbf{u}}_n + \Delta \underline{\mathbf{u}}, \bar{\lambda}) = \underline{\mathbf{g}}(\underline{\mathbf{u}}_n, \bar{\lambda}) + \text{D} \underline{\mathbf{g}}(\underline{\mathbf{u}}_n, \bar{\lambda}) \Delta \underline{\mathbf{u}}. \quad (3.52)$$

The requirement $\underline{\mathbf{g}}(\underline{\mathbf{u}}_n + \Delta \underline{\mathbf{u}}, \bar{\lambda}) = \underline{\mathbf{0}}$ leads to the system

$$\text{D} \underline{\mathbf{g}}(\underline{\mathbf{u}}_n, \bar{\lambda}) \Delta \underline{\mathbf{u}} = -(\underline{\mathbf{r}}(\underline{\mathbf{u}}_n, \bar{\lambda}) - \bar{\lambda} \underline{\mathbf{p}}). \quad (3.53)$$

In Eq. (3.53) only the residual \underline{r} and not the loading term \underline{p} is linearised, which is only valid if \underline{p} is independent of the displacements. The linear system in Eq. (3.53) is solved for $\Delta \underline{u}$ in every Newton iteration n and the displacement is updated with $\underline{u}_{n+1} = \underline{u}_n + \Delta \underline{u}$ until $\|\underline{g}(\underline{u}_{n+1}, \bar{\lambda})\| < \text{TOL}$. The convergence of the Newton method is presented in Fig. 3.3 for 1D.

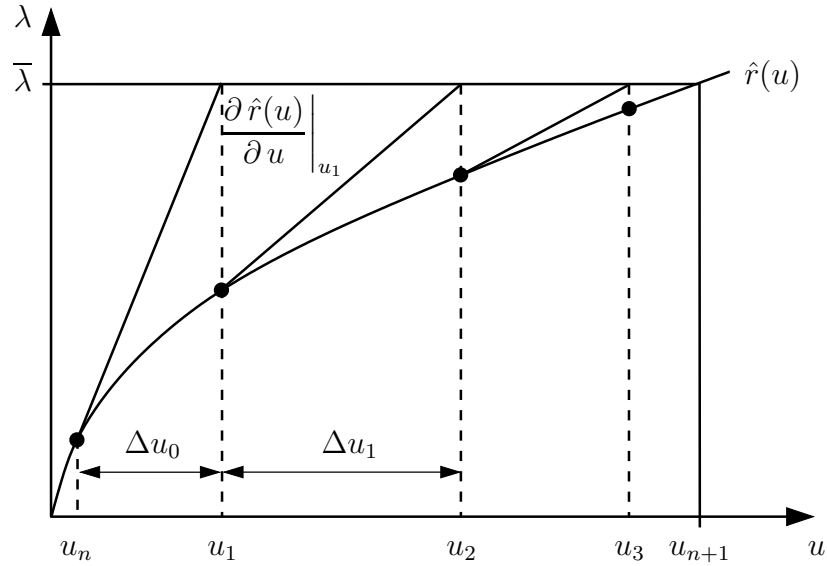


Fig. 3.3: Iterative solving of nonlinear problems

Chapter 4

The Particle Finite Element Method

The simulation of problems with large configurational changes is challenging for established modelling techniques such as the finite element method (FEM), where discrete methods (e.g. molecular dynamics) are customary for this class of problems. For large time- and length scales however, the computation time for discrete methods becomes unreasonable. The particle finite element method (PFEM) was developed in an attempt to combine the benefits of discrete and continuum based methods and was first introduced for simulation of sloshing liquids in Oñate et al. (2004). Due to these assets, the PFEM is a suitable approach to model cutting processes, where the material exhibits large configurational changes especially in the formation of chips and burrs. In this chapter the structure of the PFEM algorithm is introduced, as well as its components. A central part of the method is the detection of boundary segments, which is explained followed by a section on processing of history data. A validation of the PFEM on benchmarks is presented, as well as a physical interpretation of an essential process parameter. The chapter closes with numerical examples that support the outcome of the physical interpretation.

4.1 Structure of the PFEM Algorithm

The PFEM implementation presented in this work consists of several components, which are illustrated in Fig. 4.1. In the context of the PFEM, a body is represented by an ensemble of particles, which are characterised by a particle number and coordinates in two dimensions. The particles carry physical quantities such as the deformation gradient. For elasto-plastic materials the plastic deformation gradient and the hardening variable are stored at the particles as well. To form a domain, the boundary - i.e. the shape of the set of particles - needs to be determined. This process is realised with a so called α -shape algorithm, which is described in detail in Sec. 4.1.1. After identifying

the shape, the domain is meshed with the program TRIANGLE¹. Along with boundary conditions the setup for a finite element calculation is complete, which is solved using the FEM-code FEAP (Finite Element Analysis Program). Displacements are the outcome of the finite element calculation and are used to update the particle coordinates. Furthermore, the deformation gradient is transferred to the particles and preserved for the following PFEM step. For simulations with elasto-plastic material, the plastic deformation gradient and the hardening variable are stored at the particles as well. In the following PFEM step the deformation gradient is recovered using the particle data and the multiplicative decomposition of the deformation gradient from Eq. (2.15). The processing of history data such as the deformation gradient is elaborated in more detail in Sec. 4.1.2.

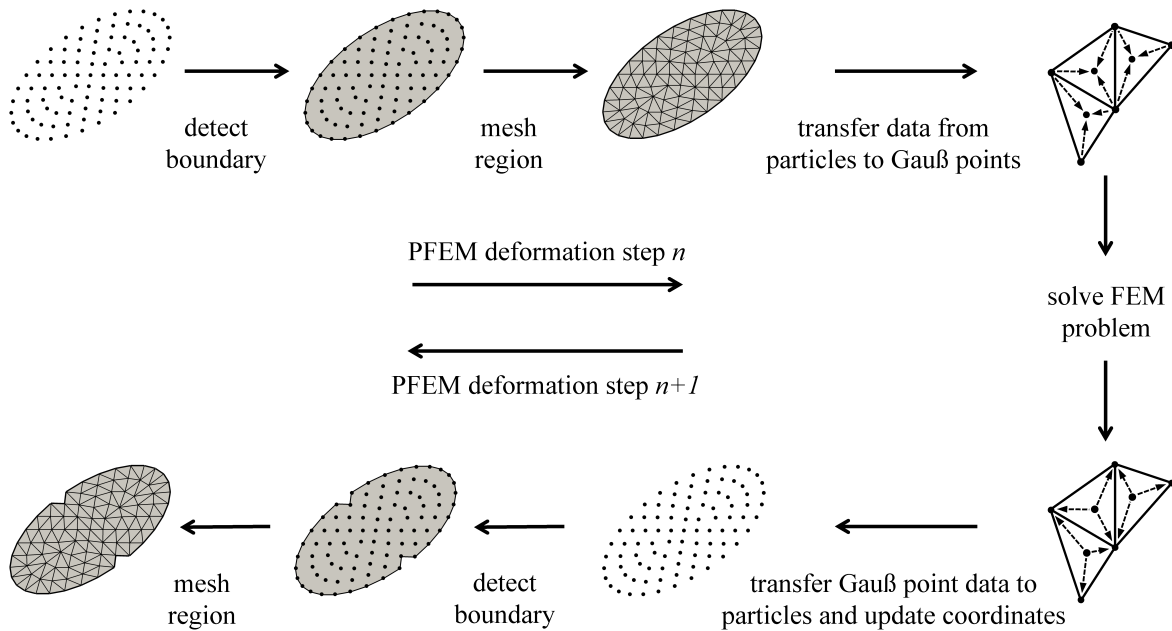


Fig. 4.1: Operations involved in the PFEM

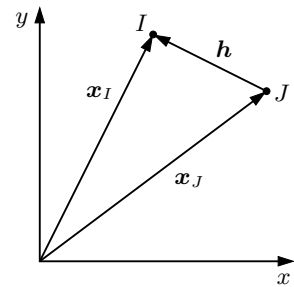
¹For more details see Shewchuk (1996)

4.1.1 Detecting the Shape of a Particle Set

A central aspect in the PFEM is the detection of the *shape*, or more precisely the boundary of a set of particles. There are many possible interpretations of *the shape of a set of points* (see Edelsbrunner and Mücke (1994) and the literature cited in there) and the α -shape method used in this work is one of them. The α -shape method is a generalisation of the convex hull of a set of particles and for more details on the α -shape method, the reader is referred to Edelsbrunner and Mücke (1994); Fischer (2000) and the references cited in there. This section provides a brief description of the algorithm used in this work. Consider a set of particles S with the minimum distance h_{\min} defined by the closest pair of particles of S . The positions of the two particles I and J of the set S are defined by the vectors \mathbf{x}_I and \mathbf{x}_J . Circles b of radius $r = \alpha h_{\min}$ (hence α scales the radius of the circle) are constructed for each pair of particles I and J . If at least one of those circles b is empty (i.e. $b \cap S = \emptyset$), the connecting line between the points I and J is a part of the boundary. In the following the construction of α -circles and the detection of boundary segments is broken down into individual steps.

The first step is to form the vector from particle J to I by subtracting the position vectors

$$\mathbf{h} = \mathbf{x}_I - \mathbf{x}_J. \quad (4.1)$$

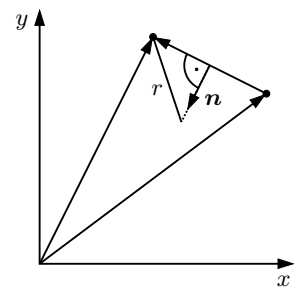


In the following it is tested whether \mathbf{h} is part of the boundary.

Subsequently, an orthogonal vector is constructed to show the direction to the center M of the circle

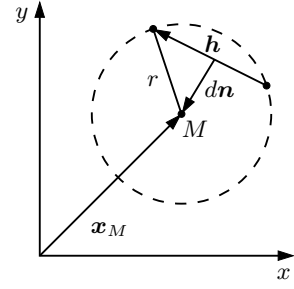
$$\mathbf{n} = \frac{1}{|\mathbf{h}|} \begin{pmatrix} -\mathbf{h} \cdot \mathbf{e}_y \\ \mathbf{h} \cdot \mathbf{e}_x \end{pmatrix}, \quad (4.2)$$

where \mathbf{e}_x and \mathbf{e}_y are the base vectors along x and y .



Since the radius of the circle is compared with the distance to other particles, the position vector to M is of interest. In order to find the center M , the distance d is required. Since the radius is defined as $r = \alpha h_{\min}$ we can get the distance from the center of the circle to the vector \mathbf{h} by

$$d = \sqrt{r^2 - \left(\frac{1}{2}|\mathbf{h}|\right)^2}. \quad (4.3)$$



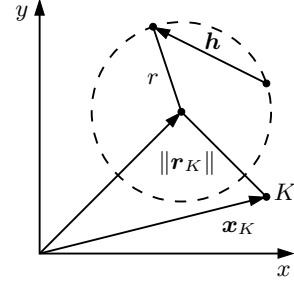
The vector \mathbf{n} can now be scaled by the value d and the center M of the circle is therefore defined as

$$\mathbf{x}_M = \frac{1}{2}(\mathbf{x}_I + \mathbf{x}_J) + d\mathbf{n}. \quad (4.4)$$

In order to confirm that the points I and J are part of the boundary, a check is performed if the circle is empty.

For example the position of point K is defined by the vector \mathbf{x}_K and the distance of this point to the center of the circle can be expressed as

$$|\mathbf{r}_K| = |\mathbf{x}_K - \mathbf{x}_M|. \quad (4.5)$$



If the condition $|\mathbf{r}_K| \geq r$ holds, the point K is not located within the circle and the algorithm continues by checking the next particle. If an intersection of the circle and any particle except I and K can be ruled out, particles I and J form a boundary segment. Algorithm 4 illustrates the implementation of the α -shape algorithm.


```

input :  $r, \mathbf{x}$  %particle coordinates and radius for  $\alpha$ -circles
output:  $s$  %list of boundary segments
for  $i = 1 : num\_particles$  do
  for  $j = 1 : num\_particles$  do
    isempty = TRUE
    for  $k = 1 : num\_particles$  do
       $\mathbf{h} = \mathbf{x}_i - \mathbf{x}_j$ 
       $\mathbf{n} = 1/|\mathbf{h}|(-\mathbf{h} \cdot \mathbf{e}_y \ \mathbf{h} \cdot \mathbf{e}_x)^T$ 
       $d = \sqrt{r^2 - (1/2|\mathbf{h}|)^2}$ 
       $\mathbf{m} = 1/2(\mathbf{x}_i + \mathbf{x}_j) + d\mathbf{n}$ 
       $|\mathbf{r}_k| = |\mathbf{x}_k - \mathbf{m}|$ 
      if  $|\mathbf{r}_k| < r$  then
        isempty = FALSE
      end
    end
    if isempty = TRUE then
      %particles  $x_i$  and  $x_j$  form boundary segment
      %append segment to list  $s$ 
    end
  end
end

```

Algorithm 4: Implementation of the α -shape algorithm

In the following, three different representations of a snowflake are subjected to the α -shape method in order to demonstrate the difficulties, which arise in boundary detection. The three representations are shown in Fig. 4.2.

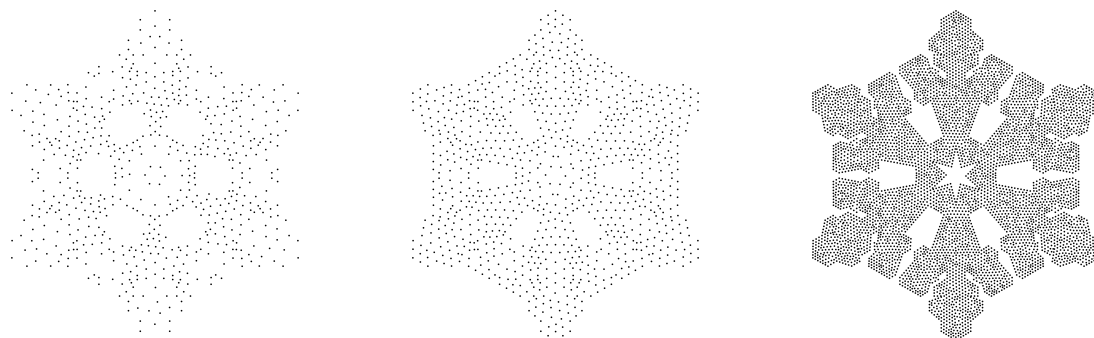


Fig. 4.2: Different particle representations of same shape

The three particle sets in Fig. 4.2 represent a snowflake of the same shape, and differ solely in number of particles and arrangement of particles. The particle density in Fig. 4.2 increases from left to right. In order to study the effect of the parameter α on the detected shape, the three representations from Fig. 4.2 are analysed with the α -shape algorithm and for a varying α . Figure 4.3 shows the results this parameter study, where α increases from right to left and the number of particles increases from top to bottom.

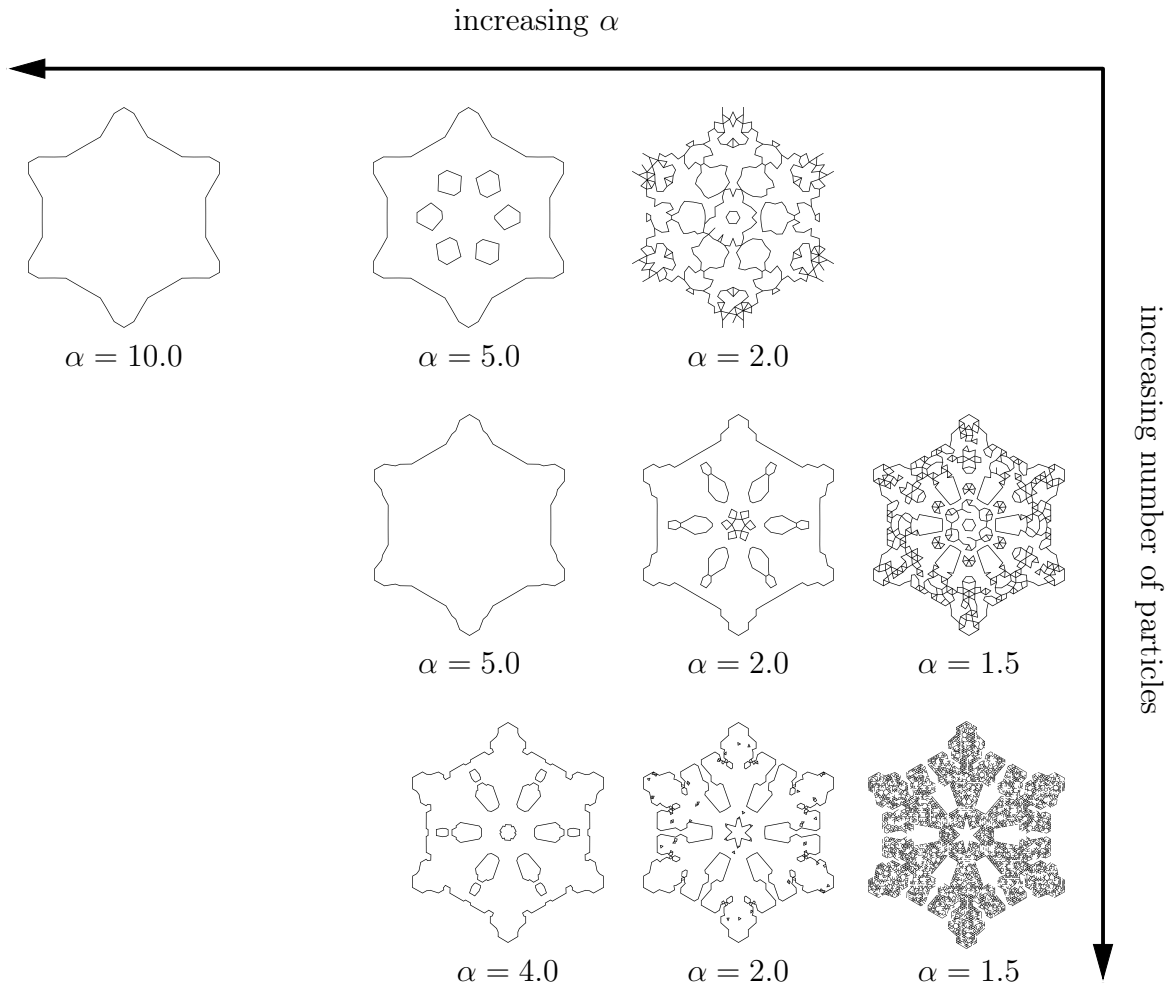


Fig. 4.3: Influence of α on detected shape

In this parameter study each of the three particle sets from Fig. 4.3 is analysed using three different values of α , which produces three different shapes. In Fig. 4.3 it can be observed that the choice of the parameter α greatly influences the detected shape. More precisely, it can be seen that less details are detected if α increases. Another important outcome of this parameter study is that the particle density influences the detected shape as well, since some features of the snowflake can only be resolved if a sufficiently high particle density is considered.

For the choice of the parameter α , the following statements can be formulated:

- If $\alpha = 0.5$ no boundary segments are detected.

- If $\alpha \rightarrow \infty$ the convex hull of the set is detected.

4.1.2 Processing of History Variables

As mentioned in the beginning of this chapter, the deformation gradient \mathbf{F} is stored at the particles, as well as the plastic deformation gradient \mathbf{F}^p , and the hardening variable ψ for simulations with elasto-plastic material. In order to compute nodal values of variables that have been calculated at Gauß points, a procedure can be developed based on the least square method. In the least square method, a functional

$$\kappa = \int_A e^2 dA \quad (4.6)$$

is minimised. In Eq. (4.6) e can be regarded as an error function. If applied to the finite element method, the error function contains Gauß point variables, nodal variables, and the shape functions

$$e(r, s) = t^{\text{GP}}(r, s) - g(r, s), \quad (4.7)$$

with

$$g(r, s) = \sum_{I=1}^N N_I t_I. \quad (4.8)$$

In Eq. (4.7) t^{GP} are the Gauß point variables and in Eq. (4.8) t_I are the unknown nodal variables. Furthermore, N_I are the shape functions of the isoparametric element and N is the number of nodes per element. In order to determine the nodal variables, the functional

$$\kappa = \int_0^1 \int_0^{1-r} [t^{\text{GP}} - \sum_{I=1}^N N_I t_I]^2 \det \mathbf{j}^e ds dr \quad (4.9)$$

is minimised. The variation $\partial\kappa/\partial t_J = 0$ leads to a set of linear equations

$$S_{IJ}^e t_I^e = r_J^e, \quad (4.10)$$

where the right hand side contains the Gauß point variables and the shape functions

$$r_J^e = \int_0^1 \int_0^{1-r} N_J t_J^{\text{GP}} \det \mathbf{j}^e ds dr. \quad (4.11)$$

The matrix

$$S_{IJ}^e = \int_0^1 \int_0^{1-r} N_I N_J \det \mathbf{j}^e \, ds \, dr \quad (4.12)$$

represents the element surface matrix. A global system can now be assembled from the element arrays

$$S_{IJ} t_I = r_J \quad \text{with} \quad r = \bigcup_{e=1}^{n^e} r^e \quad \text{and} \quad S = \bigcup_{e=1}^{n^e} S^e, \quad (4.13)$$

and solved for the unknown nodal values t_I . The matrix S_{IJ} in Eq. (4.13) is a consistent projection matrix and may also be expressed as a lumped matrix in order to speed up the computation of S_{IJ}^{-1} , which is necessary to solve the system in Eq. (4.13). For more details on the method, the reader is referred to Hinton and Campbell (1974); Bathe (2006).

4.2 Validation of the PFEM on Benchmarks

4.2.1 Examples with Uniform Deformations

As described in the introduction of this chapter, the main asset of the PFEM is the repeated boundary detection and remeshing, which enables simulations with large configurational changes. In order to facilitate the remeshing, history data has to be stored at the particles. More specifically, the deformation gradient, the plastic deformation gradient, and the hardening variable have to be transferred from the Gauß points to the particles after every PFEM loading step and vice versa in the beginning of the following step. These operations have been elaborated in the previous section. In the following, the effect of the frequent projection from Gauß points to particles on the quality of the solution is studied. For this purpose, the results of PFEM simulations are compared to results of FEM simulations. The overall load applied in the FEM simulation leads to the deformation Φ as demonstrated in Fig. 4.4.

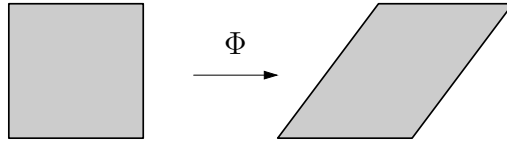


Fig. 4.4: Deformation in FEM simulation

For the PFEM simulations, the load is incremented such that the overall deformation is defined as

$$\Phi = \Phi_3(\Phi_2(\Phi_1)), \quad (4.14)$$

for the example presented in Fig. 4.5.

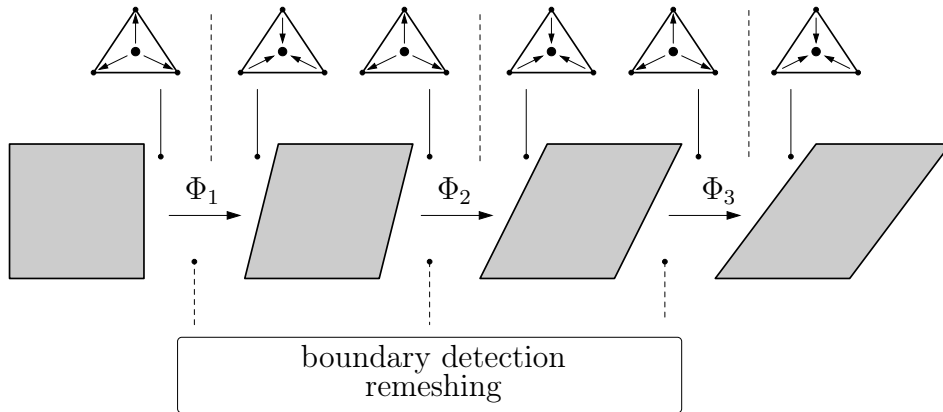


Fig. 4.5: Incremented deformation in PFEM

The deformation in Fig. 4.4 and Fig. 4.5 resembles a simple shear, which is considered as one of the first benchmark simulations to validate the PFEM. The boundary conditions for the simple shear simulation are characterised through a linear decreasing displacement from top to bottom at the left and right boundary. The sides are then tilted by the shear angle γ as described on the right hand side in Fig. 4.6. Another first benchmark with uniform deformation is the uniaxial tensile test as demonstrated on the left hand side in Fig. 4.6. In this simulation the body is vertically fixed at the bottom and a vertical displacement is applied at the top.

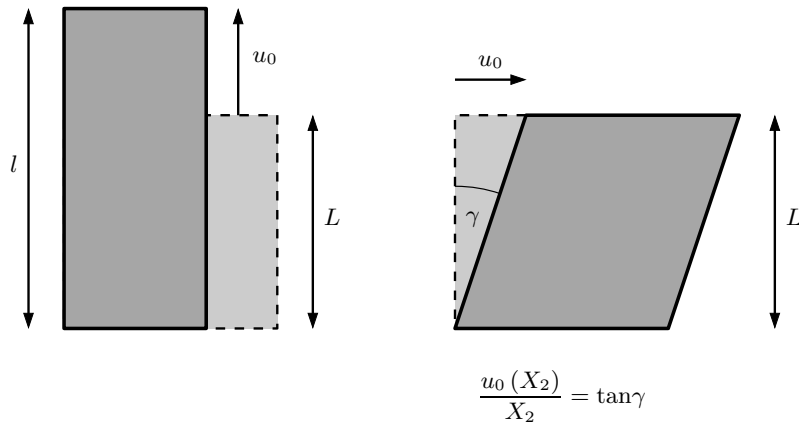


Fig. 4.6: Boundary conditions for benchmark simulations

The FEM and PFEM simulations are carried out using a hyperelastic material in the first comparison and an elasto-plastic material in the second comparison. In the benchmarks reaction forces are compared between FEM and PFEM simulations. For the simulations with hyperelastic material the Lamé constants are chosen to be $\mu = \lambda = 1$, which implies a Poisson ratio of $1/4$. The results of these simulations are shown in Fig. 4.7 for the uniaxial tensile test, and in Fig. 4.8 for the simple shear simulations.

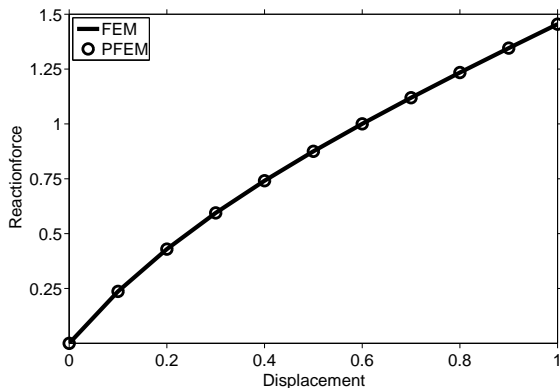


Fig. 4.7: Tensile test simulations with FEM and PFEM

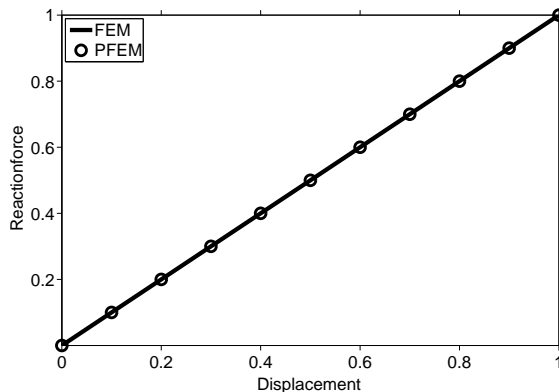


Fig. 4.8: Shear test simulations with FEM and PFEM

As Fig. 4.7 and 4.8 clearly show, the reaction forces produced by the PFEM and the FEM coincide perfectly. In the simulations with hyperelastic material, only the deformation gradient is treated as history data and projected from Gauß points to nodes and vice versa. The following simulations are run with elasto-plastic material, which requires the projection of the deformation gradient, the plastic deformation gradient, and the hardening variable. In these simulations, the Young’s modulus is set to $E = 210000$ MPa, the Poisson ratio $\nu = 0.3$, the initial yield stress $\sigma_y = 300$ MPa and the hardening modulus $k = 2100$ MPa. For the tensile test simulation, the exponent of the hardening power law from Eq. (2.72) is $m = 0.6$. For the shear simulation the exponent is $m = 0$, which resembles perfect plasticity. The material parameters are taken from literature such as Wittel (2009); Böge et al. (2015) to model steel. Figure 4.9 and Fig. 4.10 present the results of the simulations with elasto-plastic material.

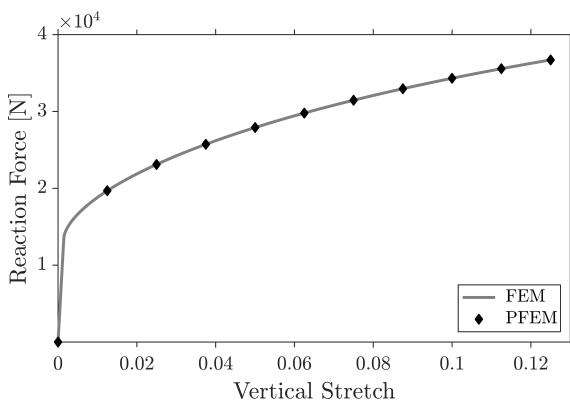


Fig. 4.9: Comparison of reaction force for $m = 0.6$ in uniaxial tension

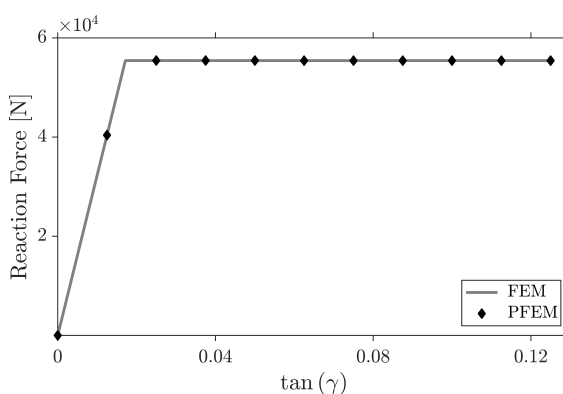


Fig. 4.10: Comparison of reaction force for $m = 0$ in simple shear

Analog to the results for the hyperelastic material, the forces in Figs. 4.9 and 4.10 coincide. From these benchmark tests, it can be concluded that the projection of

history variables exhibits no significant influence on the reaction force in simulations with uniform deformations.

4.2.2 Examples with Non-Uniform Deformations

The boundary conditions in the previous benchmarks only produce uniform deformations. In the following a benchmark with a non-uniform deformation is considered to study the influence of the projection on the reaction force. In Fig. 4.11 the undeformed mesh is shown with the boundary conditions applied in the simulations.

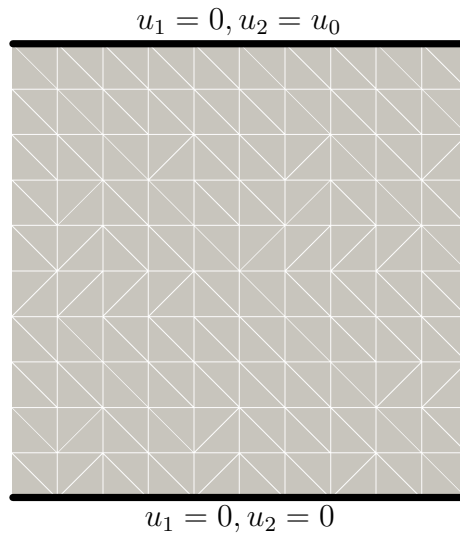


Fig. 4.11: Boundary conditions for comparison with non-uniform deformations

The body is fixed in both degrees of freedom at the base and fixed in horizontal direction at the top, where a displacement boundary condition is applied in vertical direction. In the following a PFEM simulation with 10 loading steps, 20 loading steps, and a FEM simulation are compared on three discretisations with elasto-plastic material. Two contour plots of PFEM simulations with 20 loading steps are presented in Fig. 4.12 and 4.13.

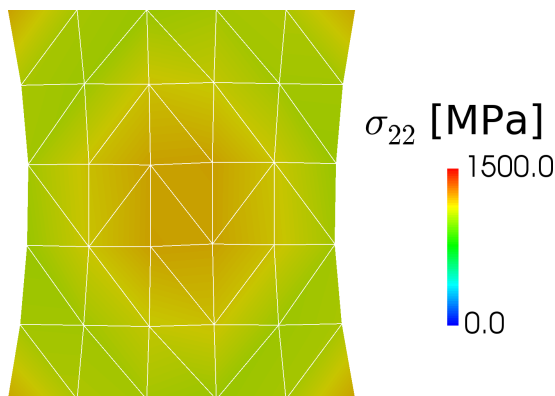


Fig. 4.12: PFEM simulation with 20 loading steps and coarse discretisation

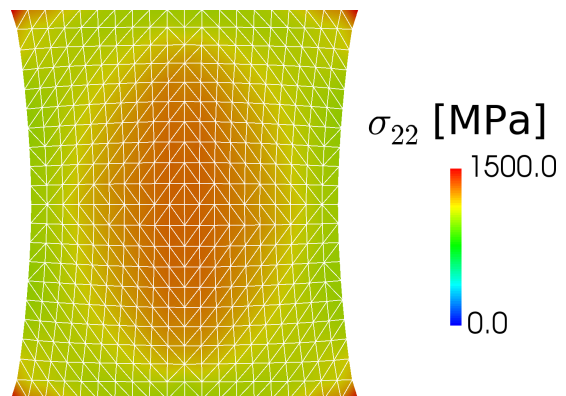


Fig. 4.13: PFEM simulation with 20 loading steps and refined discretisation

In Fig. 4.12 the coarse discretisation used in the comparison between FEM and PFEM is presented and Fig. 4.13 shows the finest discretisation considered. In the following the influence of the number of projections on the reaction force is demonstrated. Figure 4.14 shows the results of the simulations with the coarse discretisation from Fig. 4.12. The solid line represents the reaction force of the FEM simulation, the circles symbolise the results of the PFEM simulation with 10 loading steps, and the diamond shaped markers represent the results of the PFEM simulation with 20 loading steps. Figure 4.15 shows the results of the simulations with the refined mesh.

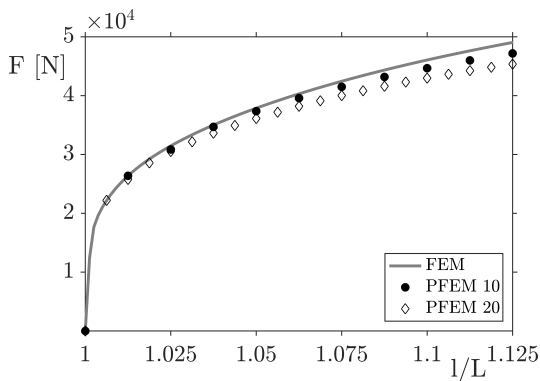


Fig. 4.14: Comparison of the reaction force for coarse discretisation

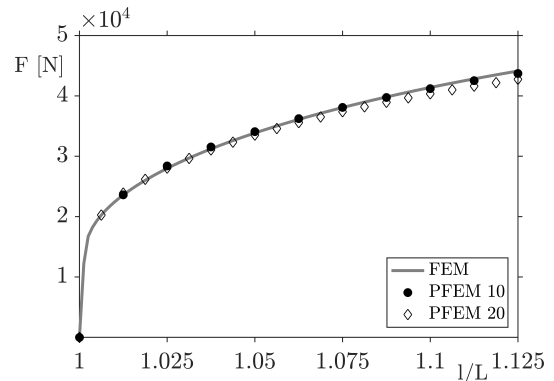


Fig. 4.15: Comparison of the reaction force for refined discretisation

The results with the coarse discretisation in Fig. 4.14 demonstrate that the number of projections in a PFEM simulation influences the reaction force. The reaction force of the PFEM simulation with 20 loading steps is significantly lower than the reaction force of the simulation with 10 loading steps, which is lower than the reaction force of the FEM simulation. This effect can also be observed in Fig. 4.15 with the results of the simulations with the refined discretisation. However, the reaction forces from the FEM simulation, the PFEM simulation with 10 loading steps, and from the PFEM simulation with 20 loading steps converge. In Fig. 4.16 the results of the simulations with the finest discretisation are presented.

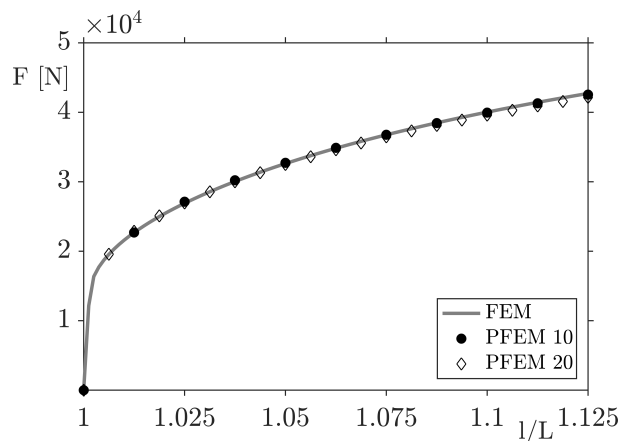


Fig. 4.16: Comparison of the reaction force for finest discretisation

The reaction forces of the simulations with the finest discretisation in Fig. 4.16 agree better than the reaction forces of the simulations with the coarser discretisations in Fig. 4.14 and 4.15. In conclusion, the results of the benchmark tests with non-uniform deformations reveal that the number of PFEM loading steps - and therefore the number of projections of history variables - influences the stress-strain response. An increasing number of PFEM loading steps leads to declining reaction forces. Figures 4.14 - 4.16 also demonstrate that this behaviour can be moderated by refining the discretisation.

4.3 Physical Interpretation of α

In classical textbooks on continuum mechanics such as Holzapfel (2000); Spencer (2004), the definition of strain tensors is motivated through the relative displacement of neighbouring particles. In this concept, the particles are imagined to form line segments which are stretched if the body deforms. With the intention to find a physical interpretation for the parameter α , we will investigate the effect of the α -shape method on the boundary of a continuous body during a deformation. It should be noted at this point that the following considerations are only valid for uniform deformations, and particles in *close neighbourhood*. Nonetheless, the outcome of this investigation is valuable and can provide a better understanding of the role of the α -shape algorithm in PFEM simulations. In Figure 4.17, we consider a body in its reference configuration Ω_0 . The boundary is occupied by set of particles S^b which are distributed in equal distances and therefore form boundary segments of equal length. We assume that the boundary in the undeformed configuration is known and that dL is the length of the boundary segments in the reference configuration. Furthermore, we define the orientation of the boundary segments in configuration Ω_0 by the unit vector e_H . In Fig. 4.17, the undeformed- and the deformed configuration Ω_t are shown as well as the line segment e_H (e_h resp.) and the α -circles.

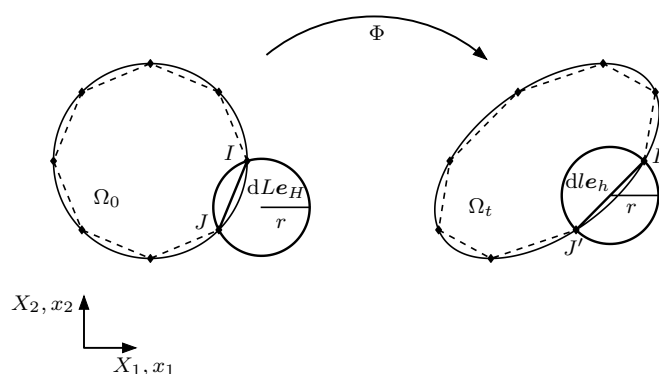


Fig. 4.17: Boundary of body \mathcal{B} in reference- and spatial-configuration

A line segment in the reference configuration is denoted by $dL \mathbf{e}_H$ which points from particle J to particle I . J has the position \mathbf{X}_J and I is therefore located at $\mathbf{X}_I = \mathbf{X}_J + dL \mathbf{e}_H$. A line segment in the deformed configuration $dl \mathbf{e}_h$ is then defined by the particles J' and I' . J' has the position \mathbf{x}_J and I' is located at $\mathbf{x}_I = \mathbf{x}_J + dl \mathbf{e}_h$. The position of particle J' can also be expressed using the deformation Φ as

$$\mathbf{x}_J = \Phi(\mathbf{X}_J), \quad (4.15)$$

and similarly for I'

$$\mathbf{x}_I = \mathbf{x}_J + dl \mathbf{e}_h = \Phi(\mathbf{X}_J + dL \mathbf{e}_H). \quad (4.16)$$

An alternate description of \mathbf{x}_I can be defined by using a Taylor series expansion. Here, only the first order term of the expansion is considered which yields

$$\mathbf{x}_I = \mathbf{x}_J + dl \mathbf{e}_h = \mathbf{x}_J + \frac{\partial \Phi(\mathbf{X}_J)}{\partial \mathbf{X}_J} dL \mathbf{e}_H, \quad (4.17)$$

where $\mathbf{F} = \partial \Phi(\mathbf{X}_J) / \partial \mathbf{X}_J$ represents the deformation gradient. With this notation we can express Eq. (4.17) as

$$dl \mathbf{e}_h = \mathbf{F} dL \mathbf{e}_H. \quad (4.18)$$

This leads to the definition of the stretch ratio

$$\lambda = \frac{dl}{dL} = \mathbf{e}_h^T \mathbf{F} \mathbf{e}_H. \quad (4.19)$$

Squaring Eq. (4.18) on both sides, and rearranging in terms of $\lambda^2 = (dl/dL)^2$ yields the quadratic stretch

$$\lambda^2 = \mathbf{e}_H^T \mathbf{C} \mathbf{e}_H, \quad (4.20)$$

where $\mathbf{C} = \mathbf{F}^T \mathbf{F}$ is the right Cauchy-Green tensor. To demonstrate the effect of the parameter α on the boundary during a deformation, we have to recall the working principle of the α -shape method. As described in Sec. 4.1.1 the method defines a circle for each pair of particles, where the radius is defined as $r = \alpha h_{\min}$. This leads to the conclusion that the distance between the respective pair of particles must not exceed the diameter of the α -circle. In the example presented in Fig. 4.17, the radius of the circle is defined as $r = \alpha dL$, and therefore the length of the deformed line segment has to fulfill the condition

$$dl \leq 2 \alpha dL. \quad (4.21)$$

Inserting Eq. (4.21) into Eq. (4.19) we can define a critical stretch ratio

$$\lambda_c = 2\alpha, \quad (4.22)$$

and recalling the quadratic stretch from Eq. (4.20) the following quadratic form can be defined

$$4\alpha^2 \geq \mathbf{e}_H^T \mathbf{C} \mathbf{e}_H, \quad (4.23)$$

which is studied in the following section for the case of three basic deformations. In three PFEM simulations, a circular disc is subjected to the following scenarios

1. uniaxial stretch,
2. biaxial stretch,
3. simple shear.

1. An example with uniaxial stretch is characterised by the deformation gradient

$$\mathbf{F} = \begin{bmatrix} 1 & 0 \\ 0 & m \end{bmatrix}. \quad (4.24)$$

By expressing the deformation gradient in Eq. (4.24) with the displacement gradient from Eq. (2.4), boundary conditions for the uniaxial stretch can be formulated with

$$m = \frac{du_2}{dX_2} + 1. \quad (4.25)$$

Therefore, the displacement boundary condition yields

$$u_2(X_2) = (m - 1)X_2. \quad (4.26)$$

In Fig. 4.18 the circular disc is presented as well as the boundary conditions that produce a uniaxial stretch in the body.

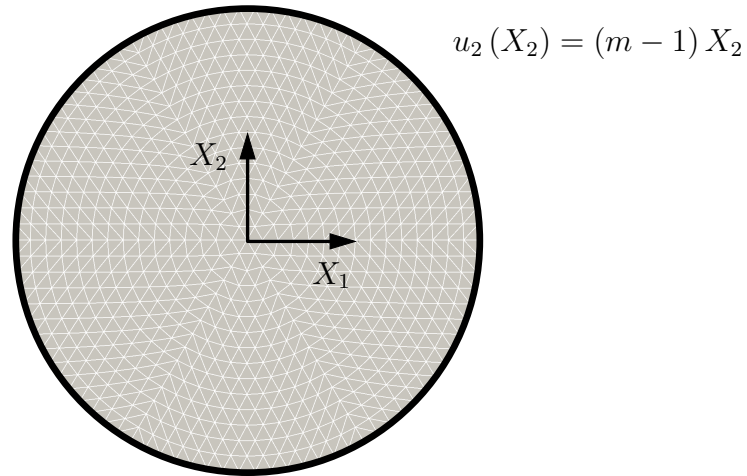


Fig. 4.18: Boundary conditions for uniaxial stretch

In the PFEM simulation with the boundary condition of Eq. (4.26) the parameter α is set to $\alpha = 0.8$. In Fig. 4.19 the circular disc is shown immediately before reaching the critical deformation, and in Fig. 4.20 the separated disc is shown.

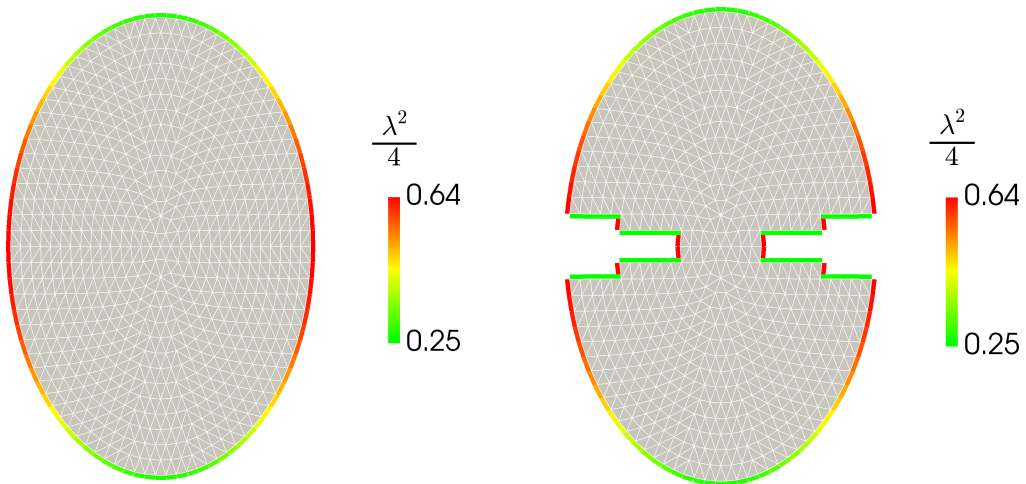


Fig. 4.19: Quadratic stretch of boundary segments for tension

Fig. 4.20: Failure of boundary segments after reaching $\lambda^2/4 = \alpha^2$

The colour code in Fig. 4.19 and 4.20 highlights the quadratic stretch $\lambda^2/4$, where the green colour represents unstretched boundary segments, and the red colour indicates the maximum stretch $\lambda^2/4 = \alpha^2$. In the figures it can be seen that the boundary segments separate after reaching the critical stretch.

In order to present a relation between α and the eigenvalues of the right Cauchy-Green tensor, we rearrange Eq. (4.20) to

$$\mathbf{e}_H^T (\mathbf{C} - \lambda^2 \mathbf{1}) \mathbf{e}_H = 0. \quad (4.27)$$

The unit vector of the undeformed line segment \mathbf{e}_H in Eq. (4.27) is compared to the eigenvectors, and λ^2 to the eigenvalues of \mathbf{C} . Therefore the classical eigenvalue problem

$$(\mathbf{C} - \gamma_i^2 \mathbf{1}) \mathbf{v}_i = \mathbf{0} \quad (4.28)$$

is considered, where γ_i^2 and \mathbf{v}_i resemble the eigenvalues and eigenvectors of the right Cauchy-Green tensor. To simplify Eq. (4.27), the transformation matrix

$$\mathbf{Q} = [\mathbf{v}_1 \quad \mathbf{v}_2] \quad (4.29)$$

is introduced, which contains the eigenvectors of \mathbf{C} . Due to the nature of the eigenvectors $\mathbf{v}_1 \perp \mathbf{v}_2$, the matrix \mathbf{Q} is orthogonal (i.e. $\mathbf{Q}^T \mathbf{Q} = \mathbf{1}$), and is used in this scenario to rotate the basis vectors \mathbf{e}_i into the eigenvectors \mathbf{v}_i and vice versa by

$$\mathbf{e}_i = \mathbf{Q} \mathbf{v}_i, \quad \mathbf{v}_i = \mathbf{Q}^T \mathbf{e}_i. \quad (4.30)$$

Applying the transformation matrix to the unit vector of the unstretched line segment yields $\mathbf{e}_H = \mathbf{Q} \mathbf{e}'_H$. With this expression, Eq. (4.27) is rearranged to

$$\lambda^2 = (\mathbf{Q} \mathbf{e}'_H)^T \mathbf{C} \mathbf{Q} \mathbf{e}'_H = \mathbf{e}'_H{}^T \mathbf{C}' \mathbf{e}'_H, \quad (4.31)$$

where the tensor \mathbf{C}' represents the diagonalised right Cauchy-Green tensor

$$\mathbf{C}' = \mathbf{Q}^T \mathbf{C} \mathbf{Q} = \begin{bmatrix} \gamma_1^2 & 0 \\ 0 & \gamma_2^2 \end{bmatrix}. \quad (4.32)$$

The transformations used in the expressions above are illustrated in Fig. 4.21.

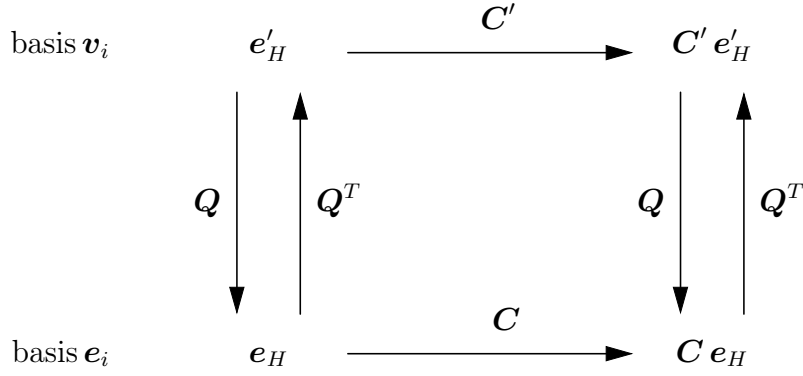


Fig. 4.21: Rotation of line segments and the right Cauchy-Green tensor

With the following definitions for the rotated unit vector of the line segment

$$e'_H = \begin{pmatrix} e'_{H1} \\ e'_{H2} \end{pmatrix} \quad \text{and} \quad e'_{H1} + e'_{H2} = 1, \quad (4.33)$$

and considering the structure of C' in Eq. (4.32) we can expand Eq. (4.31) to

$$\lambda^2 = \gamma_1^2 e'^2_{H1} + \gamma_2^2 e'^2_{H2} = \gamma_1^2 - (\gamma_1^2 - \gamma_2^2) e'^2_{H2}. \quad (4.34)$$

By regarding Eq. (4.34) one can observe that the following two scenarios are conceivable:

- The first and second eigenvalues are equal $\gamma_1^2 = \gamma_2^2$. Then $\lambda^2 = \gamma_1^2 = \gamma_2^2$ follows and a critical stretch is reached if $\gamma_i^2 = \lambda^2 = 4\alpha^2$. In Eq. (4.34) can be observed that in this case the orientation of the rotated line segment is arbitrary.
- In the event that $\gamma_i^2 > \gamma_j^2$ (without loss of generality $\gamma_1^2 > \gamma_2^2$) it follows that

$$\lambda^2 = \gamma_1^2 - \underbrace{(\gamma_1^2 - \gamma_2^2)}_{>0} \underbrace{e'^2_{H2}}_{\geq 0} \leq \gamma_1^2, \quad (4.35)$$

which yields a maximum allowed stretch of the line segment

$$\lambda^2_{\max} = \gamma_1^2 \quad \text{for} \quad e'_H = \begin{pmatrix} e'_{H1} \\ e'_{H2} \end{pmatrix} \quad (4.36)$$

with respect to basis v_i . In this case, the unit vector of the undeformed line segment is collinear to the respective eigenvector

$$\mathbf{e}_H = \mathbf{Q} \mathbf{e}'_H = \mathbf{v}_1 \quad (4.37)$$

with respect to basis \mathbf{e}_i . From this result can be concluded that the quadratic stretch of the line segment λ^2 gets maximal (w.r.t. direction \mathbf{e}_H) for the principal direction \mathbf{v}_1 with the maximal eigenvalue γ_1^2 i.e.

$$\lambda_{\max}^2 = \mathbf{v}_1^T \mathbf{C} \mathbf{v}_1 = \gamma_1^2. \quad (4.38)$$

The quadratic stretch of a boundary segment - perfectly aligned with direction \mathbf{v}_1 - becomes critical, if $\gamma_1^2 = \lambda_{\max}^2 = 4\alpha^2$.

Figures 4.22 and 4.23 show the undeformed and deformed mesh of a PFEM simulation with boundary conditions according to Fig. 4.18, and $\alpha = 0.8$. Figure 4.22 demonstrates the orientation of the eigenvector corresponding to λ_1^2 .

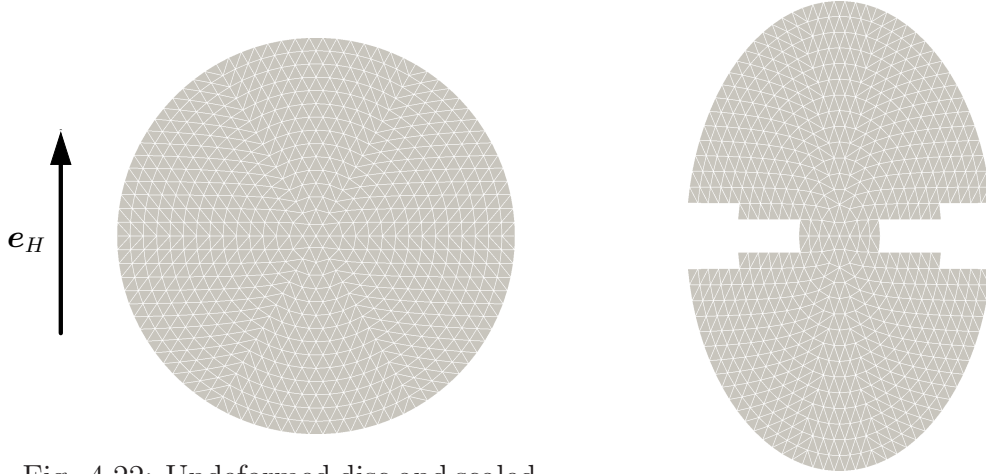


Fig. 4.22: Undeformed disc and scaled eigenvector corresponding to λ_1^2

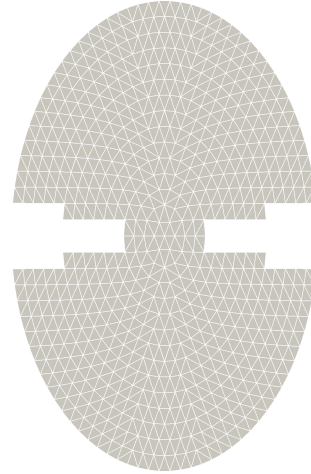


Fig. 4.23: Deformed disc with failed boundary segment

2. In the next example, a deformation which resembles a biaxial stretch is studied. In this case, the deformation gradient yields

$$\mathbf{F} = \begin{bmatrix} m & 0 \\ 0 & n \end{bmatrix}, \quad (4.39)$$

where we set $n = \frac{3}{4}m$. By expressing the deformation gradient in Eq. (4.39) with the displacement gradient from Eq. (2.4), boundary conditions for a biaxial stretch can be formulated with

$$m = \frac{du_1}{dX_1} + 1 \quad \text{and} \quad \frac{3}{4}m = \frac{du_2}{dX_2} + 1. \quad (4.40)$$

The displacement boundary conditions can then be expressed as

$$u_1(X_1) = (m - 1) X_1 \quad \text{and} \quad u_2(X_2) = (3/4 m - 1) X_2. \quad (4.41)$$

In Fig. 4.24 the circular disc is presented as well as the boundary conditions to enforce a biaxial stretch.

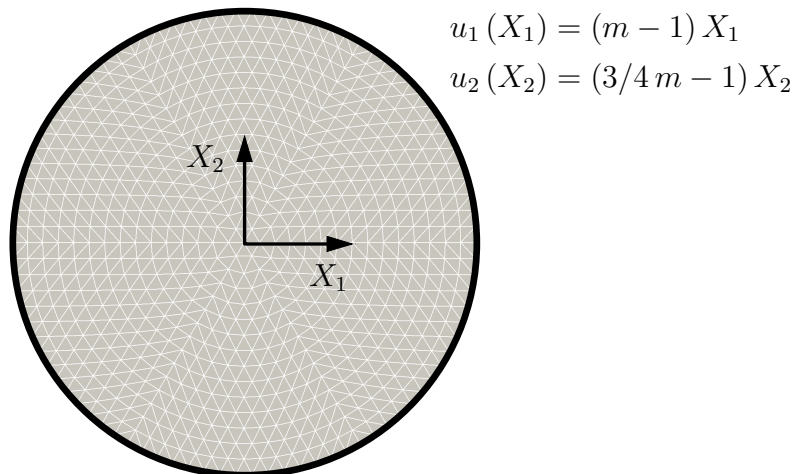


Fig. 4.24: Boundary conditions for biaxial stretch

In the PFEM simulation with the boundary conditions of Eq. (4.41) the parameter α is set to $\alpha = 0.8$. In Fig. 4.25 the circular disc is shown immediately before reaching the critical deformation, and in Fig. 4.26 the separated disc is presented.

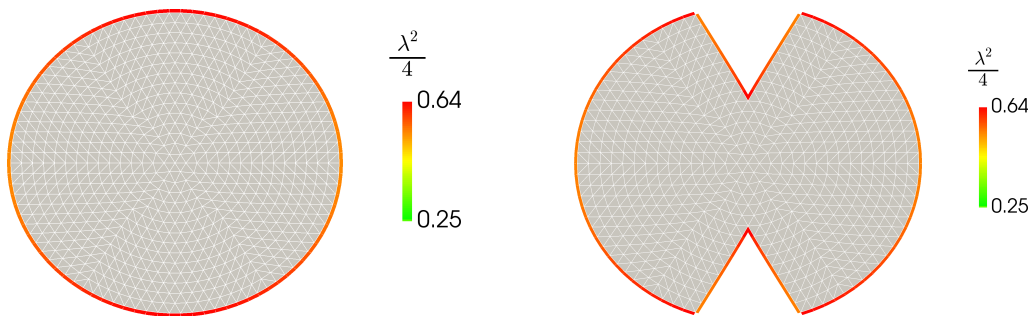


Fig. 4.25: Quadratic stretch of boundary segments for biaxial stretch

Fig. 4.26: Failure of boundary segments after reaching $\lambda^2/4 = \alpha^2$

The colour code in Fig. 4.25 and 4.26 highlights the quadratic stretch $\lambda^2/4$, where the red colour indicates the maximum stretch $\lambda^2/4 = \alpha^2$. In the figures it can be seen that the boundary segments separate after reaching the critical stretch. Analog to the example with uniaxial stretch, a maximum parameter m for the deformation gradient in Eq. (4.39) can be calculated. Since $\alpha = 0.8$ as in the previous example, the maximum stretch is $m = 8/5$ and $n = 3/4$.

For this deformation the largest principal stretch is $\lambda_1^2 = 2.56$ and therefore fulfills the α -shape condition $\lambda^2 \leq 4\alpha^2$. With the eigenvalue we can calculate the corresponding eigenvector. Figure 4.27 and 4.28 show the undeformed and deformed mesh of the PFEM simulation with boundary conditions according to Fig. 4.24, and $\alpha = 0.8$. Figure. 4.27 demonstrates the orientation of the eigenvector corresponding to λ_1^2 .

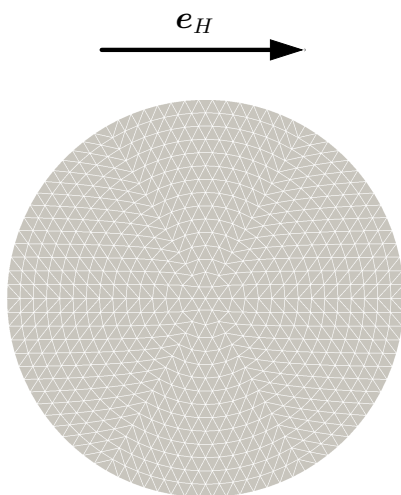


Fig. 4.27: Undeformed disc and scaled eigenvector corresponding to λ_1^2

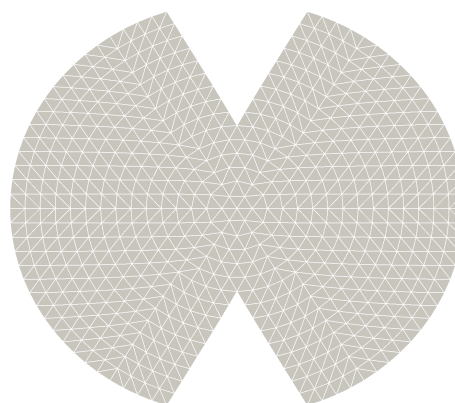


Fig. 4.28: Deformed disc with failed boundary segment

3. The last example is concerned with a simple shear deformation, which is characterised by the deformation gradient

$$\mathbf{F} = \begin{bmatrix} 1 & m \\ 0 & 1 \end{bmatrix}. \quad (4.42)$$

Analog to the previous examples, the deformation gradient is expressed with the displacement gradient, which yields

$$m = \frac{du_1}{dX_2}. \quad (4.43)$$

The boundary condition then follows as

$$u_1(X_2) = m X_2. \quad (4.44)$$

In Fig. 4.29 the disc is presented and the boundary conditions indicated.

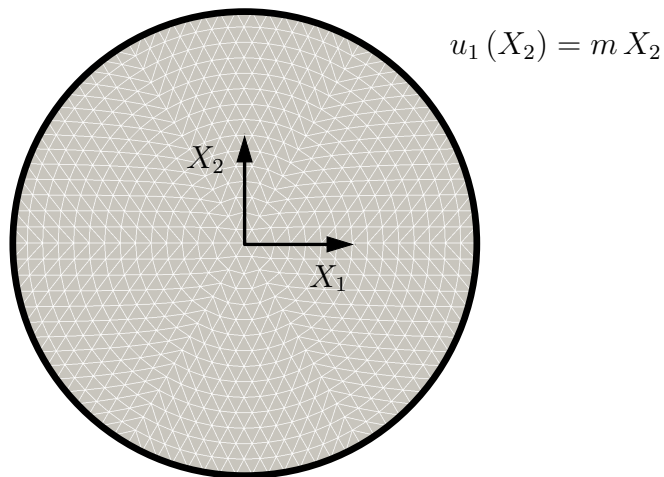


Fig. 4.29: Boundary conditions for simple shear

In the PFEM simulation with boundary conditions according to Eq. (4.44) the parameter α is set to $\alpha = 0.75$. The contour plots in Fig. 4.30 and 4.31 show the disc under simple shear before, and after reaching the critical stretch of the boundary segments.

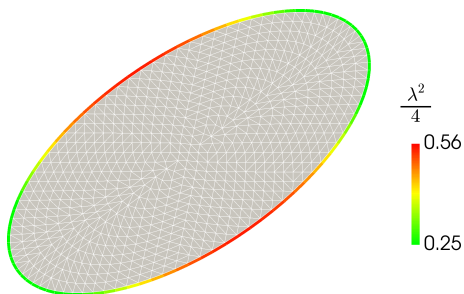


Fig. 4.30: Quadratic stretch of boundary segments for simple shear

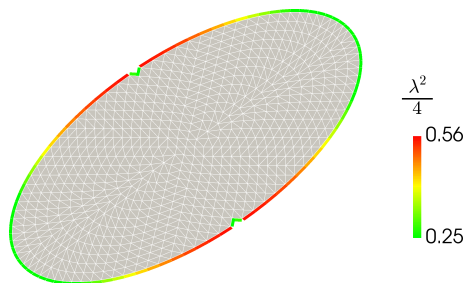


Fig. 4.31: Failure of boundary segments after reaching $\lambda^2/4 = \alpha^2$

Analog to the previous examples, a maximum shear m for the deformation gradient in Eq. (4.42) can be determined. Since $\alpha = 0.75$, the maximum shear yields $m = 5/6$. For this deformation the largest principal stretch is $\lambda_1^2 = 2.25$, which satisfies the α -shape condition $\lambda^2 \leq 4 \alpha^2$. Figures 4.33 and 4.32 show the deformed and undeformed mesh of a PFEM simulation with simple shear and $\alpha = 0.75$. Figure 4.32 demonstrates the orientation of the eigenvector corresponding to λ_1^2 .

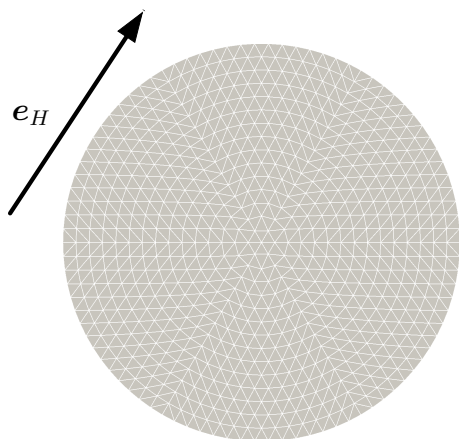


Fig. 4.32: Deformed disc with failed boundary segment

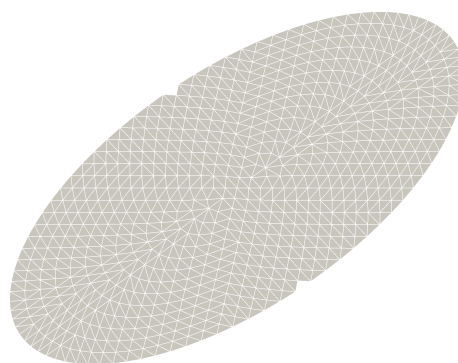


Fig. 4.33: Undeformed disc and scaled eigenvector corresponding to λ_1^2

In Fig. 4.33 the deformed mesh of the PFEM simulation is shown after the first boundary segment has exceeded the critical stretch. Figure 4.32 shows the undeformed disc and the scaled eigenvector of the largest principal stretch.

The PFEM simulations of the three basic deformations demonstrate that the material separates where $\lambda_1^2 > 4\alpha^2$, and where the corresponding eigenvector is collinear to the boundary. In the following the three examples are considered again, only now the vectors that describe the boundary segments in the unreformed configuration \mathbf{H} , and in the deformed configuration \mathbf{h} are not considered to be unit vectors. The aim of this further investigation is to provide a graphical representation of the restriction on boundary segments by the parameter α .

1. For the uniaxial stretch with the deformation gradient of Eq. (4.24), the quadratic form of Eq. (4.23) is visualised in Fig. 4.34. The grey surface resembles the quadratic stretch and the black surface symbolises the restriction due to α . Figure 4.34 is plotted with $\alpha = 0.8$ and the consequential maximum deformation for the uniaxial stretch $m = 8/5$.

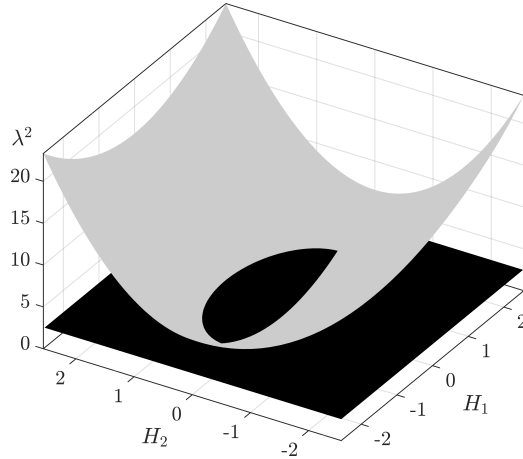


Fig. 4.34: Restriction of quadratic stretch for uniaxial stretch

The quadratic stretch in Fig. 4.34 is limited by the condition $\lambda^2 \leq 4r^2$, meaning that only the quadratic stretch underneath the black surface is feasible. Initially in the α -shape algorithm, the condition $|\mathbf{H}| \leq 2r$ is examined for the reference configuration. The radius r is set to $r = \alpha|\mathbf{H}|$ and represents the shortest distance between any pair of particles in the undeformed configuration. We define $|\mathbf{H}|$ to be equal for all boundary segments. If the above-mentioned condition holds, and no other particle is located in the α -circle, \mathbf{H} is considered as a boundary segment. Due to the deformation, the segments \mathbf{H} transform into the segments \mathbf{h} of length $|\mathbf{h}|$, which in general are not of equal length. In the actual configuration, the α -shape method examines if the condition $|\mathbf{h}| \leq 2L\alpha$ holds, which means that the length of the deformed segment has to be less or equal than the diameter of the α -circle. Since $\mathbf{h} = \mathbf{F}\mathbf{H}$, the condition $\mathbf{H}^T \mathbf{F}^T \mathbf{F} \mathbf{H} \leq 4r^2$ has to be fulfilled in order that the deformed line segment \mathbf{h} is still a boundary segment. The above mentioned conditions for the reference and the actual configuration are shown in the H_1 - H_2 plane in Fig. 4.35.

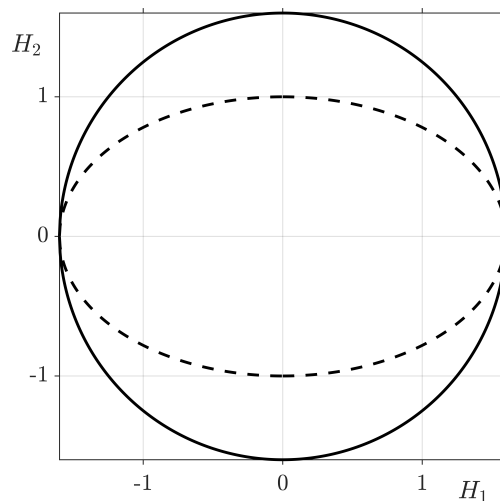


Fig. 4.35: Restriction on choice of boundary segments

The solid line in Figure 4.35 represents the set of all potential boundary segments \mathbf{H} for the reference configuration, where the dashed line presents a restriction on the boundary segments due to the deformation. The dashed line in Fig. 4.35 represent the maximum stretch for a uniaxial deformation with $\alpha = 0.8$ and $m = 8/5$ respectively.

2. In agreement with the previous example, the biaxial stretch with the deformation gradient of Eq. (4.39) is considered. The quadratic form of Eq. (4.23) is visualised in Fig. 4.34, where the grey surface resembles the quadratic stretch, and the black surface symbolises the restriction due to α .

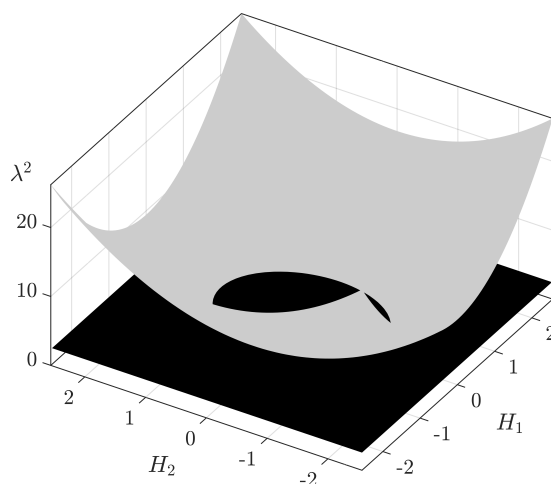


Fig. 4.36: Restriction of quadratic stretch for biaxial stretch

In Fig. 4.37 the restriction on boundary segments is illustrated in the H_1 - H_2 plane for $\alpha = 0.8$, $m = 8/5$, and $n = 6/5$.

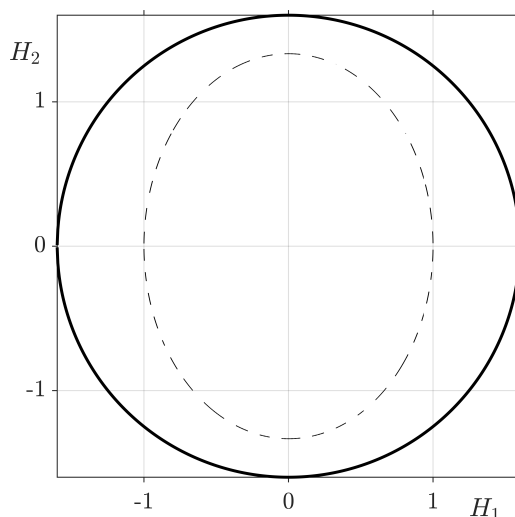


Fig. 4.37: Restriction on choice of boundary segments

As in the previous example, the solid line represents the set of all potential boundary segments for the reference configuration, and the dashed line symbolises the restriction on the boundary segments in the reference configuration due to the deformation.

3. Finally, simple shear is considered with the deformation gradient of Eq. (4.42). The quadratic form of Eq. (4.23) is illustrated in Fig. 4.34. The grey surface in Fig. 4.34 represents the quadratic stretch, and the black surface symbolises the restriction due to α .

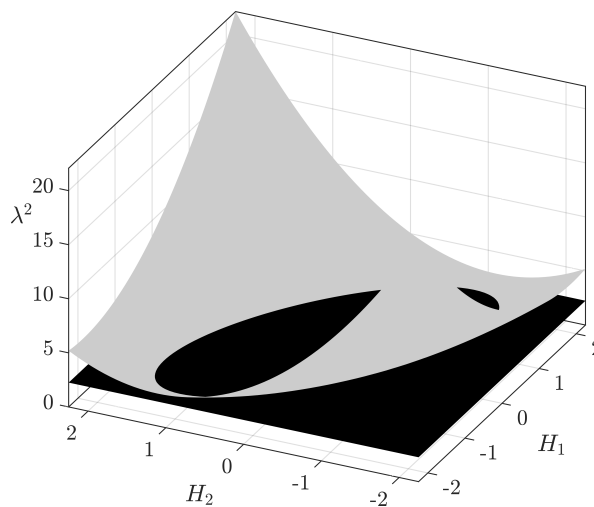


Fig. 4.38: Restriction of quadratic stretch for simple shear

The plots in Fig. 4.38 and 4.39 are generated with $\alpha = 0.75$ and the maximum shear deformation $m = 5/6$ in Eq. (4.42). In Fig. 4.39 the restriction on boundary segments is illustrated in the H_1 - H_2 plane.

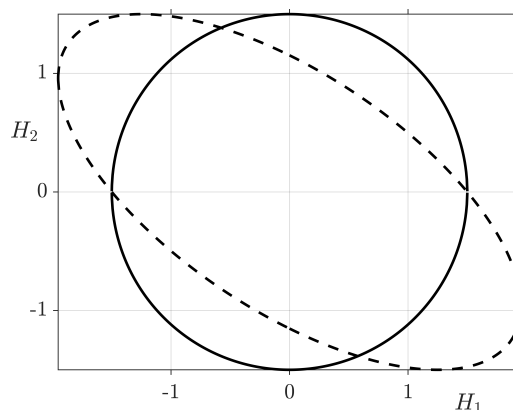


Fig. 4.39: Restriction on choice of boundary segments

As in the previous two examples, the solid line symbolises the set of all potential boundary segments \mathbf{H} in the reference configuration. After the line segments are

deformed, the α -shape algorithm detects the boundary again. The dashed line in Fig. 4.39 represents the restriction on the boundary segments in the undeformed configuration.

4.3.1 The Role of α in Tensile Tests

Section 4.3 illustrates that α can be regarded as the maximum stretch of a boundary segment. If the critical stretch $\lambda = 2\alpha$ is exceeded, the material separates. In order to demonstrate the meaning of α on an engineering based example, a tensile test is simulated. Figure 4.40 shows the undeformed specimen and the boundary conditions.

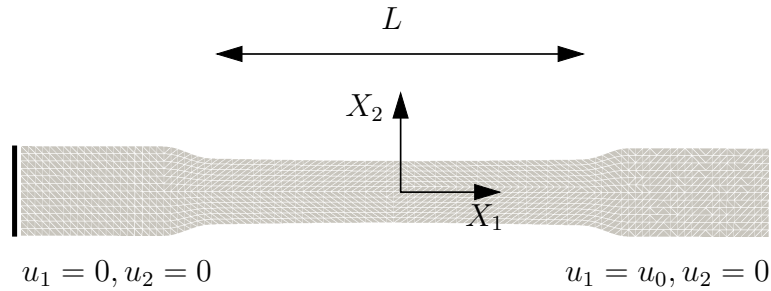


Fig. 4.40: Specimen for tensile test and boundary conditions

In Fig. 4.40 L represents the reference length and in Fig. 4.41 l denotes the deformed length. The undeformed overall length of the specimen is 160 mm. At the left side the sample is clamped in both directions i.e. $u_1 = 0, u_2 = 0$, and a displacement is applied at the right side in X_1 direction $u_1 = u_0$. The displacements in X_2 direction at the right side are set to $u_2 = 0$. In order to investigate the influence of α on the material response the reaction force is plotted with respect to the stretch of the mid section l/L . In all simulations, the Young's modulus is set to $E = 210000$ MPa, the Poisson's ratio $\nu = 0.3$, the hardening modulus $k = 1600$ MPa, the initial yield stress $\sigma_y = 300$ MPa, and the exponent of the hardening power law from Eq. (2.72) $m = 0.8$. The material parameters are taken from literature such as Wittel (2009); Böge et al. (2015) to model steel. Figure 4.41 shows the stress distribution in the deformed sample.

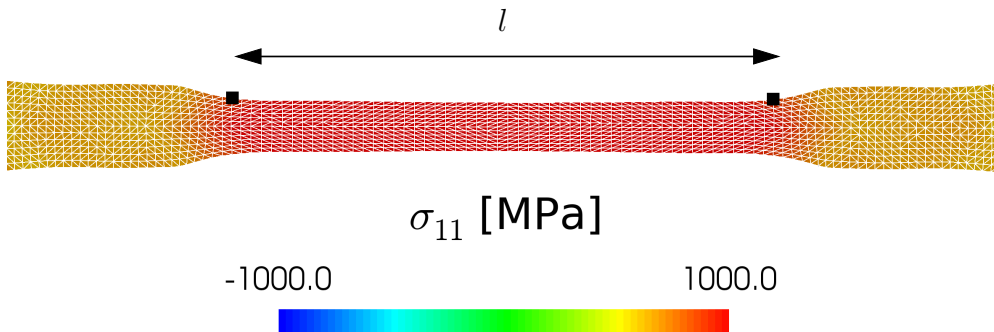


Fig. 4.41: Contour plot of stresses on deformed specimen

As can be seen in Fig. 4.41, high tensile stresses develop in the mid section of the specimen as the load increases up to the point, where the material starts to separate. In Fig. 4.42 the reaction forces are plotted with regard to the stretch of the mid section for three simulations with a varying α .

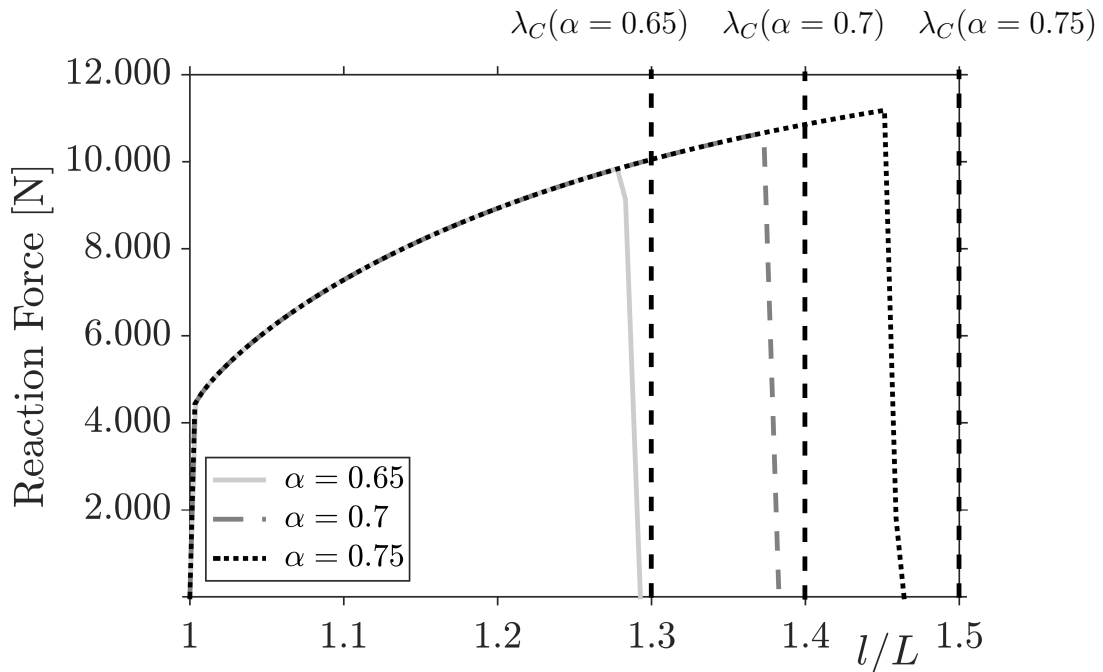


Fig. 4.42: Comparison of reaction force for uniaxial tension

Figure 4.42 demonstrates the properties of the elasto-plastic material model. In the beginning, the reaction forces increase linearly in all simulations until the yield criterion is met, then the response shows a nonlinear plastic hardening. From Sec. 4.3 it follows that the material is expected to separate, if the stretch of the boundary segments exceeds the critical value $\lambda = 2\alpha$. However, the specimen from Fig. 4.40 fails not precisely at the predicted stretch. Therefore, a follow up study is conducted, where a body under perfect uniaxial stretch is considered as shown in Fig. 4.43.

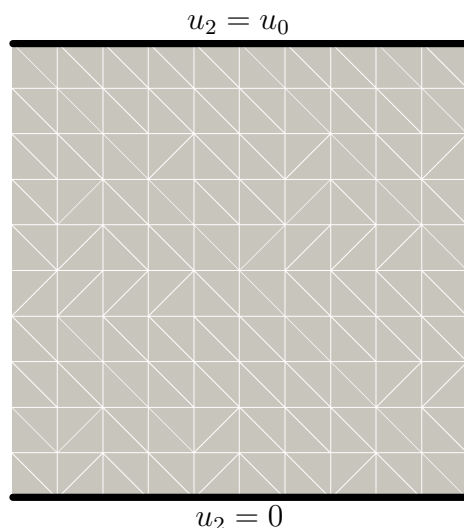


Fig. 4.43: Boundary conditions for comparison with non-uniform deformations (lateral contraction is free to ensure traction $\mathbf{t} = \mathbf{0}$ on left and right boundary)

The body in Fig. 4.43 is of size 40 mm x 40 mm, and the material parameters are identical to those of the previous example. From the derivation of the maximum stretch criterion in Sec. 4.3 follows that it is independent of the discretisation. To emphasise this effect, this tensile test is carried out using two discretisations. In Fig. 4.44 the results of the simulations with $\alpha = 0.65$ are illustrated for both discretisations and Fig. 4.45 shows the results for the simulations with $\alpha = 0.7$.

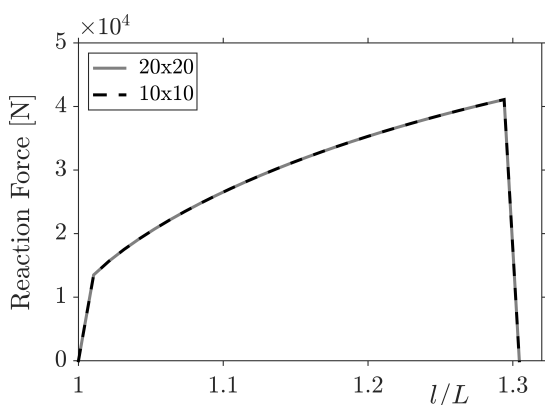


Fig. 4.44: Uniaxial tension with $\alpha = 0.65$

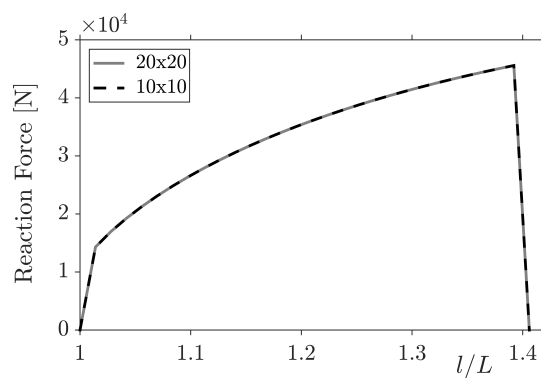


Fig. 4.45: Uniaxial tension with $\alpha = 0.7$

In Fig. 4.44 and 4.45 the results are shown from simulations with 20x20 boundary segments and for 10x10 boundary segments and it can be observed that the number of boundary segments - and therefore the initial length of the segments - does not influence material separation. The specimen from Fig. 4.43 separates exactly at the predicted point $\lambda = 2\alpha$, which can be observed in Fig. 4.44 for $l/L = 1.3$, and in

Fig. 4.45 for $l/L = 1.4$. In Fig. 4.46 the results of the simulations with $\alpha = 0.75$ are presented.

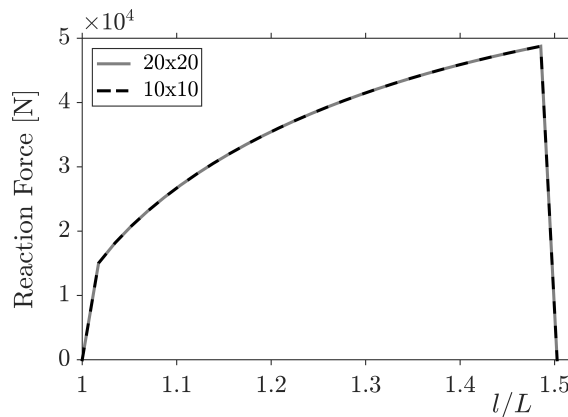


Fig. 4.46: Uniaxial tension with $\alpha = 0.75$

Analog to the results in Fig. 4.44 and 4.45, the simulation with $\alpha = 0.75$ in Fig. 4.46 shows coinciding results for both discretisations and the material separates at the predicted stretch. The maximum strain a material can endure is often referred to as fracture strain (see Gross and Seelig (2016); Böge et al. (2015)).

4.3.2 Modelling of Material Separation

As demonstrated in the previous section, the parameter α can be related to the fracture strain in tensile tests. As a conclusion, material separation can be modelled using α , and brittle, as well as tough material behaviour can be mimicked. In the following, a plate is studied under boundary conditions as shown in Fig. 4.47.

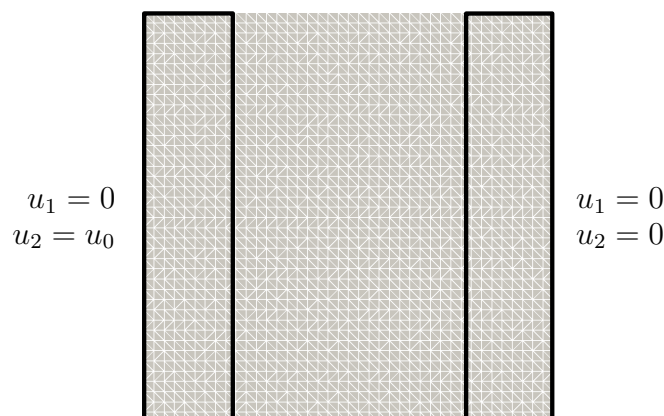


Fig. 4.47: Benchmark for material separation

The plate in Fig. 4.47 is clamped on the right side and a vertical displacement is applied on the left boundary. In all simulations a hyperelastic material is used and the Lamé constants are set to $\mu = 925$ MPa and $\lambda = 2160$ MPa, which is characteristic for plastics (see Hellerich et al. (2004)). In Fig. 4.48 the results of simulations for three different values of α are shown. The left column in Fig. 4.48 shows the results of simulations with $\alpha = 0.6$, the center column shows the results for $\alpha = 0.8$, and the right column presents the results for $\alpha = 1.0$. Each row in Fig. 4.48 represents a loading step in the PFEM simulation.

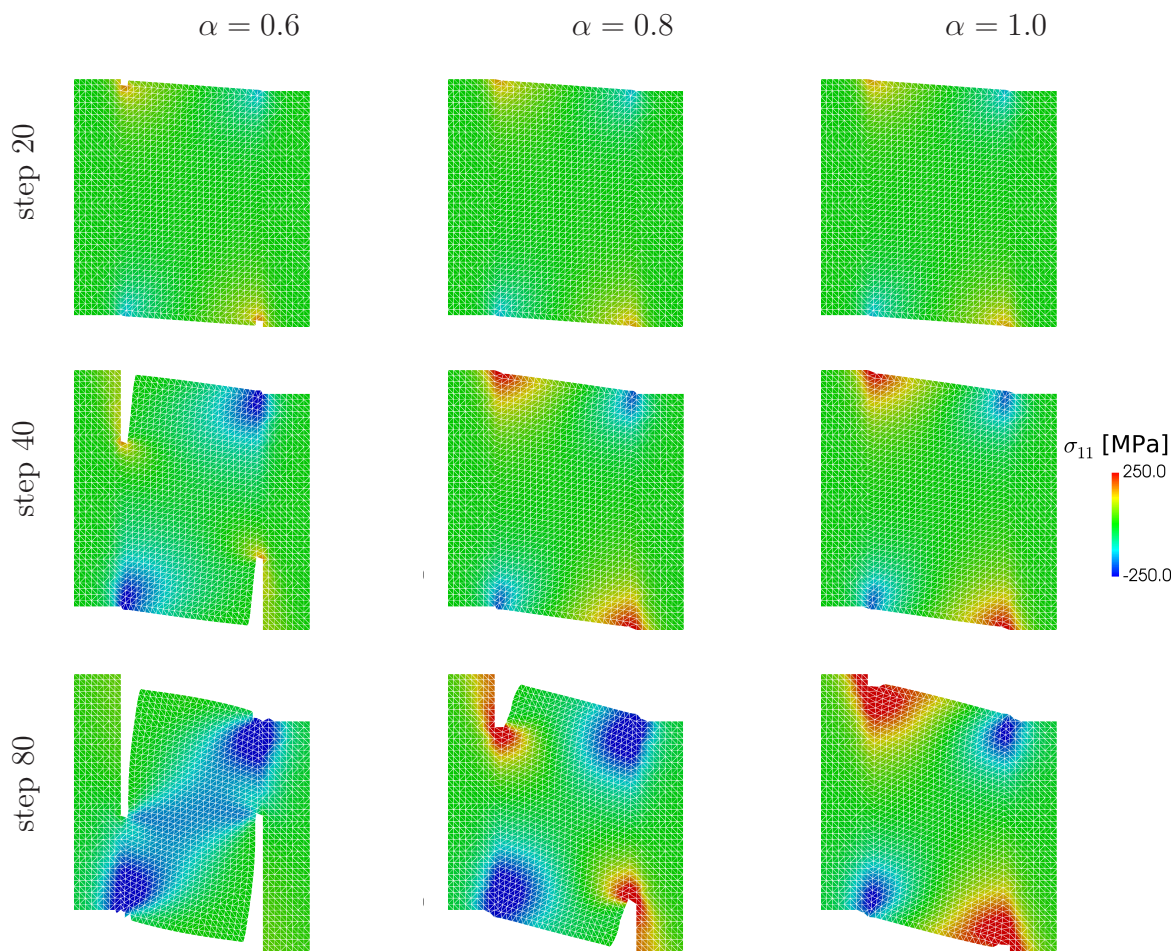


Fig. 4.48: Material separation by shearing for varying α

As can be seen in Fig. 4.48 the left column - i.e. the results of the simulation for $\alpha = 0.6$ - the material separates early in the simulation and therefore may be described as brittle. In the right column the material undergoes larger deformations before separating. From the results in Fig. 4.48 can be concluded that the parameter α provides a spectrum for the material separation from brittle to tough material behaviour. Furthermore, it can be seen that material separation, although being related to maximal strain, occurs at positions with high stress concentrations; here the edges of the fixtures.

Chapter 5

Cutting Simulations

The following chapter is devoted to PFEM simulations of cutting processes. In the beginning, vertical cutting of hyperelastic material is investigated. In this example the cutting force is studied for varying values of α and several steps of the cutting process are visualised. The following section focusses on the cutting of elasto-plastic material, where the states of stresses and plastic deformations in the workpiece are studied, which result from the cutting process. Furthermore, parameter studies on important process parameters such as hardening modulus, rake angle, and α are conducted. In these studies the effect of the parameters on the cutting force is observed. The chapter concludes with a comparison of cutting forces to empirical results. At this point it should be noted that only the work piece is considered as a deformable body. The tool is treated as rigid body throughout all following simulations.

5.1 Vertical Cutting of Hyperelastic Material

The first cutting simulation is a vertical cut of a workpiece. For this simulation, a hyperelastic material is used and the boundary conditions are illustrated in Fig. 5.1. The base of the workpiece is partly fixed and a vertical displacement is applied to the tool, forcing it to cut the workpiece.

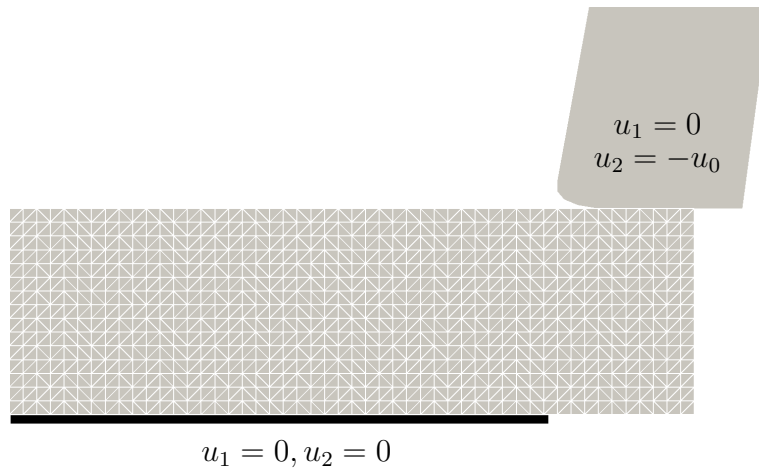


Fig. 5.1: Boundary conditions for vertical cutting

For the cutting simulations with hyperelastic material, the Lamé constants are set to $\lambda = 2160$ MPa and $\mu = 925$ MPa. Figure 5.2 presents the vertical stress component σ_{22} , and Fig. 5.3 shows the shear stress σ_{12} for a selected simulation step.

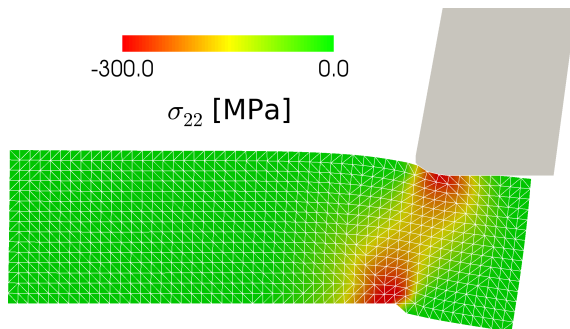


Fig. 5.2: Stress component σ_{22}

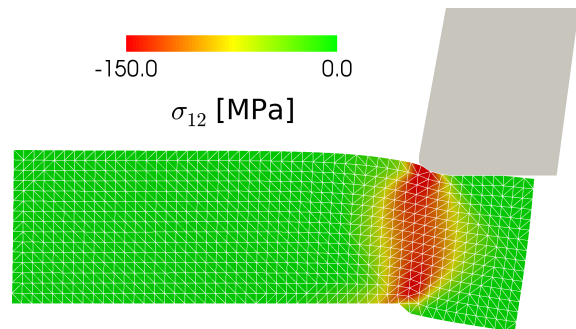
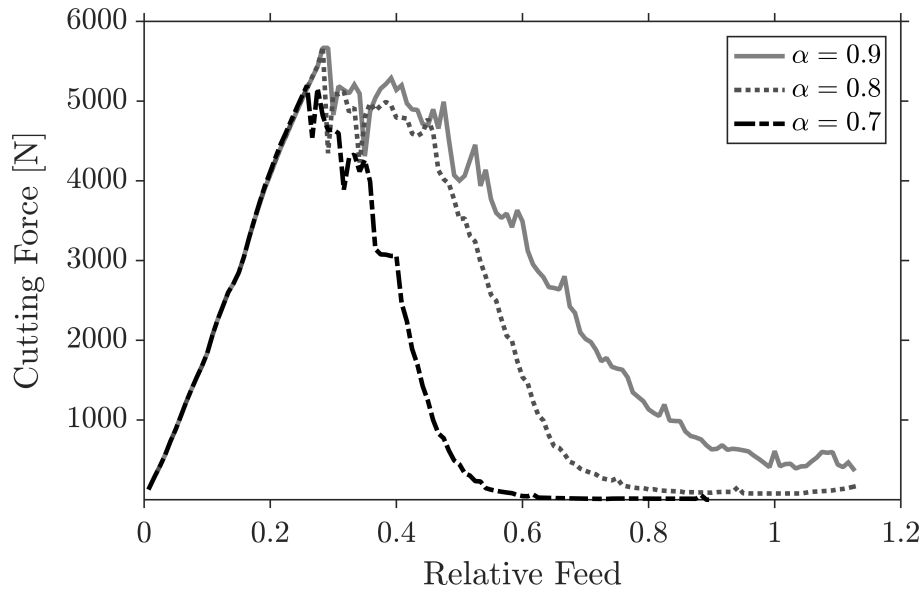


Fig. 5.3: Shear stress σ_{12}

In Fig. 5.2 it can be observed that high compressive stresses develop underneath the tool during the cutting operation. Figure 5.3 demonstrates the shear stress during the cutting process and it can be seen that a band of high shear stresses emerges. In order to study the influence of the parameter α , a parameter study is conducted. Fig. 5.4 shows the resulting cutting forces for three different values of α .

Fig. 5.4: Cutting force for variation of α

The cutting forces in Fig. 5.4 are obtained by summing the vertical component of the reaction forces of all tool nodes. The cutting forces are then plotted with regard to the relative feed, which is defined as the tool displacement with respect to the thickness of the workpiece. As can be seen in Fig. 5.4, the parameter α has a strong influence on the cutting force. The peak of the cutting force for $\alpha = 0.9$ is significantly higher compared to the peak of the cutting force for $\alpha = 0.7$. Even after the cutting force passes the peak, the level remains higher compared to the cutting force for $\alpha = 0.7$. This is due to the fact that the boundary segments endure higher stretches before failing. To affirm this effect, contour plots for three different values of α are shown in Fig. 5.5. The left column in Fig. 5.5 shows the results of simulations with $\alpha = 0.7$, the center column shows the results for $\alpha = 0.8$, and the right column presents the results for $\alpha = 0.9$. Each row in Fig. 5.5 represents a selected step in the PFEM simulation.

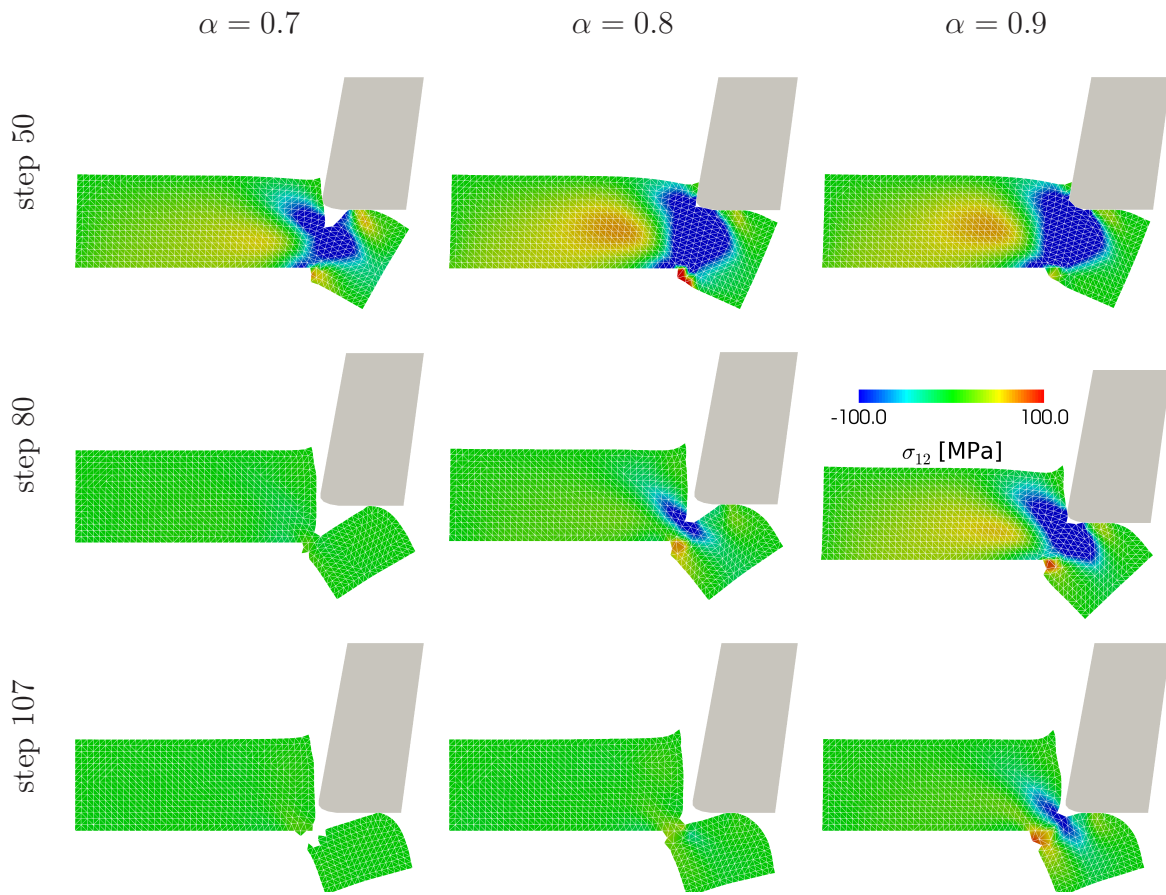


Fig. 5.5: Vertical cutting simulations for three values of α

As can be seen in the left column in Fig. 5.5 - i.e. the results of the simulation for $\alpha = 0.7$ - the material separates early and reacts rather brittle. In the right column the material undergoes somewhat higher deformations before separating.

5.2 Extrusion of Elasto-Plastic Material

In extrusion processes the material of the workpiece is pushed through a die and experiences large plastic deformations (see Klocke and König (2006)). In the following simulations the die is treated as a rigid body and the workpiece is fed to the extruder by a displacement boundary condition as shown in Fig. 5.6. The extrusion is modelled with an elasto-plastic material, where the Young's modulus is set to $E = 210000$ MPa, the Poisson ratio $\nu = 0.3$, the hardening modulus $k = 2500$ MPa, the initial yield stress $\sigma_y = 275$ MPa, and the exponent of the hardening power law from Eq. (2.72) $m = 0.8$.

The material parameters mimic steel and can be found in literature such as Wittel (2009); Böge et al. (2015). Since a ductile material is considered, $\alpha = 1.4$.

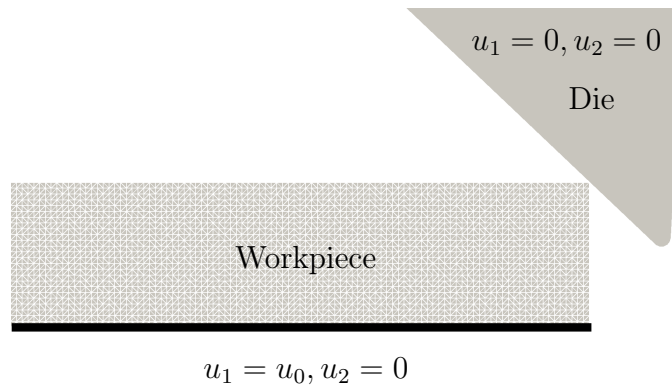


Fig. 5.6: Setup and boundary conditions for extrusion simulation

Figure 5.7 shows four steps of the extrusion process and the colour code represents the stress σ_{11} . In step 70 compressive stresses develop where the workpiece is pressed against the die. In step 140 the region of compressive stresses has increased and the workpiece is partly extruded. As the process continues, tensile stresses develop in the extruded part and the material builds up in front of the die.

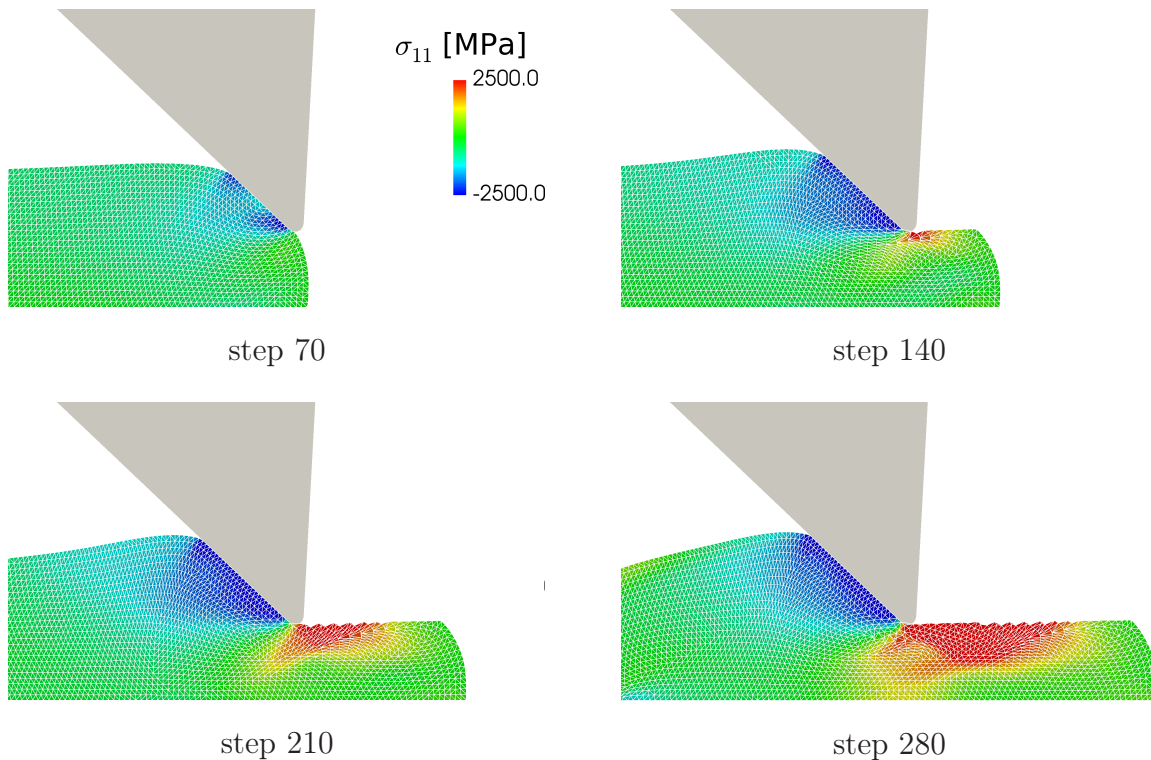


Fig. 5.7: Stress σ_{11} during extrusion process

In Fig. 5.7 it can be observed that an uneven surface develops in the extruded material. This effect is a result of high tensile stresses in this part of the workpiece and the consequential failure of boundary segments. The plastic deformation of the workpiece is illustrated in Fig. 5.8.

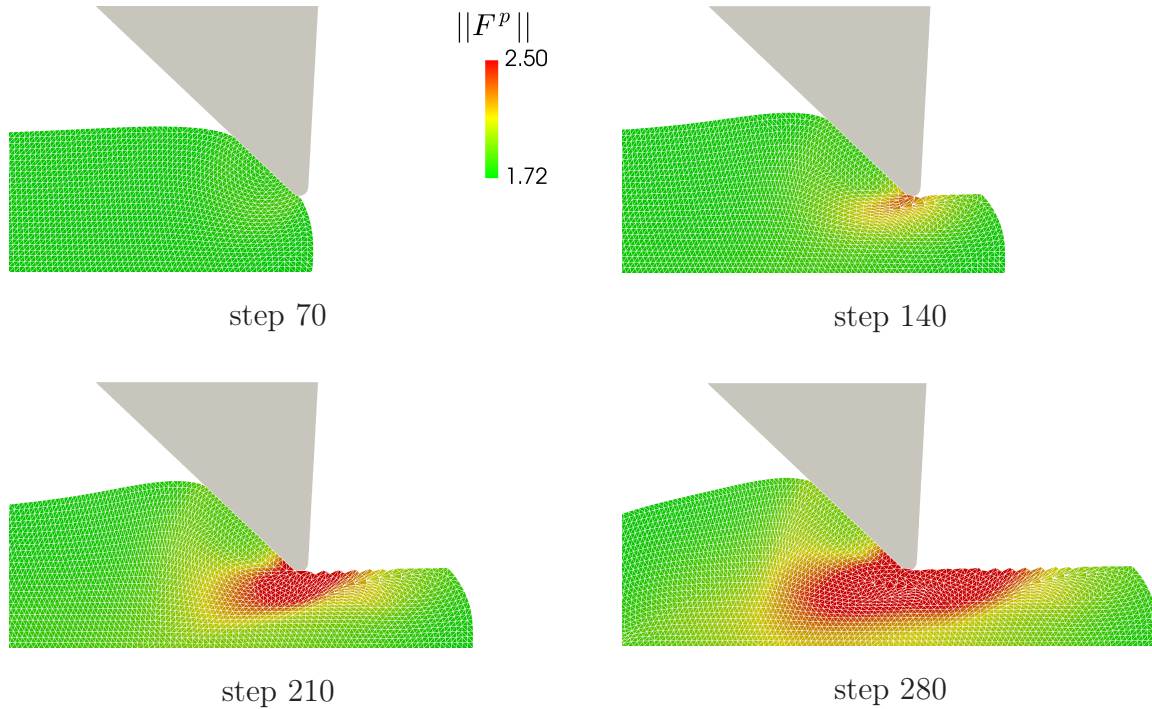


Fig. 5.8: Plastic deformation during extrusion

In the following a parameter study on the initial yield stress σ_y is conducted for the extrusion process. Except for the initial yield stress, the material parameters are taken according to the previous extrusion simulation. In this parameter study the extrusion forces are compared for three values of σ_y .

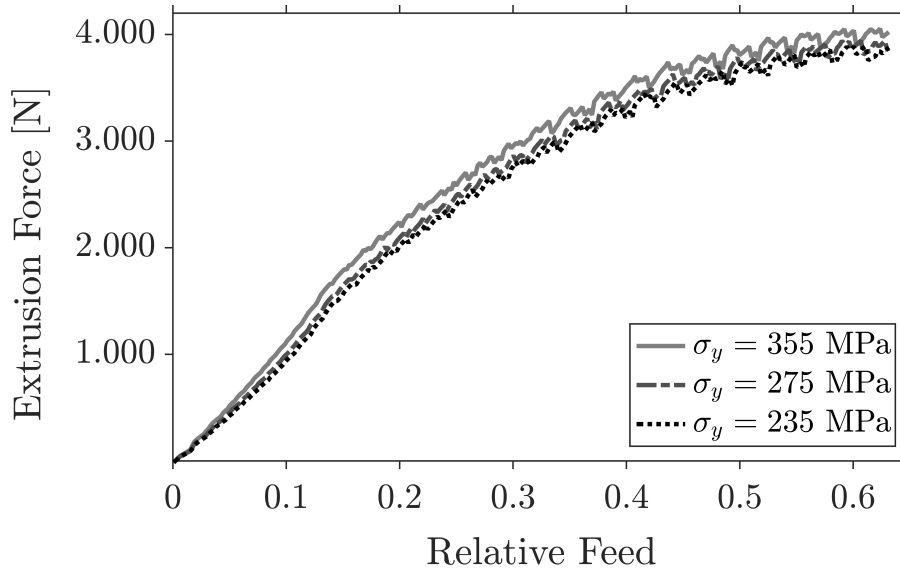


Fig. 5.9: Extrusion force for variation of initial yield stress σ_y

The extrusion forces increase as the workpiece is fed into the die, as can be seen in Fig. 5.9. It can also be observed that higher values for the initial yield stress σ_y lead to increased extrusion forces. This effect is as expected since the material deforms plastically at higher stresses. Simulations of extrusion processes can also be found in Oñate et al. (2014).

5.3 Cutting Simulations for Elasto-Plastic Material

In the following simulations we consider an elasto-plastic material, where Young's modulus $E = 210000$ MPa, the Poisson ratio $\nu = 0.3$, the hardening modulus $k = E/100$, the initial yield stress $\sigma_y = 235$ MPa, and the exponent of the hardening power law from Eq. (2.72) $m = 1$. The material parameters mimic steel and can be found in literature such as Wittel (2009); Böge et al. (2015). The cutting depth is set to 0.5mm. The setup for the simulations is presented in Fig. 5.10.

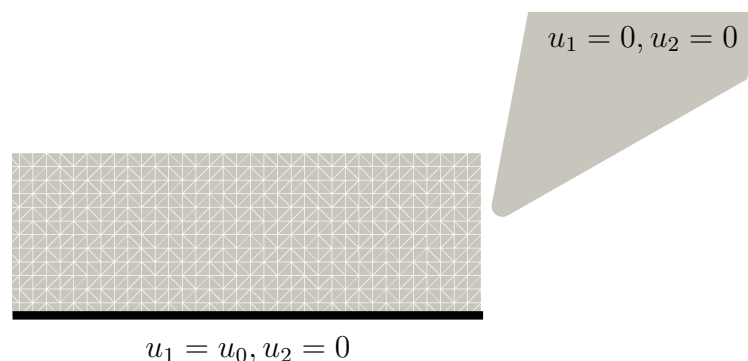


Fig. 5.10: Boundary conditions for cutting simulations

Throughout the simulation, a displacement boundary condition is applied at the base of the workpiece, which translates the work piece towards the tool. The tool is fixed and normal contact is considered between tool and workpiece. Figures 5.11, 5.12, 5.13, and 5.14 illustrate stress and deformation patterns as described in classical textbooks on manufacturing and cutting like Denkena and Toenshoff (2011); König (1999); Böge et al. (2015).

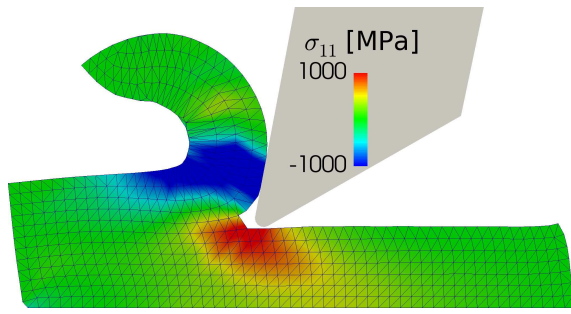


Fig. 5.11: σ_{11} stress in workpiece during cutting

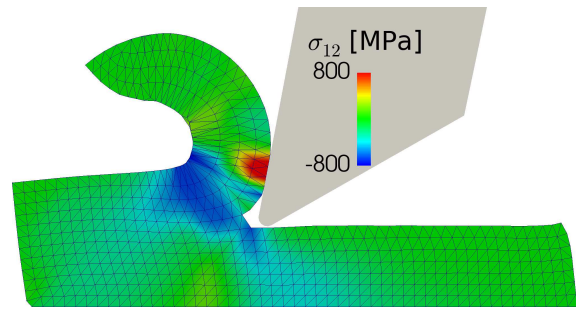


Fig. 5.12: Shear stress σ_{12}

In Fig. 5.11 the workpiece exhibits a region of compressive stresses in front of the tool, and tensile stresses underneath the tool, where the material is stretched due to the chip formation. In Fig. 5.12 two regions of high shear stresses can be observed. The region with shear stresses of a negative sign is often called primary shear zone, whereas the region with positive shear stresses is called secondary shear zone (see Denkena and Toenshoff (2011); Böge et al. (2015)). Figures 5.13 and 5.14 show a contour plot of the norm of the plastic deformation gradient during cutting.

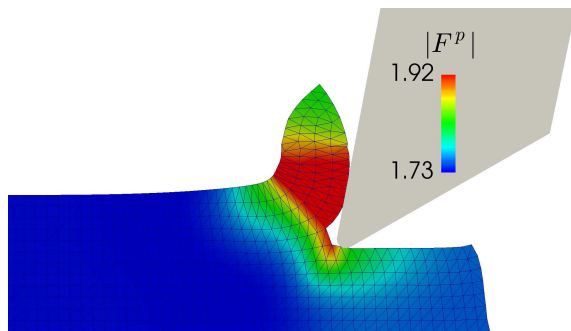


Fig. 5.13: Norm of the plastic deformation gradient $\|F^p\|$

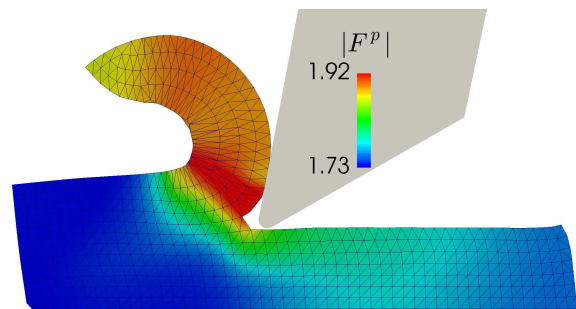


Fig. 5.14: Plastic deformation in progressed cut

The plastic deformation as shown in Fig. 5.13 and 5.14 evolves with the progress of the cut. In Fig. 5.13 a small chip has formed under large plastic deformations and the process zone is surrounded by a region of smaller plastic deformations. In Fig. 5.14 the cut has progressed and the chip is fully plastified. Here, the workpiece exhibits small plastic deformations in the whole segment behind the cutting tool. Moreover, a small burr can be observed on the workpiece. The following section is concerned with a parameter study of important process parameters.

5.4 Study of Important Process Parameters

5.4.1 Variation of the Hardening Modulus

The power law in Eq. (2.72) represents the hardening model used for the cutting simulations. In this section, the influence of the hardening modulus on the cutting force and the shape of the chip is studied. Figure 5.15 and 5.16 show contour plots of the stresses for two different hardening moduli.

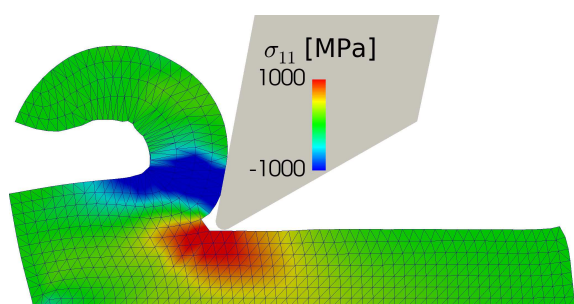


Fig. 5.15: Cauchy stress σ_{11} for a hardening modulus $k = E/100$

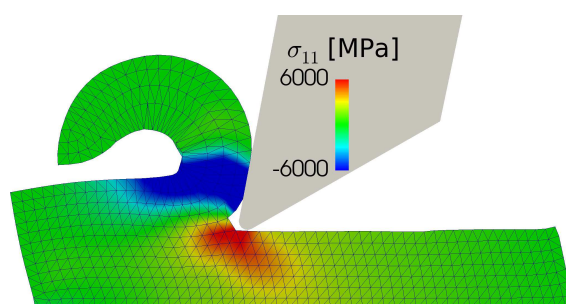


Fig. 5.16: Cauchy stress σ_{11} for a hardening modulus $k = E/10$

Figures 5.15 and 5.16 present similar patterns in the stress distribution. However, the stresses for the simulation with $k = E/10$ (Fig. 5.16) are significantly higher as for the simulation with $k = E/100$ in Fig. 5.15. By taking a closer look on the shape of the chip, it can be seen that the chip in the simulation with $k = E/10$ (Fig. 5.16) appears somewhat more curled. Figure 5.17 shows the cutting forces for a variation of the hardening modulus k .

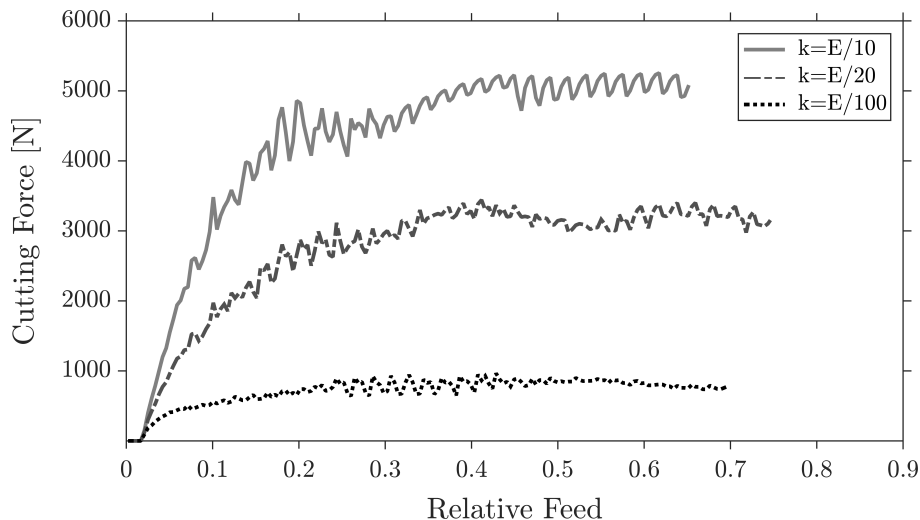


Fig. 5.17: Cutting force for variation of hardening modulus

The graphs in Fig. 5.17 illustrate that higher values for k lead to increased cutting forces. The zig-zag shape of the cutting forces is caused by the α -shape algorithm. While the line segment in front of the cutting edge is stretched, the cutting force increases. After reaching the critical stretch prescribed by the value of α , the boundary segment fails, a new boundary is detected, and the cutting force declines.

5.4.2 Variation of the Rake Angle

The rake angle γ is defined as the angle between the front edge of the cutting tool (rake face) and the vertical as illustrated in Fig. 1.1. From textbooks on cutting such as Denkena and Toenshoff (2011); Böge et al. (2015) it is known that a small rake angle leads to high cutting forces, whereas increased rake angles lead to reduced cutting forces. Figures 5.18 and 5.19 present contour plots of the stresses for simulations with two different rake angles.

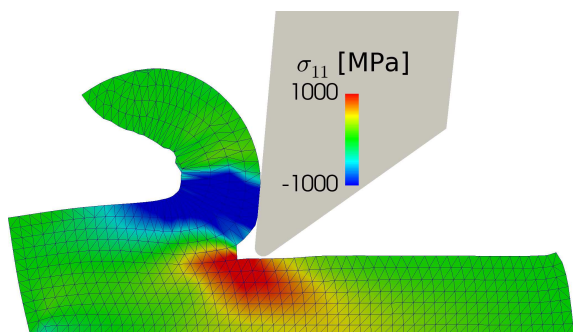


Fig. 5.18: Cauchy stress σ_{11} for small rake angle γ_-

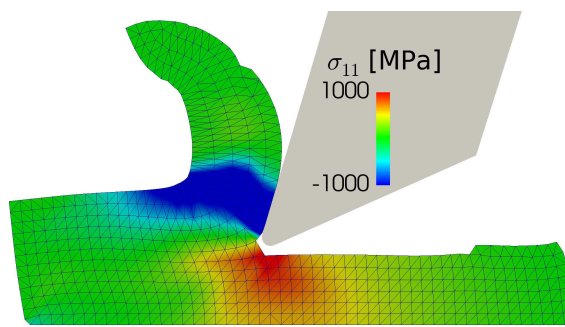


Fig. 5.19: Cauchy stress σ_{11} for large rake angle γ_+

In Fig. 5.18 and 5.19 differences in the distribution of stresses as well as in the deformation are visible. The chip in the simulation with a large rake angle is slightly thicker and the cutting depth is increased. Moreover, the zone of high tensile stresses underneath the tool is somewhat increased. Figure 5.20 shows the influence of the rake angle γ on the cutting force.

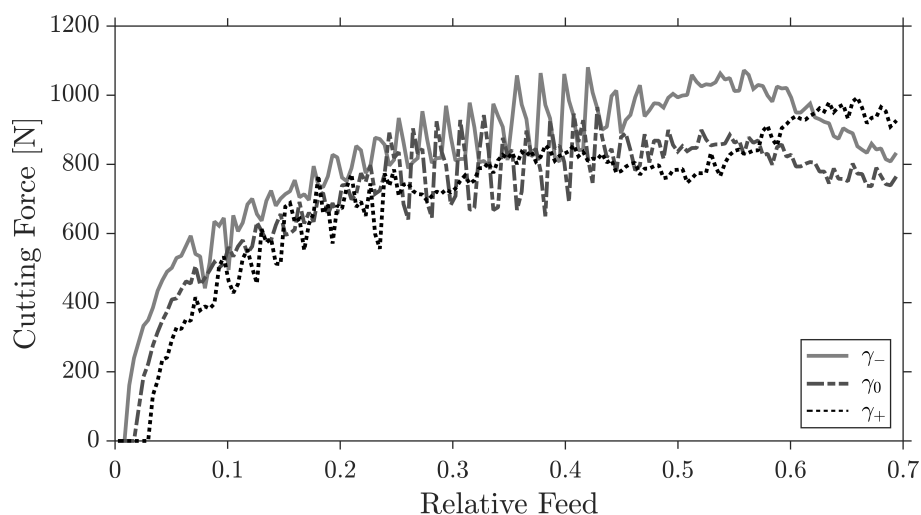


Fig. 5.20: Plot of cutting forces for varying rake angles

The rake angles for the three simulations are set to $\gamma_- = 5^\circ$, $\gamma_0 = 11^\circ$, $\gamma_+ = 17^\circ$. Figure 5.20 affirms that small rake angles, denoted by γ_- produce increased cutting forces. In contrast, cutting with increased rake angles leads to reduced cutting forces as expected.

5.4.3 Variation of α

As established in Sec. 4.3, the value of α influences the material separation and can be interpreted as the maximum stretch of a line segment. The cutting simulation processes in a way that the boundary segments in front of the tool are stretched up to the critical stretch prescribed by α . If this threshold is exceeded, the segment fails and a new boundary is created. Figures 5.21 and 5.22 present the results of cutting simulations for two different values of α .

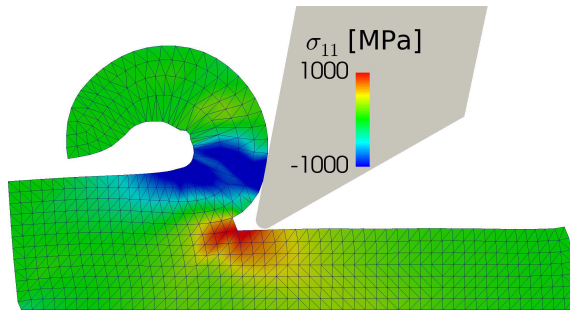


Fig. 5.21: Contour plot of stress σ_{11} for $\alpha = 0.7$

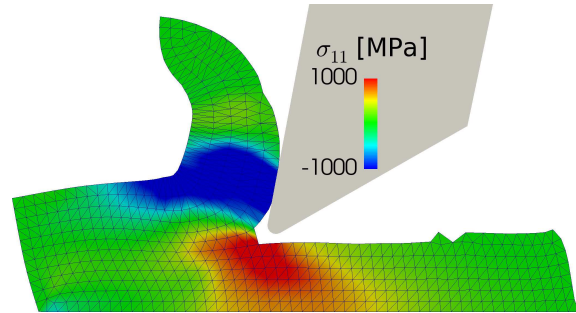


Fig. 5.22: Contour plot of stress σ_{11} for $\alpha = 0.9$

Figure 5.21 shows the result of a cutting simulation with $\alpha = 0.7$. The low value of α provokes the material to separate at relatively small deformations and the material reacts rather brittle. The tensile stresses underneath the cutting tool are reduced and the cut progresses in a certain distance in front of the tool. In contrast, in Figure 5.22 the cut progresses immediately in front of the tool and the material shows a more ductile behavior. The increased value of α results in a large region of tensile stresses, and the chip thickness is increased. Figure 5.23 shows a plot of the cutting forces for a variation of α .

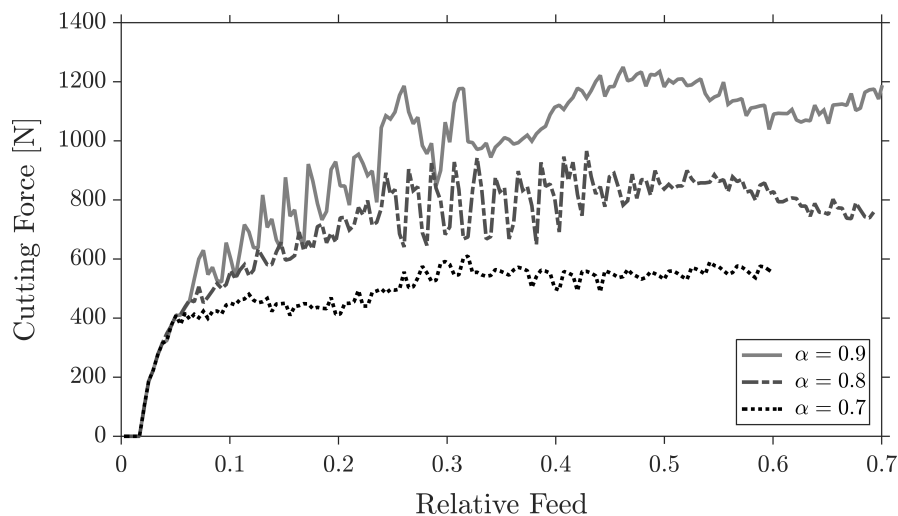


Fig. 5.23: Plot of cutting forces for varying α

The curves in Fig. 5.23 coincide in the beginning of the cutting process. However, at a certain relative feed they diverge due to the different values of α . The simulation with $\alpha = 0.9$ allows the highest stretch of boundary segments in front of the tool. Hence, the cutting force is significantly higher compared to the simulations with a lower α . The cutting force from the simulation with $\alpha = 0.7$ is lower, since the line segments in front of the cutting tool fail at a much lower stretch. The effect of α on the ductility of the material can also be demonstrated by observing the norm of the

plastic deformation gradient $\|\mathbf{F}^p\|$, which is plotted in Fig. 5.24 for three values of α . The left column in Fig. 5.24 shows the results of simulations with $\alpha = 0.7$, the center column shows the results for $\alpha = 0.8$, and the right column presents the results for $\alpha = 0.9$. Each row in Fig. 5.24 represents a selected step in the PFEM simulation.

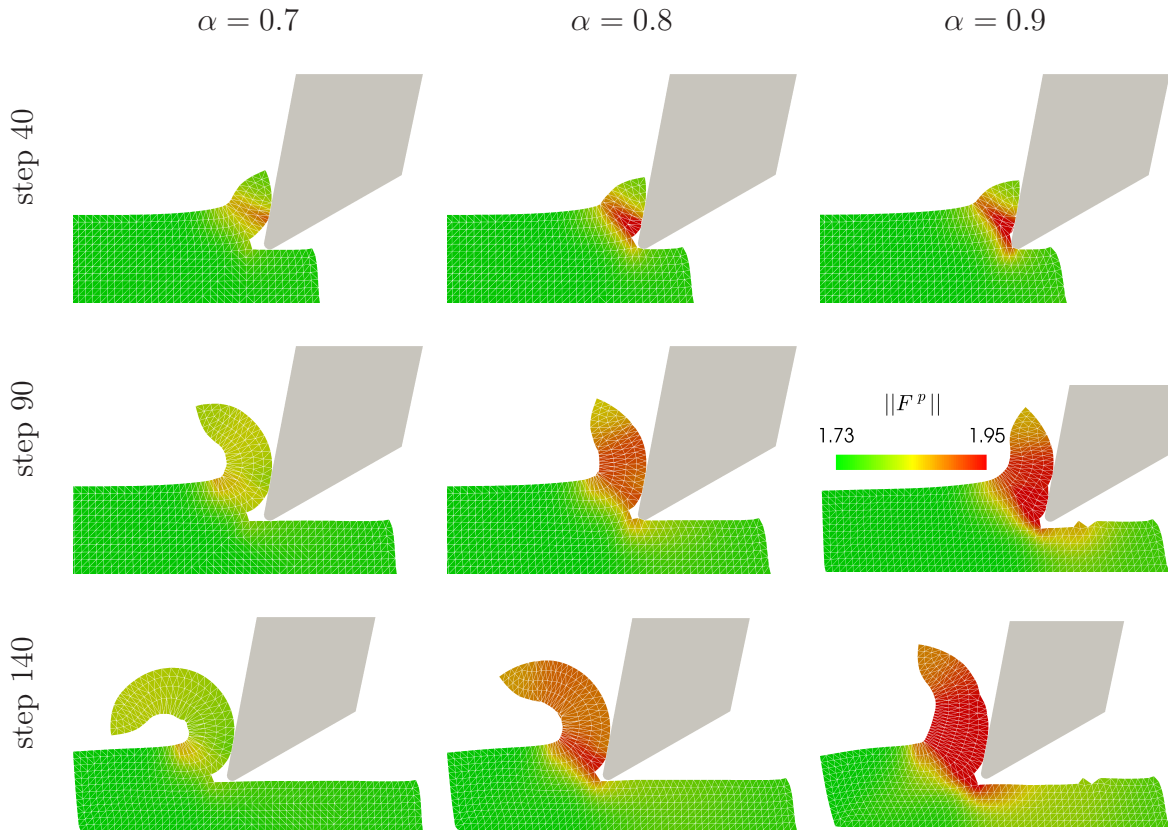


Fig. 5.24: Plastic deformation $\|\mathbf{F}^p\|$ for varying value of α

The results in the first column ($\alpha = 0.7$) display a simulation of a rather brittle material. Throughout the simulation, the norm of the plastic deformation gradient $\|\mathbf{F}^p\|$ is small compared to the simulations with higher values of α . It can also be observed that the material of the workpiece separates in a certain distance in front of the tool. In the right column ($\alpha = 0.9$) the material exhibits more ductility and the norm of the plastic deformation gradient reaches high values compared to the simulations in the left column. Furthermore, it can be seen that the chip formation differs significantly throughout the three columns i.e. three different values of α .

5.5 Comparison to Empirical Results

In manufacturing technology a concept has been developed in Kienzle (1952) to model the required power in turning processes. In order to calculate the power, the cutting force is calculated, which may be employed as empirical reference for the cutting force computations with the PFEM. The resultant force \mathbf{F}_z in Fig. 5.25 is a product of the cutting process and in general is a force in three dimensional space. This resultant force consists of the components

$$\mathbf{F}_z = \mathbf{F}_c + \mathbf{F}_f + \mathbf{F}_p. \quad (5.1)$$

In Eq. (5.1) the cutting force \mathbf{F}_c acts tangential on the turning workpiece. The passive force \mathbf{F}_p acts in direction of the cutting tool, and the feed force \mathbf{F}_f in opposite direction of the feed. The forces are illustrated in Fig. 5.25.

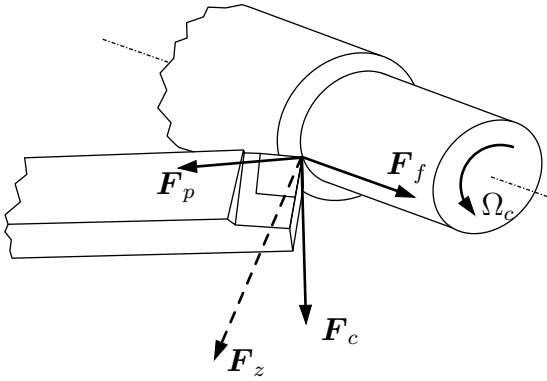


Fig. 5.25: Cutting forces in turning operation

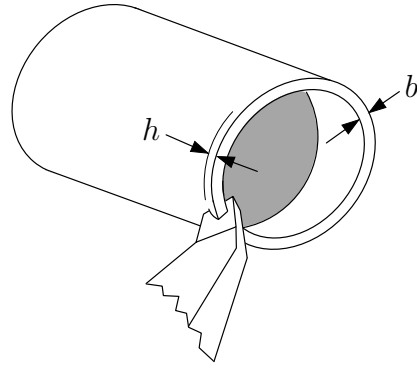


Fig. 5.26: Dimensions in orthogonal cutting

In this work the focus is on computing the cutting force \mathbf{F}_c with the PFEM and on a comparison to orthogonal cutting as demonstrated in Fig. 5.26. Orthogonal cutting is characterised by orthogonal axes of cutting tool and workpiece. Derived in Kienzle (1952) and later mentioned in textbooks on manufacturing as Denkena and Toenshoff (2011); Böge et al. (2015), the formula

$$F_c = |\mathbf{F}_c| = b h k_c \quad (5.2)$$

can be applied to estimate the cutting force. Since the cutting force in this work is computed in a plane strain setting, the cutting thickness is set to $b = 1\text{mm}$. In Eq. (5.2) h is the undeformed chip thickness and k_c is defined as

$$k_c = \frac{k_{c1.1}}{h^z} k_\lambda (\lambda_1, \dots, \lambda_n) . \quad (5.3)$$

The constants $k_{c1.1}$, and z are material specific parameters which can be found in literature as Böge et al. (2015) and k_λ is an influence factor, which is usually employed to account for friction, shape of the cutting tool, etc.. However, in this work we set $k_\lambda = 1$ to reduce the number of parameters involved in this observation. For the comparison between the results of the Kienzle formula in Eq. (5.2) and the cutting force from the PFEM simulations, we focus on the material S 235 JR. Then the parameters in Eq. (5.3) follow to $k_{c1.1} = 1780$ MPa and $z = 0.17$. The undeformed chip thickness is set to $h = 0.5$ mm and the parameters used to describe the elastoplastic material in the PFEM simulations are $E = 210000$ MPa, $\nu = 0.3$, $\sigma_y = 235$ MPa, $k = 2500$ MPa, $m = 0.8$, and $\alpha = 0.8$. Figure 5.27 shows the cutting force from the PFEM simulation and the estimate from Eq. (5.2).

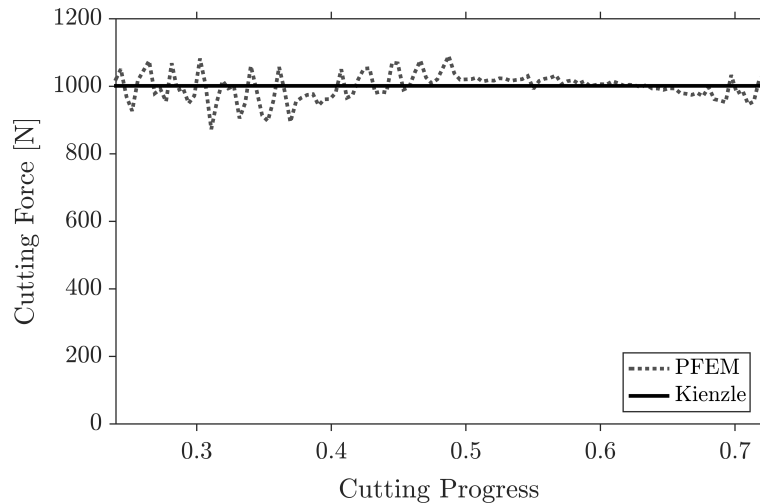


Fig. 5.27: Comparison of PFEM and Kienzle formula for chip thickness $h = 0.5$ mm

As can be seen in Fig. 5.27 the PFEM simulation is capable to reproduce the empirical result from Eq. (5.2). In order to provide a more wholesome comparison, Eq. (5.3) is studied for various cutting depths h in the following. In Böge et al. (2015) a range for the cutting depth $h = 0.05 - 2.5$ mm is provided, in which Eq. 5.3 is valid. In Fig. 5.28 the cutting force from Eq. (5.3) is plotted in the valid range of h , as well as cutting forces of PFEM simulations.

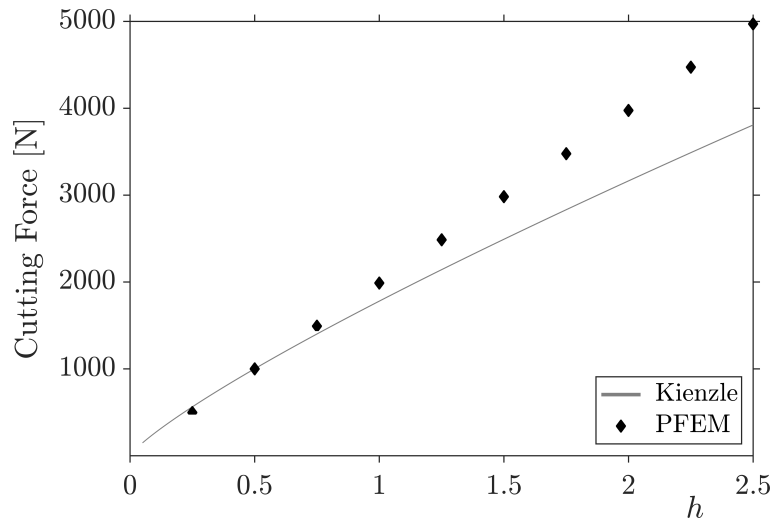


Fig. 5.28: Cutting forces from PFEM simulations and Kienzle's estimate

In order to generate the graph that represent the PFEM simulations in Fig. 5.28, only a sequence of the cutting force is considered, where the force is relatively steady. This sequence corresponds to the sequence selected for the comparison in Fig. 5.27. After extracting the sequence, the mean value is computed. These mean values are represented in Fig. 5.28 by the diamond shaped markers. As can be observed, the PFEM matches Kienzle's equation nicely for low cutting depths. However, for deeper cuts the results diverge.

Chapter 6

Conclusion and Outlook

The PFEM implementation presented in this work is based on finite deformations and two constitutive laws are considered. A hyperelastic constitutive law is implemented to model cutting processes of plastics. Furthermore, an elasto-plastic material is considered, which enables simulations of metal cutting. An attempt to validate the PFEM in a comparison to the FEM is made for both material models. The benchmarks for the comparison include simulations with uniform deformations, such as uniaxial stretch and simple shear. In this study the reaction forces of both methods are compared and good agreement of the results can be observed. However, in these simulations the deformation gradient is spatially constant and one can argue that in this case the frequent projection of the history data should barely influence the quality of the results. Therefore, a further benchmark is considered, where the boundary conditions lead to a non-uniform deformation gradient. Another objective in this study is the influence of the number of projections and the discretisation on the cutting force. From the results can be concluded that refined discretisations within the PFEM simulations lead to a better agreement of both methods. On the other hand, an increasing number of projections impairs the agreement.

In the first applications of the PFEM only experience based recommendations were provided on the choice of the crucial parameter α and no efforts were made in order to find a physical interpretation. In this work it is shown that α can be associated with a maximum stretch of boundary segments and a relation to the stretch ratio is demonstrated. A restriction on the quadratic stretch is derived as well as on the first eigenvalue of the right Cauchy-Green tensor. Furthermore, it is shown that α not only restricts the stretch of boundary segments but the orientation as well. It is elaborated that former boundary segments fail if the first eigenvalue exceeds the limit $\lambda_1^2 = 4\alpha^2$ and the orientation of the former segment is collinear to the corresponding eigenvector. PFEM simulations on basic deformations such as uniaxial stretch, biaxial stretch, and simple shear are presented to support the outcome of the physical interpretation. Moreover, a graphical representation of the restriction on boundary segments is pro-

vided. The graphs demonstrate a restriction on the length and orientation of boundary segments in their undeformed configuration before and after a deformation. Further PFEM simulations of tensile tests with different values for α reveal the meaning of the parameter in the context of material science. It is shown that α can be related to the fracture strain in tensile tests. Since the results of the tensile test with realistic geometry slightly deviate from the expectation, a follow up study is conducted with simple geometries and uniform deformations. In addition to that, a parameter study on α is regarded in another PFEM simulation with hyperelastic material and material separation. On this example it is demonstrated that by varying α , the separation of the material can be triggered. It is shown that small values of α can be associated with brittle material, where a high α can be used to describe tough material.

In the beginning of chapter 5 cutting simulations with hyperelastic material are presented. A parameter study on α is conducted in order to investigate the influence on the cutting force. As predicted in the physical interpretation of the α -shape method, increasing values of α lead to an increased critical stretch of boundary segments. As a result, the boundary segments in front of the cutting tool endure more stretch before failing and therefore the cutting force increases for an increasing α . A further example presented in this work is an extrusion simulation of elasto-plastic material. It is shown that high compressive stresses develop in the workpiece in front of the die and high tensile stresses evolve in the extruded material. Furthermore, the plastic deformation in the workpiece during the extrusion is demonstrated and a parameter study on the initial yield stress σ_y shows that increased values for σ_y lead to increased extrusion forces. In the following section the cutting of elasto-plastic material is considered. Effects as the plastic deformation during cutting are visualised as well as the distribution of stresses. In literature on manufacturing technology such as Denkena and Toenshoff (2011) shear bands are reported in the workpiece, which can be reproduced by the PFEM simulations. Furthermore, the influence of important process parameters is studied. A variation of the hardening modulus shows that an increased hardening modulus produces increased cutting forces. A parameter study on the rake angle demonstrates that smaller rake angles produce higher cutting forces, which agrees with literature on manufacturing such as Denkena and Toenshoff (2011); Böge et al. (2015). The final parameter study is concerned with the parameter α . As expected from the physical interpretation and previous results, the cutting force increases with an increasing value of α . In cutting simulations with elasto-plastic material it can be shown that simulations with high values for α lead to increasing plastic deformations. Moreover, the chip formation varies for varying values of α and it can be seen that cutting simulations of brittle material (small value of α) resemble a similar chip formation as it is known from literature such as Denkena and Toenshoff (2011); Böge et al. (2015). On the other hand, cutting simulations with a high value of α resemble the

chip formation of tough materials. The final section is concerned with a comparison of cutting forces from PFEM simulations to an empirical benchmark known from Kienzle (1952). In a first approach the Kienzle equation is compared to a cutting simulation for an explicit cutting depth h . The parameters for the constitutive law and α used for this comparison are then adopted to conduct a more wholesome investigation. In this study the cutting simulations are compared to the Kienzle equation for several cutting depths and the results expose good agreement especially for low cutting depths.

For future work, an expansion of the implementation to three dimensional problems should be considered. The current simulations only consider normal contact between tool and workpiece. Friction and heat conduction should be accounted for, since they play an important role in cutting processes. Since the PFEM has already been successfully applied to problems with fluid-solid interaction, the heat conduction between a coolant and the workpiece should be investigated. In order to improve the current implementation, triangular finite elements with quadratic shape functions should be considered.

Bibliography

- I.A. Alhafez, Y. Gao, and H.M. Urbassek. Nanocutting. a comparative molecular-dynamics study of fcc, bcc, and hcp metals. *Curr. Nanosci.*, 13, 2017. doi: 10.2174/1573413712666160530123834.
- R. Aubry, S.R. Idelsohn, and E. Oñate. Particle finite element method in fluid-mechanics including thermal convection-diffusion. *Computers & Structures*, 83(17):1459 – 1475, 2005. ISSN 0045-7949. doi: <http://dx.doi.org/10.1016/j.compstruc.2004.10.021>.
- R. Aubry, E. Oñate, and S.R. Idelsohn. Fractional step like schemes for free surface problems with thermal coupling using the lagrangian pfem. *Computational Mechanics*, 38(4):294–309, 2006. doi: 10.1007/s00466-006-0058-5.
- K.J. Bathe. *Finite Element Procedures*. Prentice Hall, 2006. ISBN 9780979004902.
- W. Becker and D. Gross. *Mechanik elastischer Körper und Strukturen*. Springer Verlag, 2002. ISBN 9783540435112.
- A. Böge, W. Böge, G. Böge, P. Franke, P. Kurzweil, and W. Weißbach. *Formeln und Tabellen Maschinenbau: Für Studium und Praxis*. Springer Fachmedien Wiesbaden, 2015. ISBN 9783658098179.
- J. Bonet and R.D. Wood. *Nonlinear Continuum Mechanics for Finite Element Analysis*. Cambridge University Press, 2nd edition edition, 2008. ISBN 9780521838702.
- J.M. Carbonell, E. Oñate, and B. Suárez. Modeling of ground excavation with the particle finite-element method. *Computational Plasticity*, 136(4):455–463, 2010. doi: 10.1061/(ASCE)EM.1943-7889.0000086.
- J.M. Carbonell, E. Oñate, and B. Suárez. Modelling of tunnelling processes and rock cutting tool wear with the particle finite element method. *Computational Mechanics*, 52(3):607–629, 2013. doi: 10.1007/s00466-013-0835-x.
- A. Cuitiño and M. Ortiz. A material independent method for extending stress update algorithms from small strain plasticity to finite plasticity with multiplicative kinematics. *Engineering Computations*, 9:437–451, 1992.

- E.A. de Souza Neto, D. Peric, and D.R.J. Owen. *Computational Methods for Plasticity: Theory and Applications*. Wiley, 2011. ISBN 9781119964544.
- B. Denkena and H.K. Toenshoff. *Spanen: Grundlagen*. VDI-Buch. Springer Berlin Heidelberg, 2011. ISBN 9783642197727.
- P. Eberhard and T. Gaugele. Simulation of cutting processes using mesh-free lagrangian particle methods. *Computational Mechanics*, 51(3):261–278, 2013. doi: 10.1007/s00466-012-0720-z.
- H. Edelsbrunner and E.P. Mücke. Three-dimensional alpha shapes. *ACM Trans. Graph.*, pages 43–72, 1994. doi: 10.1145/174462.156635.
- K. Fischer. Introduction to alpha shapes. *Department of Information and Computing Sciences, Faculty of Science, Utrecht University*, 2000.
- F. Fleissner, T. Gaugele, and P. Eberhard. Applications of the discrete element method in mechanical engineering. *Multibody System Dynamics*, 18(1):81, 2007. doi: 10.1007/s11044-007-9066-2.
- Y. Gao and H.M. Urbassek. Evolution of plasticity in nanometric cutting of fe single crystals. *Appl. Surf. Sci.*, 317:6–10, 2014. doi: 10.1016/j.apsusc.2014.08.020.
- R. Greve. *Kontinuumsmechanik*. Springer Berlin Heidelberg, 2003. ISBN 9783540007609.
- D. Gross and T. Seelig. *Bruchmechanik: Mit einer Einführung in die Mikromechanik*. Springer Berlin Heidelberg, 2016. ISBN 9783662467374.
- M. Heinstein and D. Segalman. Simulation of orthogonal cutting with smooth particles hydrodynamics. *Sandia National Laboratories*, 1997.
- W. Hellerich, G. Harsch, and S. Haenle. *Werkstoff-Führer Kunststoffe: Eigenschaften, Prüfungen, Kennwerte ; mit 56 Tabellen*. Hanser, 2004. ISBN 9783446225596.
- E. Hinton and J.S. Campbell. Local and global smoothing of discontinuous finite element functions using a least squares method. *International Journal for Numerical Methods in Engineering*, 8(3):461–480, 1974. doi: 10.1002/nme.1620080303.
- G.A. Holzapfel. *Nonlinear Solid Mechanics*. John Wiley & sons, LTD, 2000. ISBN 9780471823193.
- S.R. Idelsohn, E. Oñate, and F.D. Pin. The particle finite element method: a powerful tool to solve incompressible flows with free-surfaces and breaking waves. *International Journal for Numerical Methods in Engineering*, 61(7):964–989, 2004. doi: 10.1002/nme.1096.

- S.R. Idelsohn, E. Oñate, F.D. Pin, and Calvo N. Fluid–structure interaction using the particle finite element method. *Computer Methods in Applied Mechanics and Engineering*, 195(17–18):2100 – 2123, 2006. doi: <https://doi.org/10.1016/j.cma.2005.02.026>.
- O. Kienzle. Die bestimmung von kräften und leistungen an spanenden werkzeugen und werkzeugmaschinen. *Z. VDI*, 94, 1952.
- F. Klocke and W. König. *Fertigungsverfahren 4*. VDI-Buch. Springer Berlin Heidelberg, 2006. ISBN 9783540395331.
- K. Komvopoulos and S.A. Erpenbeck. Finite element modeling of orthogonal metal cutting. *Journal of Engineering for Industry*, 113(3):253–267, 1991.
- W. König. *Fertigungsverfahren 1: Drehen, Fräsen, Bohren*. VDI-Buch. Springer Berlin Heidelberg, 1999. ISBN 9783540662693.
- E.H. Lee. Elastic-plastic deformation at finite strains. *Journal of Applied Mechanics*, 36:1–6, 1969.
- K. Li, X.-L. Gao, and J.W. Sutherland. Finite element simulation of the orthogonal metal cutting process for qualitative understanding of the effects of crater wear on the chip formation process. *Journal of Materials Processing Technology*, 127:309 – 324, 2002. doi: [https://doi.org/10.1016/S0924-0136\(02\)00281-9](https://doi.org/10.1016/S0924-0136(02)00281-9).
- J. Limido, C. Espinosa, M. Salaün, and J.L. Lacomme. {SPH} method applied to high speed cutting modelling. *International Journal of Mechanical Sciences*, 49(7):898 – 908, 2007. doi: <https://doi.org/10.1016/j.ijmecsci.2006.11.005>.
- A.G. Mamalis, M. Horváth, A.S. Branis, and D.E. Manolakos. Finite element simulation of chip formation in orthogonal metal cutting. *Journal of Materials Processing Technology*, 110:19 – 27, 2001. doi: [https://doi.org/10.1016/S0924-0136\(00\)00861-X](https://doi.org/10.1016/S0924-0136(00)00861-X).
- F.J. Montáns and Bathe. On the stress integration in large strain elasto-plasticity. *Computational Fluid and Solid Mechanics*, pages 494–497, 2003. doi: [10.1016/B978-008044046-0.50122-6](https://doi.org/10.1016/B978-008044046-0.50122-6).
- J. Oliver, J.C. Cante, R. Weyler, C. González, and J. Hernandez. Particle finite element methods in solid mechanics problems. *Computational Plasticity*, pages 87–103, 2007.
- E. Oñate, S.R. Idelsohn, F. Del Pin, and R. Aubry. The particle finite element method — an overview. *International Journal of Computational Methods*, 01(02):267–307, 2004. doi: [10.1142/S0219876204000204](https://doi.org/10.1142/S0219876204000204).

- E. Oñate, M.A. Celigueta, and S.R. Idelsohn. Modeling bed erosion in free surface flows by the particle finite element method. *Acta Geotechnica*, 1(4):237–252, 2006. doi: 10.1007/s11440-006-0019-3.
- E. Oñate, S.R. Idelsohn, M.A. Celigueta, and R. Rossi. Advances in the particle finite element method for the analysis of fluid–multibody interaction and bed erosion in free surface flows. *Computer Methods in Applied Mechanics and Engineering*, 197(19):1777 – 1800, 2008. doi: <http://dx.doi.org/10.1016/j.cma.2007.06.005>.
- E. Oñate, M.A. Celigueta, S.R. Idelsohn, F. Salazar, and B. Suárez. Possibilities of the particle finite element method for fluid–soil–structure interaction problems. *Computational Mechanics*, 48(3):307, 2011. doi: 10.1007/s00466-011-0617-2.
- E. Oñate, A. Franci, and J.M. Carbonell. A particle finite element method for analysis of industrial forming processes. *Computational Mechanics*, 54(1):85–107, 2014. doi: 10.1007/s00466-014-1016-2.
- J.M. Rodríguez, J.M. Carbonell, J.C. Cante, and J. Oliver. Continuous chip formation in metal cutting processes using the particle finite element method (pfem). *International Journal of Solids and Structures*, 2017a. doi: <https://doi.org/10.1016/j.ijsolstr.2017.04.030>.
- J.M. Rodríguez, P. Jonsén, and A. Svoboda. Simulation of metal cutting using the particle finite-element method and a physically based plasticity model. *Computational Particle Mechanics*, 4:35–51, 2017b. doi: 10.1007/s40571-016-0120-9.
- M. Sabel, C. Sator, and R. Müller. A particle finite element method for machining simulations. *Computational Mechanics*, 54:123–131, 2014. doi: 10.1007/s00466-014-1025-1.
- M. Sabel, C. Sator, and R. Müller. Particle finite element simulations of cutting processes in manufacturing. *PAMM*, 16:231–232, 2016a. doi: 10.1002/pamm.201610104.
- M. Sabel, C. Sator, T.I. Zohdi, and R. Müller. Application of the particle finite element method in machining simulation discussion of the alpha-shape method in the context of strength of materials. *Journal of Computing and Information Science in Engineering*, 17:7, 2016b. URL <http://dx.doi.org/10.1115/1.4034434>.
- M.H. Sadd. *Elasticity: Theory, Applications, and Numerics*. Elsevier Science, 2014. ISBN 9780124104327.
- C. Shet and X. Deng. Finite element analysis of the orthogonal metal cutting process. *Journal of Materials Processing Technology*, 105:95 – 109, 2000. doi: [https://doi.org/10.1016/S0924-0136\(00\)00595-1](https://doi.org/10.1016/S0924-0136(00)00595-1).

- J.R. Shewchuk. Triangle: Engineering a 2d quality mesh generator and delaunay triangulator. pages 203–222, 1996. doi: 10.1007/BFb0014497.
- J.C. Simo and T.J.R. Hughes. *Computational Inelasticity*. Springer New York, 2000. ISBN 9780387975207.
- A.J.M. Spencer. *Continuum Mechanics*. Dover Publications, Inc., 2004. ISBN 9780486435947.
- E. Uhlmann, R. Gerstenberger, M. Schäfer, and J Kuhnert. Development of the mesh-free finite pointset method for the simulation of chip formation. *ZWF Zeitschrift für wirtschaftlichen Fabrikbetrieb*, 106(7-8):510–514, 2011. doi: 10.3139/104.110606.
- E. Uhlmann, R. Gerstenberger, and J. Kuhnert. Cutting simulation with the meshfree finite pointset method. *Procedia CIRP*, 8:391 – 396, 2013. doi: <http://dx.doi.org/10.1016/j.procir.2013.06.122>.
- H. Wittel. *Roloff/Matek Maschinenelemente: Tabellenbuch*. Viewegs Fachbücher der Technik. Vieweg + Teubner, 2009. ISBN 9783834806895.
- P. Wriggers. *Nichtlineare Finite-Element-Methoden*. Springer Berlin Heidelberg, 2001. ISBN 9783540677475.
- B. Zhang and A. Bagchi. Finite element simulation of chip formation and comparison with machining experiment. *Journal of Engineering for Industry*, 116(3):289–297, 1994.
- M. Zhu and M.H. Scott. Modeling fluid–structure interaction by the particle finite element method in opensees. *Computers & Structures*, 132:12 – 21, 2014. doi: <http://dx.doi.org/10.1016/j.compstruc.2013.11.002>.
- M. Zhu and M.H. Scott. Unified fractional step method for lagrangian analysis of quasi-incompressible fluid and nonlinear structure interaction using the pfem. *International Journal for Numerical Methods in Engineering*, 109:1219–1236, 2017. doi: 10.1002/nme.5321.
- O.C. Zienkiewicz and R.L. Taylor. *The Finite Element Method: The basis*. Fluid Dynamics. Butterworth-Heinemann, 2000a. ISBN 9780750650496.
- O.C. Zienkiewicz and R.L. Taylor. *The Finite Element Method: Solid mechanics*. Fluid Dynamics. Butterworth-Heinemann, 2000b. ISBN 9780750650557.

Curriculum Vitae

Name: Matthias Sabel

Geburtsort: Zell (Mosel)

09.1992 – 07.1996 Grundschule Blankenrath

08.1996 – 07.2002 Realschule Zell
Abschluss: Mittlere Reife

08.2002 – 07.2005 Ausbildung zum Kfz-Mechaniker
Autohaus Ziefer in Simmern

09.2005 – 06.2006 Berufsoberschule, Berufsbildende Schule Cochem
Abschluss: Fachhochschulreife

10.2006 – 08.2010 Bachelor-Studium des Wirtschaftsingenieurwesen
mit Schwerpunkt Fahrzeugtechnik
an der Fachhochschule Bingen
Bachelor-Thesis:
Simulation von Riemenscheiben
Abschluss: Bachelor of Engineering

10.2010 – 03.2013 Master-Studium im Bereich Computational Engineering
an der Technischen Universität Kaiserslautern
Master-Thesis:
*Gemischte FEM-Analysen für inkompressibles
Materialverhalten*
Abschluss: Master of Science

05.2013 – 09.2017 Wissenschaftlicher Mitarbeiter
am Lehrstuhl für Technische Mechanik,
Fachbereich Maschinenbau und Verfahrenstechnik
der Technischen Universität Kaiserslautern